The Astrophysical Journal Supplement Series, 276:69 (35pp), 2025 February https://doi.org/10.3847/1538-4365/ad9fef

APOKASC-3: The Third Joint Spectroscopic and Asteroseismic Catalog for Evolved Stars in the Kepler Fields

Marc H. Pinsonneault[1], Joel C. Zinn[2], Jamie Tayar[3], Aldo Serenelli[4,5], Rafael A. García[6], Savita Mathur[7,8,9], Mathieu Vrard[1,10], Yvonne P. Elsworth[11,12], Benoit Mosser[13], Dennis Stello[14,15,16], Keaton J. Bell[17], Lisa Bugnet[18], Enrico Corsaro[19], Patrick Gaulme[20,21], Saskia Hekker[12,22,23], Marc Hon[24,25], Daniel Huber[15,25], Thomas Kallinger[26], Kaili Cao[27,28], Jennifer A. Johnson[1,27], Bastien Liagre[6,7,29], Rachel A. Patton[1,27], Ângela R. G. Santos[30,31], Sarbani Basu[32], Paul G. Beck[7,8], Timothy C. Beers[33], William J. Chaplin[11,12], Katia Cunha[34,35], Peter M. Frinchaboy[36,37], Léo Girardi[38], Diego Godoy-Rivera[7,8], Jon A. Holtzman[21], Henrik Jönsson[39], Szabolcs Mészáros[40,41], Claudia Reyes[14], Hans-Walter Rix[42], Matthew Shetrone[43], Verne V. Smith[44], Taylor Spoo[36], Keivan G. Stassun[45], and Ji Wang[1]

[1] Department of Astronomy, The Ohio State University, Columbus, OH 43210, USA
[2] Department of Physics and Astronomy, California State University, Long Beach, Long Beach, CA 90840, USA
[3] Department of Astronomy, University of Florida, Gainesville, FL 32611, USA
[4] Institute of Space Sciences (ICE, CSIC), Carrer de Can Magrans S/N, Campus UAB, E-08193 Bellaterra, Spain
[5] Institut d'Estudis Espacials de Catalunya, Carrer Esteve Terradas, 1, Edifici RDIT, Campus PMT-UPC, E-08860, Castelldefels, Spain
[6] Université Paris-Saclay, Université Paris Cité, CEA, CNRS, AIM, 91191, Gif-sur-Yvette, France
[7] Instituto de Astrofsica de Canarias (IAC), C/Va Lactea, s/n, E-38200 La Laguna, Tenerife, Spain
[8] Universidad de La Laguna (ULL), Departamento de Astrofísica, E-38206 La Laguna, Tenerife, Spain
[9] Space Science Institute, 4750 Walnut Street, Suite 205, Boulder, CO 80301, USA
[10] Observatoire de la Côte d'Azur, CNRS, Laboratoire Lagrange, Bd de l'Observatoire, CS 34229, 06304 Nice Cedex 4, France
[11] University of Birmingham, School of Physics and Astronomy, Edgbaston, Birmingham B15 2TT, UK
[12] Stellar Astrophysics Centre, Department of Physics and Astronomy, Aarhus University, Ny Munkegade 120, DK-8000 Aarhus C, Denmark
[13] LESIA, Observatoire de Paris, Université PSL, CNRS, Sorbonne Université, Université de Paris, 92195 Meudon, France
[14] School of Physics, University of New South Wales, NSW 2052, Australia
[15] Sydney Institute for Astronomy (SIfA), School of Physics, University of Sydney, NSW 2006, Australia
[16] ARC Centre of Excellence for All Sky Astrophysics in 3 Dimensions (ASTRO 3D), Australia
[17] Department of Physics, Queens College, City University of New York, Flushing, NY 11367, USA
[18] Institute of Science and Technology Austria (ISTA), Am campus 1, Klosterneuburg, Austria
[19] INAF—Osservatorio Astrofisico di Catania, via S. Sofia 78, 95123 Catania, Italy
[20] Thüringer Landessternwarte, Sternwarte 5, 07778 Tautenburg, Germany
[21] Department of Astronomy, MSC 4500, New Mexico State University, P.O. Box 30001, Las Cruces, NM 88003, USA
[22] Heidelberg University (ZAH/LSW), Königstuhl 12, 69118 Heidelberg, Germany
[23] Heidelberg Institute for Theoretical Studies, Schloss-Wolfsbrunnenweg 35, 69118 Heidelberg, Germany
[24] Kavli Institute for Astrophysics and Space Research, Massachusetts Institute of Technology, 77 Massachusetts Avenue, Cambridge, MA 02139, USA
[25] Institute for Astronomy, University of Hawai'i, 2680 Woodlawn Drive, Honolulu, HI 96822, USA
[26] Institute for Astronomy, University of Vienna, Türkenschanzstrasse 17, A-1180 Vienna, Austria
[27] Center for Cosmology and AstroParticle Physics (CCAPP), The Ohio State University, 191 West Woodruff Avenue, Columbus, OH 43210, USA
[28] Department of Physics, The Ohio State University, 191 West Woodruff Avenue, Columbus, OH 43210, USA
[29] ENS Paris-Saclay, Université Paris-Saclay, 91190, Gif-sur-Yvette, France
[30] Instituto de Astrofísica e Ciências do Espaço, Universidade do Porto, CAUP, Rua das Estrelas, PT4150-762 Porto, Portugal
[31] Departamento de Física e Astronomia, Faculdade de Ciências, Universidade do Porto, Rua do Campo Alegre 687, PT4169-007 Porto, Portugal
[32] Department of Astronomy, Yale University, P.O. Box 208101, New Haven CT, 06520-8101, USA
[33] Department of Physics and Astronomy, and JINA Center for the Evolution of the Elements University of Notre Dame, Notre Dame, IN 46556, USA
[34] University of Arizona, Steward Observatory, Tucson, AZ 85719, USA
[35] Observatório Nacional, São Cristóvão, Rio de Janeiro, Brazil
[36] Department of Physics and Astronomy, Texas Christian University, TCU Box 298840, Fort Worth, TX 76129, USA
[37] Maunakea Spectroscopic Explorer, Canada-France-Hawaii-Telescope, Kamuela, HI 96743, USA
[38] Osservatorio Astronomico di Padova, INAF, Vicolo dell Osservatorio 5, I35122 Padova, Italy
[39] Materials Science and Applied Mathematics, Malmö University, SE-205 06 Malmö, Sweden
[40] ELTE Eötvös Loránd University, Gothard Astrophysical Observatory, Szombathely, Hungary
[41] MTA-ELTE Lendület "Momentum" Milky Way Research Group, Hungary
[42] Max Planck Institute for Astronomy, Königstuhl 17, 69117 Heidelberg, Germany
[43] University of California Observatories, University of California Santa Cruz, 1156 High Street, Santa Cruz, CA 95064, USA
[44] NSF's NOIRLab, Tucson, AZ 85719, USA
[45] Department of Physics and Astronomy, Vanderbilt University, Nashville, TN 37235, USA

Received 2024 August 12; revised 2024 December 9; accepted 2024 December 9; published 2025 February 5

Abstract

In the third APOKASC catalog, we present data for the complete sample of 15,808 evolved stars with APOGEE spectroscopic parameters and Kepler asteroseismology. We used 10 independent asteroseismic analysis techniques and anchor our system on fundamental radii derived from Gaia L and spectroscopic T_{eff}. We provide evolutionary state, asteroseismic surface gravity, mass, radius, age, and the data used to derive them for 12,418 stars. This includes 10,036 exceptionally precise measurements, with median fractional uncertainties in $\nu_{\rm max}$, $\Delta\nu$, mass, radius, and age of 0.6%, 0.6%, 3.8%, 1.8%, and 11.1%, respectively. We provide more limited data for 1624 additional stars that either have lower-quality data or are outside of our primary calibration domain. Using lower red giant branch (RGB) stars, we find a median age for the chemical thick disk of $9.14 \pm 0.05(\rm ran) \pm 0.9(\rm sys)$ Gyr with an age dispersion of 1.1 Gyr, consistent with our error model. We calibrate our red clump (RC) mass loss to derive an age consistent with the lower RGB and provide asymptotic GB and RGB ages for luminous stars. We also find a sharp upper-age boundary in the chemical thin disk. We find that scaling relations are precise and accurate on the lower RGB and RC, but they become more model dependent for more luminous giants and break down at the tip of the RGB. We recommend the use of multiple methods, calibration to a fundamental scale, and the use of stellar models to interpret frequency spacings.

Unified Astronomy Thesaurus concepts: Asteroseismology (73); Stellar evolution (1599); Stellar ages (1581); Stellar populations (1622); Stellar pulsations (1625); Stellar masses (1614)

Materials only available in the online version of record: machine-readable tables

1. Introduction

Stellar oscillations reveal the inner workings of stars, and time-domain surveys from space have made it possible to measure them in exquisite detail for large numbers of stars. Asteroseismology, the study of stellar pulsations, has therefore emerged as a transformational tool for understanding stellar astrophysics and stellar populations.

The Kepler satellite had an especially dramatic impact on asteroseismology due to a combination of unprecedented precision, sample size, and long-duration observations. Over the past decade, the community has steadily refined the interpretation of this landmark data set. Time-resolved space data does not stand alone; its power is amplified by complementary ground-based campaigns. High-resolution spectroscopy, in particular, is essential for stellar characterization, population studies, and chemical evolution. The combined power of time-domain and spectroscopic data has resulted in catalogs of thousands of masses and radii for evolved red giant stars, opening up a completely new age dimension that has changed our understanding of the formation and evolution of the Milky Way galaxy. A detailed analysis of oscillation frequency patterns has also yielded novel insights into stellar physics. Two examples show the depth of the potential insights. Core He-burning stars with nondegenerate cores, hereafter red clump or RC stars, can be distinguished from shell H-burning stars, hereafter red giant branch (RGB) stars, with degenerate cores (T. R. Bedding et al. 2011), and internal rotation rates have been measured for large numbers of giants (C. Gehan et al. 2018; G. Li et al. 2024; B. Mosser et al. 2024).

In this paper we perform a comprehensive analysis of the full joint sample of cool evolved stars with Kepler time-domain data and APOGEE high-resolution spectroscopy, hereafter APOKASC-3. This is the third paper in a series. M. H. Pinsonneault et al. (2014, APOKASC-1) released the first set of data combining a large (1916 star) high-resolution spectroscopic survey with asteroseismic data. We followed up with M. H. Pinsonneault et al. (2018, APOKASC-2), which enlarged the sample considerably to 6676 stars. APOKASC-2 also introduced an explicit calibration of the results to a fundamental system, in that case, giants in open clusters. Although powerful, the latter data set was incomplete, both in terms of spectroscopic and asteroseismic analysis. We can also now take advantage of data from the Gaia DR3 release (Gaia Collaboration et al. 2023), which permits a much more precise calibration of stellar properties.

1.1. Population Asteroseismology in the Kepler Fields

To place APOKASC-3 in context, a brief summary of the properties of solar-like oscillations is in order. Cool stars have deep convection zones in their outer layers. The turbulence within them generates waves, which are in turn refracted by the enormous density gradients in stars. Sufficiently low-frequency waves are reflected at the surface, producing an acoustic cavity. This combination naturally produces standing wave patterns at discrete frequencies, which can be detected from brightness or radial velocity variations. These oscillations were first detected in the Sun (R. B. Leighton et al. 1962; J. W. Evans & R. Michard 1962), and helioseismology yielded crucial data on the internal structure and global properties of the Sun; for a comprehensive review, see S. Basu (2016). These solar-like oscillations are a nearly universal feature of cool stars, making their study of general interest. We focus here on inferring global stellar properties—in particular, mass, radius, and age.

Solar-like oscillations are well described by spherical harmonics. The number of nodes in the radial, latitudinal, and longitudinal directions are given, respectively, by quantum numbers n, l, and m. Global inferences rely on l and n. Spatially resolved modes can be detected in the Sun, but for unresolved stars, only the lowest-order modes can be detected ($l = 0, 1, 2, 3$) because of cancellation effects.

Early ground-based campaigns had some success in detecting oscillations in other stars (T. R. Bedding 2014), creating the field of asteroseismology. However, Sunlike stars have low amplitudes, and it was difficult to detect oscillations in more evolved stars with ground-based telescopes because their slow oscillations required long uninterrupted time-series data. It was only with the advent of time-domain space missions, primarily designed for exoplanet transit studies, that the real potential of asteroseismology could be realized. Data from the CoRoT satellite (S. Hekker et al. 2009; J. De Ridder et al. 2009) established conclusively that evolved giants were solar-like oscillators. The Kepler mission dramatically expanded the sample size, with unprecedented data quality and light-curve duration as well (T. R. Bedding et al. 2010; D. Stello et al. 2013; J. Yu et al. 2018).

Sound waves spend most of their time in the outermost layers of stars ($c_s^2 \sim \frac{T}{\mu}$), where c_s is the sound speed, T is the temperature, and μ is the mean molecular weight. The absolute frequencies are therefore difficult to predict accurately from theoretical models, because they depend on difficult outer layer physics, such as the details of how modes reflect close to the surface. However, in Sunlike stars, even and odd l modes naturally separate into close pairs with a nearly uniform spacing between modes of the same degree l but different degree n. In asymptotic theory, this large frequency spacing $\Delta\nu$ is related to the mean density (M. Tassoul 1980). The observed pattern for giants is more complex because of mixed modes arising from interactions between p-modes, analogs of sound waves, and g-modes, analogs of water waves (W. A. Dziembowski et al. 2001; M. A. Dupret et al. 2009; T. R. Bedding et al. 2011; M. Grosjean et al. 2014). However, the radial ($l = 0$) modes retain a regular structure, allowing a precise measurement for $\Delta\nu$. The trapping of sound waves in an acoustic cavity is related to the density scale height near the surface of the star, which is tied to the surface gravity through hydrostatic balance. The frequency of maximum power $\nu_{\rm max}$ therefore scales with the surface gravity (H. Kjeldsen & T. R. Bedding 1995; K. Belkacem et al. 2011), so $\Delta\nu$ and $\nu_{\rm max}$ can be combined to infer masses and radii.

After the initial burst of discovery, it became apparent that complementary data on stellar properties was essential for further progress. The scalings between $\Delta\nu$, $\nu_{\rm max}$, and stellar variables depend on effective temperature $T_{\rm eff}$ and chemical abundances, as do stellar ages.

The next step to reliable masses and radii was establishing a robust $T_{\rm eff}$ scale. The groundbreaking Kepler Input Catalog (T. M. Brown et al. 2011), hereafter KIC, developed to identify stars that might host transiting planets, was tied to an absolute temperature scale by M. H. Pinsonneault et al. (2012). Further updates dramatically improved stellar characterization of targets (S. Mathur et al. 2017).

Initial stellar population studies used photometric metallicities, such as those in the original KIC. Although powerful in principle, such estimates are sensitive to extinction and the choice of filters (L. Casagrande & D. A. VandenBerg 2014). In particular, the griz filters adopted by the KIC yield only coarse metallicity data because they were primarily designed to characterize galaxies, not stars (M. H. Pinsonneault et al. 2012).

The solution for the determination of reliable abundances was the development of massive high-resolution spectroscopic surveys, which came of age in the last 10–15 yr. Large data sets, and automated pipeline analysis, yielded abundance mixtures, $T_{\rm eff}$, and other spectroscopic parameters of an unprecedented quality and sample size. We focus here on the Apache Point Observatory Galactic Evolution Experiment (S. R. Majewski et al. 2017), hereafter APOGEE, which is our reference spectroscopic data set.

APOGEE was part of the Sloan Digital Sky Survey (SDSS; D. G. York & J. Adelman 2000), and in both SDSS-III (D. J. Eisenstein et al. 2011) and SDSS-IV (M. R. Blanton et al. 2017). It was envisioned as an engine for Galactic archeology, the study of the formation and evolution of the Milky Way galaxy. It is a multifiber spectroscopic survey that uses a moderately high-resolution ($R \sim 22{,}000$) infrared spectrograph (J. C. Wilson et al. 2019) on the SDSS telescope (J. E. Gunn et al. 2006), with stellar parameters inferred using the ASPCAP pipeline (A. E. Garcìa Pérez et al. 2016). APOGEE targeted red giants in the Kepler field to take advantage of the overlap with seismology (G. Zasowski et al. 2013, 2017; R. L. Beaton et al. 2021). Asteroseismic surface gravities were invaluable calibrators for spectroscopic ones (J. A. Holtzman et al. 2018), while spectroscopic data allowed asteroseismic data to be used to infer mass, radius, and age.

The evolutionary state—whether we are observing stars before or after He burning has ignited—is also an important stellar property. Fortunately, evolutionary state can be inferred from a detailed study of the oscillation frequency pattern (B. Mosser et al. 2014; Y. Elsworth et al. 2019). Stars with spectra and asteroseismic states can also be used as a training set to infer spectroscopic evolutionary states. When asteroseismic states are not available, these spectroscopic evolutionary states can be used to distinguish RGB and RC stars, with typical recovery rates of order 93% (J. A. Holtzman et al. 2018).

The final major observational advance is the immense power of the Gaia mission (Gaia Collaboration et al. 2023), which permits precise and accurate distance measurements for the large majority of Kepler targets. In turn, these distances can be combined with Gaia photometry and 3D extinction maps, producing exquisitely precise and accurate luminosities. Luminosities, L, combined with absolute $T_{\rm eff}$ from APOGEE then can be used to compute fundamental radii, R, which are an invaluable cross-check on asteroseismic radius inferences (J. C. Zinn et al. 2019b). We therefore believe that this is an ideal time for a comprehensive analysis of Kepler asteroseismology.

1.2. APOKASC-3 Goals

Our effort has several important goals. First, we want to provide a legacy data set of the highest-quality Kepler asteroseismic measurements. To do this, we use a number of distinct analysis pipelines; targets with a large number of consistent measurements are the core sample for this purpose. This represents a significant advantage over single-method surveys, as it allows us to discover outliers and unusual light curves that can be difficult to analyze with automated methods.

Second, we want to anchor our mass, radius, and age measurements firmly to an absolute scale, which we can derive from a combination of Gaia DR3 and APOGEE data. This absolute reference system also allows us to quantify the domains in which asteroseismic inferences are the most reliable, and the domains where the assumptions in asteroseismic scaling relations break down. As an example, one important lesson from APOKASC-1 and APOKASC-2 was the need to use stellar models to map the observed frequency pattern onto the mean density. Here we explore the impact of different choices for this mapping on the results. Even for a given mass, different ages are inferred from different stellar interiors codes and different choices for input physics, an additional subject that we explore here.

A third major goal is to be comprehensive. To that end, we present results for all Kepler stars with APOGEE spectra here. In a companion paper, we provide stellar properties for asteroseismic detections in stars without APOGEE spectra; the combination of the two represents the full census of asteroseismic detections of evolved cool stars in the Kepler fields.

Our final goal is transparency; we therefore provide both recommended mean values, alternative averages, and the individual results used to derive them. We also summarize a set of recommended best practices for population asteroseismology and outline areas for future research.

1.3. Changes from APOKASC-2

Our overall method is similar to that employed in APOKASC-2. We use multiple pipelines to interpret time series data from Kepler. The global oscillation properties $\Delta\nu$ and $\nu_{\rm max}$ are related to mass and radii through scaling relations, of the form

$$\frac{M}{M_\odot} = \left(\frac{f_{\nu{\rm max}}\,\nu_{\rm max}}{\nu_{{\rm max},\odot}}\right)^3 \left(\frac{f_{\Delta\nu}\,\Delta\nu}{\Delta\nu_\odot}\right)^{-4} \left(\frac{T_{\rm eff}}{T_{{\rm eff},\odot}}\right)^{1.5} \qquad (1)$$

and

$$\frac{R}{R_\odot} = \left(\frac{f_{\nu{\rm max}}\,\nu_{\rm max}}{\nu_{{\rm max},\odot}}\right) \left(\frac{f_{\Delta\nu}\,\Delta\nu}{\Delta\nu_\odot}\right)^{-2} \left(\frac{T_{\rm eff}}{T_{{\rm eff},\odot}}\right)^{0.5}. \qquad (2)$$

The $\nu_{\rm max}$ and $\Delta\nu$ measurements from the pipelines are placed on a common zero-point, and the measurement scatter between methods is taken as an error estimate. Asteroseismic diagnostics are used to infer evolutionary states where possible. Where they are not available, we use spectroscopic evolutionary-state diagnostics calibrated with asteroseismic data. Effective temperatures are taken from APOGEE spectroscopic data. The $f_{\Delta\nu}$ term relates the mean density to the observed frequency spacing, and is computed from stellar interiors models (see Section 3.1). The $f_{\nu{\rm max}}$ term is an empirical calibration function inferred from comparisons to fundamental data, and is used to place our results on an absolute scale (see Section 3.2). However, there are significant differences with APOKASC-2 as well:

1. This paper uses the full sample with spectroscopic data from the APOGEE survey and time-domain data from the Kepler survey.
2. We used different techniques for preparing the light curves, and a larger number of pipelines for light-curve analysis.
3. We adopted outlier rejection tools for asteroseismic measurements inconsistent either with a broad spectroscopic prior or the median results from other methods. This allowed us to identify background stars and deal with lower-quality time series data in some stars.
4. We used radii from a combination of Gaia L and APOGEE $T_{\rm eff}$ to anchor our fundamental scale, rather than masses in open cluster stars. In APOKASC-2, $f_{\nu{\rm max}} = 1$ with an adopted $\nu_{{\rm max},\odot} = 3076\ \mu$Hz. Here $f_{\nu{\rm max}}$ is a function of $\nu_{\rm max}$, with the same solar benchmark. These radii are also provided in the catalog.
5. We considered three distinct methods for inferring the mean density from the measured frequency spacings, and two methods for inferring ages.
6. We separate our detections into three categories: Gold, Silver, and Detections (Section 2.2). Both $\nu_{\rm max}$ and $\Delta\nu$ are detected for Gold and Silver sample stars. They differ in that Gold sample stars have the most precise and accurate data, and Silver sample stars are ones with larger uncertainties. Detections are cases where we can only measure $\nu_{\rm max}$.
7. We provide flags for nondetections as well as sources that we attribute to background stars, and define domains where the scaling relations are valid.

1.4. Roadmap of This Paper and Related Publications

We discuss the 10 pipelines used to analyze the Kepler light curves in Appendix A, and our method for combining them into the global asteroseismic properties $\Delta\nu$ and $\nu_{\rm max}$ in Appendix B. In Section 2 we describe the APOKASC-3 sample selection criterion, spectroscopic properties, and our method for assigning evolutionary states. We infer masses, radii, and ages in Section 3. The catalog itself is presented in Section 4. We also illustrate stellar physics and stellar population applications of the data there. Our key results are summarized in Section 5, including recommended practices for population asteroseismology.

We also note some related papers here. The evolutionary states of the APOKASC-3 sample are the focus of a separate paper (M. Vrard et al. 2024). J. D. Roberts et al. (2024) described the empirical first dredge-up pattern using APOKASC-3 data. A theoretical treatment of both the first dredge-up and the RGB bump is provided by a separate paper (K. Cao & M.H. Pinsonneault 2025). Stars with oscillation frequencies close to the long-cadence Kepler Nyquist sampling frequency (∼283.2 μHz) require special analysis techniques, and they are the focus of B. Liagre et al. (2025, in preparation). The binary population in this sample was investigated by 2024, using Gaia and APOKASC data. The kinematic classification of this sample is presented in D. Godoy-Rivera et al. (2024).

We present asteroseismic data for stars without APOGEE spectra in R. García et al. (2025, in preparation), with more than 9100 additional targets. The Kepler-APOGEE sample was chosen from targets in the KIC that have time-domain data. Sustained efforts by the APOGEE team have resulted in substantial, but not complete, overlap between the two data sets. The large majority of the missing stars were too faint for APOGEE. Of the R. García et al. (2025, in preparation) stars, 6663 were detected by five or more pipelines in the initial analysis. The medium- and low-resolution LAMOST survey (X.-Q. Cui et al. 2012) is a valuable resource for these fainter stars (J.-N. Fu et al. 2020). It provides optical coverage that complements the IR data from APOGEE for a large data set. LAMOST results are also tied to the APOGEE scale; see, for example, M. Xiang et al. (2019), which provided abundance mixtures for 6 million stars.

2. The APOKASC-3 Sample

The Kepler field has been the subject of intensive study, and it was naturally a high priority for the APOGEE spectroscopic survey. Asteroseismology was a major focus but not the only one, so the APOGEE selection function needs to be considered. As discussed in APOKASC-1, the Kepler targeting for giants was also complex. The selection function therefore needs to be assessed carefully before using this data set for population studies (e.g., V. Silva Aguirre et al. 2018). For extended discussions of the targeting for the Kepler–APOGEE sample, see M. H. Pinsonneault et al. (2014) and G. V. A. Simonian et al. (2019).

2.1. The APOGEE Survey and Data Releases

The SDSS provides regular data releases; these include both new targets and new analysis techniques. Four different data releases (hereafter DR10, DR14, DR16, DR17) have been used in the APOKASC papers—Data Release 10 (C. P. Ahn et al. 2014) for APOKASC-1, Data Release 14 (B. Abolfathi et al. 2018) for

APOKASC-2, and Data Releases 16 and 17 (R. Ahumada et al. 2020; Abdurro'uf et al. 2022) for APOKASC-3. All of the data releases use the same underlying logic: spectra are fit in a multidimensional space to infer "raw" global parameters. The key ones for our purposes are $T_{\rm eff}$, $\log g$, [M/H], and [α/M]. Here, M is a metallicity index, closely correlated with Fe, and α is an index of elements associated with α-capture species. Individual abundances are inferred from selected features in spectral windows. Of these, we use [C/Fe] and [N/Fe] to infer spectroscopic evolutionary states. The global parameters $T_{\rm eff}$ and $\log g$ are then placed on an absolute scale in a postprocessing step. $T_{\rm eff}$ is adjusted to corrected values tied to the infrared flux method (IRFM; P. González Hernández & P. Bonifacio 2009), while $\log g$ is tied to asteroseismic surface gravities (J. A. Holtzman et al. 2018). There are also small adjustments to the abundance scale for consistency. The calibration procedure for DR16 is discussed in H. Jönsson et al. (2020), while that for DR17 can be found at https://www.sdss4.org/dr17/irspec/aspcap/. We use the differences between DR16 and DR17 as a measure of systematic uncertainties in the spectroscopic properties of the sample. We use DR16 data for assigning spectroscopic evolutionary states (see below). Projected rotation velocities $v \sin i$, where i is the inclination angle, are taken from R. A. Patton et al. (2024).

The full APOGEE-Kepler sample contains 23,363 unique targets. However, many of these are not in the domain where we expect asteroseismic detections from the long-cadence (30 minutes) time series data obtained by Kepler. These less-evolved targets were observed either as part of other programs or as telluric standards (G. V. A. Simonian et al. 2019).

Most, but not all, of our data is from DR17. The APOGEE survey has regular improvements and changes in the pipeline analysis, and as a result, the stellar parameters change in each data release. There are 15,321 stars classified as giants in DR17. In 74 additional cases, we had valid solutions in DR16 but not DR17, and adopted the DR16 values.[46] There were 175 additional targets classified as dwarfs in DR17 but as giants in DR16, so we searched for seismic signals in them as well.

In large samples, there are rare but interesting objects, and they can have unusual spectra. We therefore have to be careful not to exclude these stars by definition from our sample. The APOGEE automated pipeline has quality-control checks, and if the fit is poor, the BAD STAR flag is triggered, and calibrated values are not returned. Some of these spectra simply have poor data, but others represent classes of stars, such as rapid rotators or binaries, that are poorly fit by the standard templates. We searched for asteroseismic signals in 174 targets without good spectral fits that were classified as giants in the KIC, but do not provide mass, radius, and age because they require spectroscopic information.

Our total giant sample was therefore 15,742. We also performed a background source search in the dwarfs, and found 66 such targets that we also included in our catalog. This gives a total catalog sample of 15,808.

In Figure 1 we show the 15,570 targets in the APOKASC-3 sample with spectroscopic data, along with a histogram of the $\log g$ distribution.[47] A strong concentration of the sample around the location of the core He-burning RC and the red giant branch bump (RGBB) is apparent. Our sample range is 3000–6000 K in $T_{\rm eff}$ and -0.5 to 3.5 in $\log g$. The lower $T_{\rm eff}$ and $\log g$ bounds are the limits of the APOGEE sample, while the higher $T_{\rm eff}$ bound is set by the domain where solar-like oscillations are excited, and the higher $\log g$ bound where $\nu_{\rm max}$ exceeds the Nyquist sampling frequency.

Figure 2 shows the heavy element mixtures for APOKASC-3 stars that we used for this study in the [α/Fe] versus [Fe/H] plane. The bottom panel shows a scatter plot of the full sample, indicating the presence of a small sample of interesting low [α/Fe] stars; the top panel is a histogram illustrating the distinctive metallicity distributions of our high and low [α/Fe] populations. The α-poor population is predominant, with 12,058 members, compared to 3568 α-rich stars.[48]

2.2. *The Asteroseismic Sample*

All of our targets have long-cadence Kepler data, and are in the domain where we expect to be able to detect oscillations. We started with a broad spectroscopic prior for $\nu_{\rm max}$, which we used to identify background sources and reject outlier measurements. We describe the preparation of light curves and the 10 individual pipelines used for asteroseismic analysis in Appendix A. Our method for inferring $\Delta\nu$ and $\nu_{\rm max}$ from the full set of measurements from individual pipelines is described in Appendix B. From these data, we identified a sample with exceptionally high recovery. This was used to set relative $\nu_{\rm max}$ zero-points and weights for individual pipelines. We then did a second outlier pass, rejecting measurements inconsistent with the ensemble data. In this round, some investigators also analyzed the outliers to weed out errors from the automated analysis, and some pipeline results were refined.

We then defined four categories of targets: a Gold sample (five or more valid measurements of both $\Delta\nu$ and $\nu_{\rm max}$); a Silver sample (two to four valid measurements of both $\Delta\nu$ and $\nu_{\rm max}$); a Detection sample (less than two valid $\Delta\nu$ measurements, but two or more $\nu_{\rm max}$ ones); and a Nondetection sample, with less than two $\nu_{\rm max}$ detections. Errors and weights were inferred separately for each group. We returned median and weighted mean values for both $\Delta\nu$ and $\nu_{\rm max}$ for the Gold and Silver samples, and $\nu_{\rm max}$ alone for the Detections.

The APOKASC-2 sample included only stars with $2\ \mu{\rm Hz} < \nu_{\rm max} < 220\ \mu{\rm Hz}$; here, we measure oscillators across the full dynamic range ($0.1\ \mu{\rm Hz} < \nu_{\rm max} < 280\ \mu{\rm Hz}$) where they are detectable with Kepler 30 minute cadence data. We report $\Delta\nu$, $\nu_{\rm max}$, and the asteroseismic surface gravity for all detected stars. However, we only report masses and radii for $1\ \mu{\rm Hz} < \nu_{\rm max} < 220\ \mu{\rm Hz}$ (Section 2.2.1).

However, our goal of recovering the full asteroseismic sample introduces new challenges relative to prior efforts: stars with incomplete data, unusual or suppressed oscillation patterns, and very high or low frequencies of maximum power. All of these populations are important for our study, and we begin by briefly describing the issues in turn. There is a small population of stars where oscillations are not detected even in excellent data. The primary culprit is thought to be stellar activity, which suppresses the amplitude of oscillations as observed in main-sequence stars by W. J. Chaplin et al. (2011) and S. Mathur et al. (2019). J. Tayar et al. (2015) found that rapid rotators were far less common in asteroseismically

---

[46] Of the DR17 giants, 102 were not detected in DR16; this impacts only our spectroscopic evolutionary states for these stars, as discussed below.

[47] In this paper, 65 of the 15,570 targets were discovered to be background asteroseismic detections in this paper, so the spectra do not correspond to the oscillations; these targets are included but not analyzed in detail.

[48] For this, and subsequent plots, we use the [M/H] vector for metallicity, which closely tracks [Fe/H] in practice.

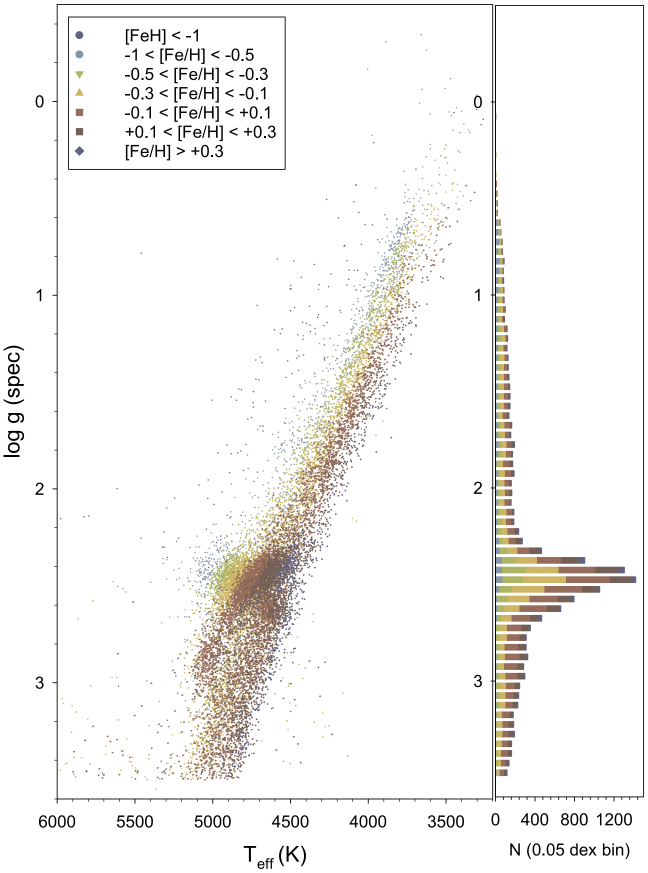

Figure 1. The full APOKASC-3 evolved star sample. The histogram illustrates the number of targets, as a function of metallicity, in 0.05 dex log*g* bins (right).

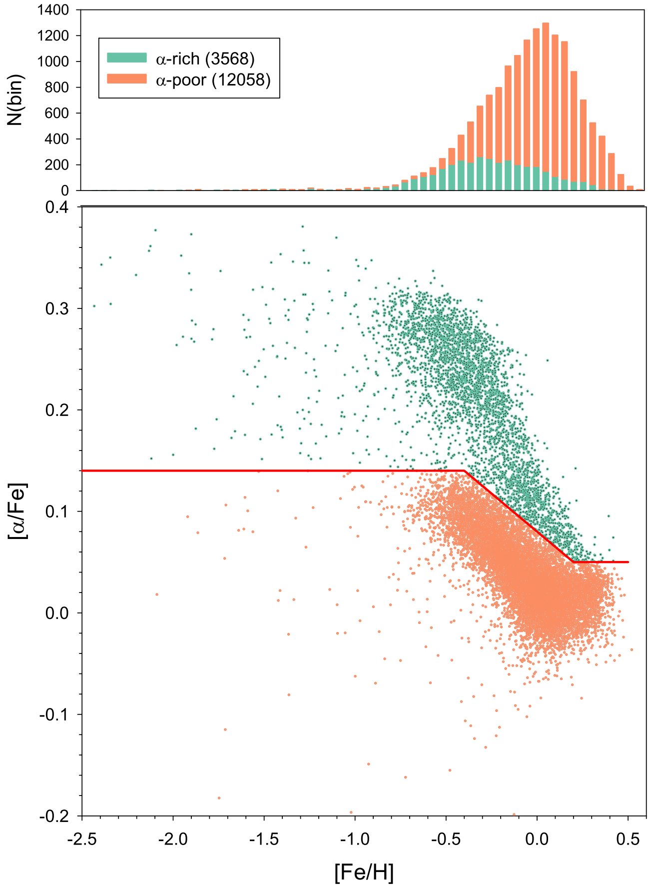

Figure 2. The abundance distribution of the APOKASC-3 sample in the [α/Fe]–[Fe/H] plane. The red line is the criterion that we use to distinguish high [α/Fe] from low [α/Fe] ones. For plotting purposes later in the catalog, we use a slight modification of the J. D. Roberts et al. (2024) criterion for distinguishing the two populations. A star was classified as α-rich if [α/Fe] was above (0.08–0.15[Fe/H]) in the range $-0.4 <$ [Fe/H] $< +0.2$; a threshold of $+0.14$ was assigned for [Fe/H] below -0.4; and a threshold of $+0.05$ was used for [Fe/H] above $+0.2$. Our criterion differs from the J. D. Roberts et al. (2024) one in that we use [α/Fe] and they used [Mg/Fe], including a slight zero-point shift.

detected giants than in the field. P. Gaulme et al. (2020) reported that the vast majority of red giants without detected oscillations despite excellent data belong to close binary systems that are tidally locked. Such systems usually exhibit orbital periods shorter than 50 days. In addition, the fraction of binaries among the stars with partially suppressed oscillations remains significantly larger (≈15%) than for RG oscillators that do not display detectable surface modulation (P. Gaulme et al. 2020).

In some cases, there are also technical issues with light curves, or significant background contaminants. We therefore have examined our sample of nondetections individually, and note where stellar activity or backgrounds are responsible for the lack of a signal. We discuss sample completeness, recovery, and nondetections in Section 2.2.2.

We then inferred masses, radii, and ages for our core sample. This required knowledge of evolutionary state, discussed in detail in a companion paper (M. Vrard et al. 2024). Our evolutionary states are discussed in Section 2.2.3. We discuss unusual targets (background sources and those without spectra) in Section 3.5. Our mass, radius and age inference procedures, which require stellar interior models and calibration to a fundamental system, are described in Section 3.

2.2.1. *Low and High $\nu_{\rm max}$ Targets*

Our asteroseismic approach breaks down in the low- and high-frequency domains. On the high-frequency side, we have to consider the Nyquist sampling limit for 29.4 minutes long-cadence data, which is 283.447 μHz (J. M. Jenkins et al. 2010). There is therefore an expected population with $\nu_{\rm max}$ below this level. However, for stars close to this boundary, the true spectral power will extend above the Nyquist limit, leading to a distorted power spectrum and a reduced amplitude for $\nu_{\rm max}$ close to the sampling limit. As seen in Figure 24 (Appendix B), systematic differences between methods diverge above 220 μHz, which we take as the limit where different analysis techniques are required. Near- and super-Nyquist asteroseismology is the subject of a separate paper (B. Liagre et al. 2025, in preparation).

Along the RGB, the amplitude of the modes increases and $\nu_{\rm max}$ decreases as surface gravity drops. Detecting oscillations is therefore straightforward in luminous giants with a sufficiently long time series, which is typically true for the Kepler sample. However, for these stars, precise asteroseismic characterization becomes progressively more difficult as $\nu_{\rm max}$ decreases. There are fewer detected modes; although peaks in the power spectrum are narrower, their relative width, scaled to $\Delta\nu$, increases when $\Delta\nu$ decreases (G. Dréau et al. 2021), making it hard to resolve individual mode frequencies. It is also difficult to define a consistent system relative to higher $\nu_{\rm max}$ for a sparse set of modes, which is important for measuring $\Delta\nu$. For the lowest frequencies, light-curve systematics are also important. These challenges are reflected in measurement differences between methods, which grow as $\nu_{\max}$ drops (Appendix B).

The mapping of $\nu_{\max}$ onto mean density also becomes more challenging in low $\nu_{\max}$ stars, because we can observe only with low radial order n, where the asymptotic approximation in scaling relations becomes a poor one. This departure is accounted for in our $f_{\Delta\nu}$ factor, but there are significant differences between different $f_{\Delta\nu}$ approaches at low $\nu_{\max}$ (Section 3.1). Finally, there are known to be significant offsets between asteroseismic and fundamental radii for luminous giants (J. C. Zinn et al. 2019b, 2023).

For all of these reasons, we believe that the classical scaling relation approach is not the correct approach for the most luminous giants in our sample, and adopt $\nu_{\max}$ of 1 μHz as our threshold. This is the characteristic $\nu_{\max}$ where B. Mosser et al. (2013) first detected a change in the oscillation frequency regime. D. Stello et al. (2014) also found that the low radial order modes (n <5 below 1 μHz) seen in these stars produce a highly nonuniform pattern even in theoretical models, further complicating analysis. We therefore provide ensemble averaged $\nu_{\max}$, $\Delta\nu$, and asteroseismic log$g$ for giants with 0.1 μHz < $\nu_{\max}$ < 1 μHz, but not masses and radii.

2.2.2. Overall Asteroseismic Recovery

We present our four groups of targets—Gold, Silver, Detection, and Nondetection—in Figure 3. The lines close to log$g$ of 1 and 3.3 denote characteristic $\nu_{\max}$ of 1 and 220 μHz, respectively, which define the domain where we infer mass, radius, and age. Stars without spectra and ones where the asteroseismic detection does not correspond to the spectroscopic source are not shown. Virtually all stars in the RC and on the lower RGB are in the high-quality Gold sample. The Silver sample extends to lower surface gravity than the Gold sample does. The spike in the Silver sample at high gravity is caused by the difficulty in detecting signal when $\nu_{\max}$ is close to the sampling frequency.

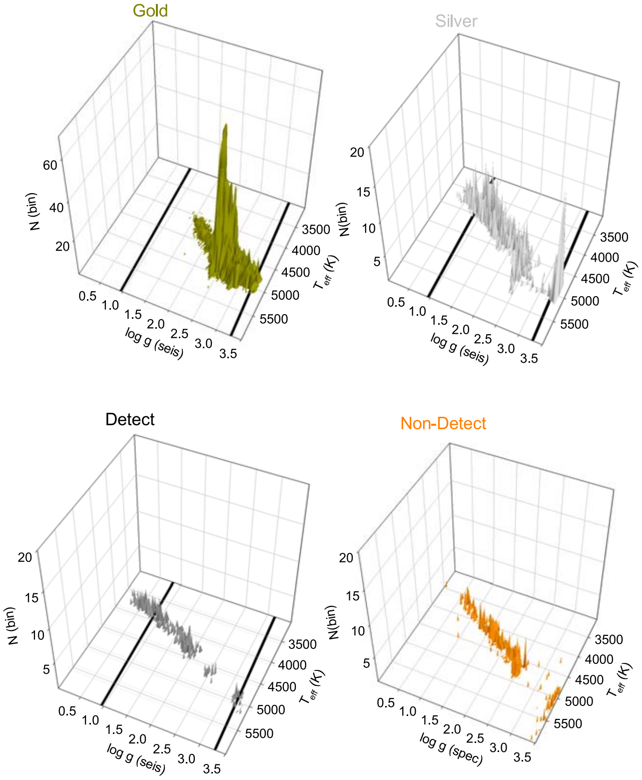

Figure 3. Our four cohorts—Gold (top left), Silver (top right), Detections (bottom left), and Nondetections (bottom right)—illustrated in 3D mesh plots as a function of log$g$ and spectroscopic T_{eff}. We use seismic log$g$ for all categories except Nondetections, for which we use spectroscopic log$g$. The horizontal lines denote the approximate boundaries where we report masses and radii (between log$g$ of 1 and 3.3). Bin sizes of 40 K in T_{eff} and 0.02 dex in log$g$ reflect typical measurement uncertainties. The vertical scale for the Gold bin is higher than for the other panels. The large majority of lower RGB and RC stars are robustly detected. In the detected groups, we also note the number of stars with detections that are outside the domain where we provide masses, ages, and radii. In total, we have 12,448 targets with full data, 1634 with partial data, and 1423 without seismic data. Background sources (129) and stars without valid spectroscopic data (174) are not shown.

The nondetections and marginal detections are spread out across the log$g$ domain. We do not report full data for 20% of the sample, even though the Kepler sample is the highest-quality asteroseismic data set currently in existence. Kepler had a relatively large aperture, bright targets, and more than 4 yr of continuous data, which was downloaded in 90 day segments referred to as quarters. The majority of our targets (13,543) had continuous data for 3+ quarters of the mission, including 9970 with 13 or more quarters. However, because some red giant stars were not explicitly included as planet search candidates, they were observed sporadically or infrequently; stars with <3 quarters of data are difficult to recover signals from. Figure 4 shows our recovery as a function of $\nu_{\max}$ for targets with 1–2 quarters of data (left) and 3–18 quarters (right). For our core sample (1–220 μHz), 9,869 (80.4%) of the stars with 3+ quarters of data were in the Gold sample, with only 123 (1%) being nondetections. By contrast, of the stars with 1–2 quarters of data, there were 826 nondetections (40.1%) and 182 Gold sample stars (8.8%). The APOKASC-2 sample was selected to emphasize stars with high-quality light curves, and we obtained consistent results for almost all of those targets.

Stars without asteroseismic detections are nonetheless interesting objects, so we performed a manual analysis of targets. We identified plausible reasons for nondetections in all cases. A total of 965 of the nondetections had <3 quarters of data; in many cases, this was actually less than one full quarter of data. There were 242 stars with predicted $\nu_{\max}$ (from spectra) below 1 μHz, a domain where detection is challenging. An additional 147 stars had a predicted $\nu_{\max}$ (from spectra) above 283 μHz, close to the Nyquist sampling rate. 262 stars not in these categories still had no detections, including 78 targets without good spectroscopic fits.

Of these, 29 stars had two oscillation power excesses, indicating either a true double giant system or a contaminating signal from a background source. In all cases, one of the peaks is close to the value predicted by spectra. These stars could be real binaries, but the majority of them are usually the result of a background star in the aperture, which contaminates the light curve of the main target.

The amplitude of the asteroseismic modes is known to be reduced in rapidly rotating cool giants (e.g., R. A. Garcìa et al. 2010; W. J. Chaplin et al. 2011; A. R. G. Santos et al. 2018; S. Mathur et al. 2019; P. Gaulme et al. 2020). Rapid rotation is also associated with cool spots that can induce a photometric variability signal. For 69 stars, we do not detect modes, but can see spikes at low frequency that appear to correspond to the

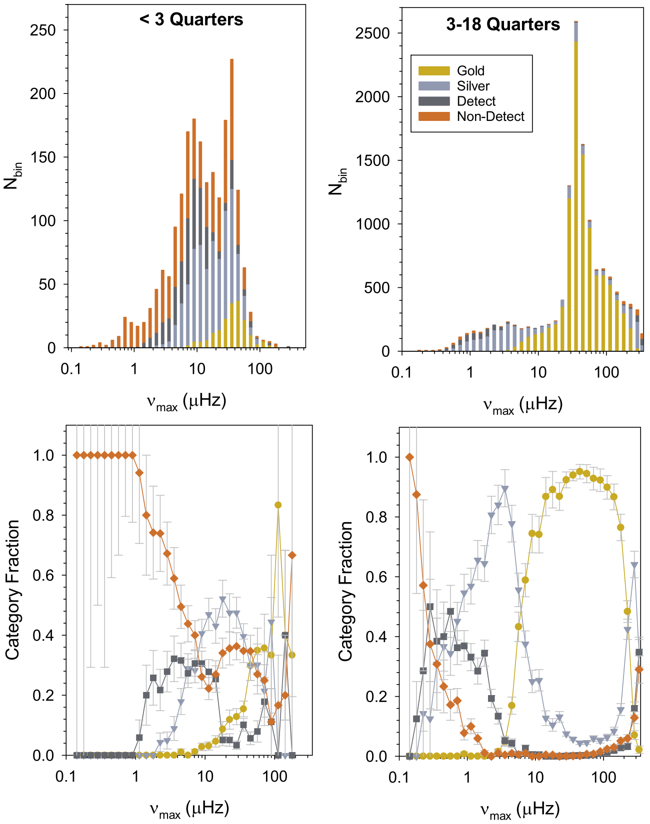

Figure 4. Our four cohorts—Gold (dark yellow, circles), Silver (light gray, triangles), Detections (dark gray, squares), and Nondetections (orange, diamonds)—illustrated as a function of spectroscopic $\nu_{\max}$ for stars with <3 quarters of data (left) and for those with 3–18 quarters (right). Absolute numbers are in the top panels, and fractions in the bottom panels. The large majority of stars with good data are detected in our core domain of 1–220 μHz, while recovery is much more difficult for shorter time series.

rotation of the star. We attribute these nondetections to mode suppression caused by rotation and activity.

We also have a sample of 87 stars where we can see signatures of transits or eclipses, preventing us from detecting the modes. Detailed work, outside of the scope of this paper, is required to interpret these light curves.

Finally, some power spectra present spurious spikes that can be due to instrumental issues or to the modes of classical pulsators from faint background sources. There are 79 stars in this category. We note that some stars were in more than one category. See Section 3.5 for a further discussion on outliers. We summarize the properties of our nondetections and outliers in Table 1.

2.2.3. Evolutionary States

He-core burning (RC) stars and stars with degenerate cores (RGB and AGB) exhibit distinct frequency patterns that can be clearly identified in the long-duration time-series data provided by space missions (T. R. Bedding et al. 2011; B. Mosser et al. 2011a). After this was discovered, a number of automatic methods to distinguish RGB from clump targets with asteroseismology were developed. In this section, we present a summary of how we used those techniques to assess the evolutionary status of stars. The complete description of the method is presented in M. Vrard et al. (2024).

We used six different methods that automatically determine the evolutionary status of red giant stars (T. Kallinger et al. 2012; M. Vrard et al. 2016; M. Hon et al. 2017; Y. Elsworth et al. 2019; B. Mosser et al. 2019; J. S. Kuszlewicz et al. 2020), one of them with two different codes. In some cases, different approaches predicted different states for the same star. Some methods are based on direct inferences about core properties, which require higher-quality data; others are based on parameters correlated to evolutionary state, which can be performed with moderate-quality data. The indirect techniques were weighted less heavily in the final classification when their results conflicted with direct techniques, similar to the approach used in Y. Elsworth et al. (2019).

With those criteria, we manage to obtain a classification for 11,371 stars in the APOKASC sample (4755 identified as RC and 6616 identified as RGB or AGB). The RC category includes more-massive core He-burning stars, both those fainter than the RC and sometimes referred to as the secondary RC, and the brighter intermediate-mass ones. Manual checks confirmed that the seismic evolutionary status identification was very reliable and robust when it disagreed with the spectroscopic state. We also had an agreement between the spectroscopic and seismic classification better than 94% of the time.

M. Vrard et al. (2024) also investigated asteroseismic and spectroscopic methods for separating H-shell only (RGB) stars and double shell-burning objects (AGB) stars. Asteroseismic techniques were in agreement with spectroscopic state inferences close to the RC, but were found to diverge for more luminous stars. For stars with $\Delta\nu \leqslant 2$ μHz, the disagreement between the different techniques becomes close to 50%; thus, the asteroseismic classification cannot be reliably assessed for luminous stars. In the APOKASC-3 catalog, we therefore treated shell-burning sources as potential AGB stars for log$g$ below 2.2; as AGB stars do not appear at higher log$g$, we classified all higher gravity shell-burning sources as RGBs.

However, AGB stars are hotter than RGB stars at the same surface gravity. The temperature difference is significant just above the RC and becomes small toward the tip of the RGB. We can therefore assign spectroscopic AGB or RGB evolutionary states to some stars above the RC, as shown in Figure 5. These assignments affect the inferred ages, as discussed in Section 3.3. For details of the approach used, see M. Vrard et al. (2024).

3. Mass, Radius, and Age

The asteroseismic scaling relations (Equations (1) and (2)) require corrections for precise work. The mean asteroseismic properties themselves are also subject to method-dependent offsets and trends. A calibration against fundamental data is therefore essential in our view.

We use stellar models and pulsation theory to define a star-by-star correction factor $f_{\Delta\nu}$ to interpret the observed frequency spacings. The $\nu_{\max}$ scaling has a strong underlying physical basis, tied to the relationship between the acoustic cutoff frequency and the surface gravity (K. Belkacem et al. 2011). A predictive theory, however, requires advances in our understanding of the excitation, damping, and reflection of modes. It is therefore not currently practical to define star-by-star corrections for $\nu_{\max}$. In practice, both the measurement systematics and the offsets between asteroseismic and fundamental radii are well-behaved functions of $\nu_{\max}$. Motivated by

Table 1
Outlier Categories

KIC	STARCAT	SEISB	ROT	EB	BadTS	HighN	LowN	Nomodes	Short
1434395	SilverOl	0	0	1	1	0	0	0	0
1864258	NoDetOl	0	0	0	0	0	1	0	0
1872749	DetectOl	0	0	0	0	1	0	1	0
2010051	LowNmax	0	0	0	0	0	1	0	0
2015616	DetectOl	0	1	0	0	0	0	1	0

Note. We present only the first five rows; remaining entries are available online. KIC is the KIC ID, and STARCAT is the category the outlier is found in. The next eight columns are toggles indicating the class of behaviors for which the light curve was flagged (1 = yes, 0 = no). Objects could be flagged for more than one reason. SEISB = double-peaked power spectrum; ROT = strong stellar rotation signal; EB = Eclipsing Binary; BadTS = either pollution by a background source or a pathologicial time series; HighN = $\nu_{\rm max}$ above or close to Nyquist; LowN = $\nu_{\rm max}$ below 1 μHz; Nomodes = no clear detection; Short = 1 or fewer quarters of data. Note that we do not list the nondetections with short time series; the Short category was only used for initial detections for which we identified contradictory or poor results.

(This table is available in its entirety in machine-readable form in the online article.)

this result, we define an empirical $f_{\nu\rm max}$ function that serves to calibrate our radius system.

Our method assumes that offsets between fundamental and asteroseismic radii are caused by departures from the $\nu_{\rm max}$ scaling relation; in general, they could arise from errors in the $\Delta\nu$ scaling relation or the $T_{\rm eff}$ scale, which could inject errors in the masses even if the radii are calibrated. Ages are model-dependent, and we use stellar interior models to infer ages from spectroscopic and asteroseismic data. We therefore compare different weighting methods for inferring $\Delta\nu$ from theoretical frequency spectra, and different stellar models for computing the power spectra and inferring ages. This exercise allows us to quantify uncertainties arising from the models used to interpret the data.

In APOKASC-2, our primary calibrators were members of the open star clusters NGC 6791 and NGC 6819. There was limited overlap with eclipsing binary and interferometric samples, which remains true in the current sample, so these stars were not used as primary calibrators. A new tool is now a greatly expanded set of stars with reliable radii from Gaia. We use these data to define a correction function $f_{\nu\rm max}$ that brings asteroseismic radii into statistical agreement with Gaia radii, inferred from knowledge of L and $T_{\rm eff}$.

3.1. Mapping $\Delta\nu$ to Mean Density: Inferring $f_{\Delta\nu}$

The observed oscillation pattern depends in detail on the internal structure of the star. In principle, it is possible to predict, identify, and fit individual frequencies. This approach, sometimes referred to as peak-bagging, has been employed for detailed studies of individual stars, and for stars in the open cluster NGC 6819 (R. Handberg et al. 2017). However, it is difficult to predict amplitudes from first principles, and real power spectra are complicated by mixed modes and rotational splittings. Even for the radial modes, there are known offsets between observed and predicted frequencies, even in the Sun (J. Christensen-Dalsgaard & M. J. Thompson 1997), that can be traced to poorly understood outer layer physics and near-surface reflection effects. See Y. Li et al. (2023) for a recent discussion of this surface correction in the Kepler context. Carefully chosen combinations of frequencies can mitigate these effects.

Here, we collapse the frequency pattern down to a single figure of merit, $\Delta\nu$, which is proportional to the square root of the mean density in the asymptotic limit of large radial order n and a structure homologous to the Sun. In real stars, neither is strictly true. We correct for this by defining

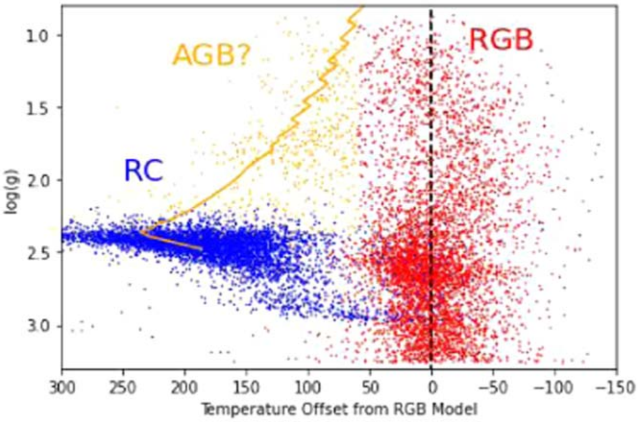

Figure 5. Temperature offset, as defined in M. Vrard et al. (2024), relative to the mean RGB locus as a function of asteroseismic surface gravity for our upper RGB sample. The RC stars are shown in blue, RGB stars are red, and AGB stars are yellow. A 1 solar mass, solar metallicity MIST AGB track is shown for reference as a yellow line.

$$f_{\Delta\nu}^2 = \frac{\langle\rho\rangle}{\Delta\nu^2} \tag{3}$$

and solving for it as described in the method sections below.[49] We then took the inferred asteroseismic radii to define a $f_{\nu\rm max}$ function, which perturbs the assigned asteroseismic gravities, and repeated the calibration exercise. For all models, we adopt the APOKASC-2 solar zero-point of 135.1416 μHz for $\Delta\nu$. We also adopt 3076 μHz as the reference point for the solar $\nu_{\rm max}$; the $f_{\nu\rm max}$ scaling is defined relative to this value.

To infer $f_{\Delta\nu}$, we need to choose stellar interiors models to produce theoretical frequency spectra. These model frequencies have to be converted into a $\Delta\nu$ that would have been observed from the model spectrum by choosing a subset of modes and assigning weights to spacings between individual modes. The difference between this predicted $\Delta\nu$ and the true mean density is then used to infer $f_{\Delta\nu}$. Following APOKASC-2, we adopted the Garstec models and the Mosser weighting approach. However, we explored two different stellar evolution codes, and two different weighting schemes, to explore systematic uncertainties.

---

[49] We note that both $f_{\Delta\nu}$ and $f_{\nu\rm max}$, discussed below, are sometimes defined in the literature in the opposite sense.

1. *Sharma models and Weightings*. The *asfgrid*[50] $f_{\Delta\nu}$ scheme (S. Sharma et al. 2016) uses a grid of MESA v6950 models generated with the 1M_pre_ms_to_wd test suite case (B. Paxton et al. 2011, 2013, 2015). Models were run without rotation, overshooting, diffusion, or mass loss. Convection was treated according to the J. P. Cox & R. T. Giuli (1968) mixing length prescription. Opacities were generated from OPAL (C. A. Iglesias & F. J. Rogers 1993, 1996) using N. Grevesse & A. J. Sauval (1998) solar abundances, with C/O enriched abundance mixtures assumed for helium burning. In the low-temperature regime, molecular opacities are adopted from J. W. Ferguson et al. (2005). Asteroseismic frequencies of the radial modes are then computed using GYRE v3.1 (R. H. D. Townsend & S. A. Teitler 2013). A local measurement of $\Delta\nu$ in the vicinity of $\nu_{\rm max}$ is performed as the slope of a linear fit to the radial mode frequencies versus their mode order using a Gaussian weight function centered on $\nu_{\rm max}$, following T. R. White et al. (2011). The $f_{\Delta\nu}$ term is defined as the ratio between the asymptotic and local $\Delta\nu$, and tabulated as a function of evolutionary state, [Fe/H], $T_{\rm eff}$, $\nu_{\rm max}$, and $\Delta\nu$ (D. Stello & S. Sharma 2022).
2. *Garstec models, White and Mosser Weightings*. Our base case in APOKASC-2 used GARSTEC (A. Weiss & H. Schlattl 2008) models, which we also adopt here. GARSTEC models use OPAL radiative opacities (C. A. Iglesias & F. J. Rogers 1996) complemented at low temperature with molecular and dust opacities from the Wichita group (J. W. Ferguson et al. 2005) and conductive opacities from Potekhin as updated in S. Cassisi et al. (2007). The equation of state is FreeEOS (A. W. Irwin 2012). Hydrogen-burning reaction cross sections are taken from Solar Fusion II (E. G. Adelberger et al. 2011), and helium-burning reaction rates are from NACRE (C. Angulo et al. 1999). Stellar atmospheres are computed using the VAL-C T-τ relation from J. E. Vernazza et al. (1981). Convection is modeled according to the mixing length theory, following the J. P. Cox & R. T. Giuli (1968) implementation, and the mixing length parameter is fixed following the calibration of a standard solar model, which, in combination to the T–τ relation, leads to $\alpha_{\rm MLT} = 2.012$. Models with masses $<1.25 M_\odot$ include gravitational settling, following A. A. Thoul et al. (1994). The efficiency of gravitational settling is artificially decreased for masses between $1.25 M_\odot$ and $1.35 M_\odot$, with a suppression factor increasing linearly from 0 to 1 in that range, and it is neglected for larger masses. The impact of this simplification for the structure of RGB stars is small. Turbulent mixing below the convective envelope is modeled diffusively, with the diffusion coefficient based on the parameterization from D. A. VandenBerg et al. (2012). Convective over/undershooting is modeled using the diffusive approach (B. Freytag et al. 1996), and the free parameter fixed to $f = 0.02$ in all convective boundaries. To avoid the well-known problem of large overshooting regions in very small convective cores, f is decreased from its standard value down to 0 in the convective cores of models in the mass range $1.4 M_\odot$ to $<1 M_\odot$. The solar mixture is from N. Grevesse & A. Noels (1993); therefore, $(Z/X) = 0.02439$ is used to define the spectroscopic solar reference abundance, $[{\rm Fe/H}] = 0$. The metallicity and helium enrichments are assumed to follow a linear relation such that $Y = Y_{\rm BBN} + (\Delta Y)/\Delta Z)Z$, and $\Delta Y/\Delta Z = 1.15$ as determined from $Y_{\rm BBN} = 0.2485$ and our solar calibration. Mass loss is modeled using Reimers' prescription with the free parameter fixed to $\eta = 0.2$.

   For each stellar model, version 0.3b of ADIPLS (J. Christensen-Dalsgaard 2008) is used to compute all radial modes with frequencies lower than the acoustic cutoff frequency. The $\Delta\nu$ term is obtained as the slope of a weighed linear fit to the frequencies of the radial modes as a function of mode order. The weighting function represents a Gaussian distribution of power, centered in $\nu_{\rm max}$, and characterized by a FWHM value. Two possibilities have been considered for the latter: the prescription by T. R. White et al. (2011) in which ${\rm FWHM} = 0.25\nu_{\rm max}$, and the empirical determination obtained by B. Mosser et al. (2012), for which ${\rm FWHM} = 0.66\ \nu_{\rm max}{}^{0.88}$ for $\nu_{\rm max}$ expressed in μHz. The value of $\Delta\nu$ is then used as in Equation (3) to compute $f_{\Delta\nu}$ for all of the models in the grid.

   The grid of stellar models ranges from 0.6–5.0 $M_\odot$, with mass step of 0.02 $M_\odot$ in the range 0.6–3 $M_\odot$, and 0.04 $M_\odot$ for larger masses. [Fe/H] spans from −2.5 up to +0.6 dex, with steps of 0.05 dex, up to 3 $M_\odot$, and from −1.0 up to +0.6 for masses between 3 and 5 $M_\odot$. The chemical mixture is always solar-scaled. For this work, in BeSPP, α-enhancement is taken into account by using a modified [Fe/H] value computed as $[{\rm Fe/H}]_{\rm corr} = [{\rm Fe/H}] + 0.625\ [\alpha/{\rm Fe}]$. This is analogous, and quantitatively similar, to other transformations, such as the one from M. Salaris et al. (1993).

   We then employ a Bayesian inference code, BeSPP, to interpret the model grid. BeSPP assumes a Salpeter mass function and a constant star formation rate as priors, and posterior distributions are obtained by marginalization as described in A. M. Serenelli et al. (2013). The process for determining $f_{\Delta\nu}$ is as follows: $\Delta\nu$, $\nu_{\rm max}$, and $T_{\rm eff}$ are used to obtain the seismic log$g$, and an initial guess for the stellar mass using scaling relations and setting $f_{\Delta\nu} = 1$. The input set of variables in BeSPP therefore is log$g$, $[{\rm Fe/H}]_{\rm corr}$, and the stellar mass along with their respective errors. These are used to construct the posterior distribution of $f_{\Delta\nu}$, which is used to refine the stellar mass and then used to start the new iteration. Convergence is defined as $f_{\Delta\nu}$ varying less than one part in 10^5. Note that this is different from the traditional grid-based modeling in several respects. In particular, the $T_{\rm eff}$ scale in stellar models is not used at all, as $T_{\rm eff}$ is only used in scaling relations and not in the construction of any likelihood.

The derived correction factors for RC and RGB stars are illustrated in Figures 6 and 7, respectively. There is a significant difference between RC and RGB stars; the degenerate cores of AGB/RGB stars are more different from the Sun than the lower-density RC stars, inducing a larger change in the relative scalings. Our applied corrections therefore require knowledge of the evolutionary states. In the absence of a well-defined state, we consider both solutions and adopt a larger uncertainty in the derived masses and ages.

Different weighting schemes and choices of models give very similar results for the lower RGB and the main RC populations.

---

[50] The *asfgrid* code is publicly available at http://www.physics.usyd.edu.au/k2gap/Asfgrid/.

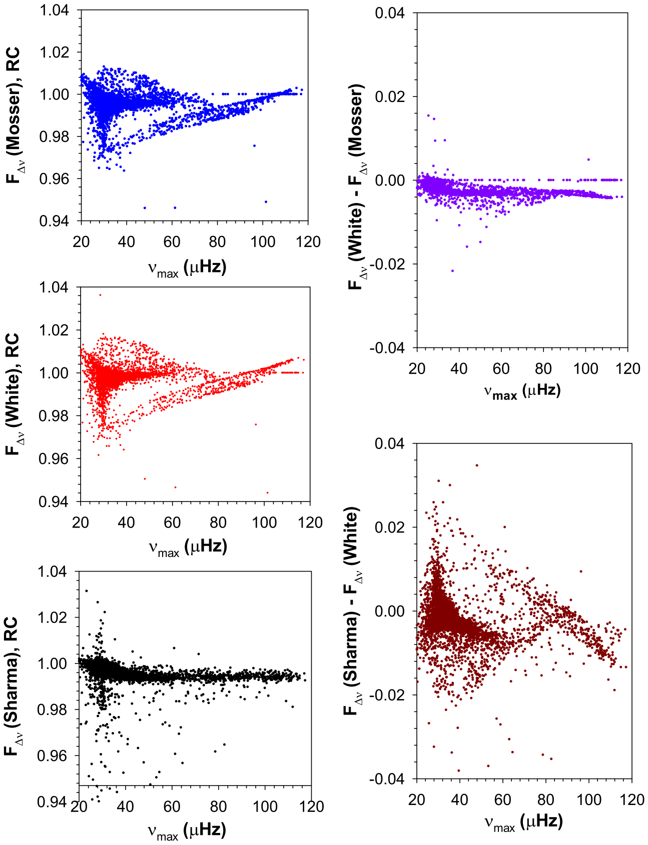

Figure 6. Frequency-spacing corrections for RC stars using the Garstec+Mosser (top left), Garstec+White (middle left), and Sharma+White (lower left) models and weights. Differences between Garstec+Mosser and Garstec+White (top right) measure the impact of the assigned weighting scheme. Differences between Garstec+White and Sharma+White measure the impact of the models used. For a minority of stars, the true log*g* range of the sample did not correspond to the range in the model grid, which is responsible for some of the structures seen in the BeSPP results.

We can therefore conclude that our predicted asteroseismic masses and radii for these stars are insensitive to the method used to map the data onto mean density. However, relative offsets between methods become significant in low $\nu_{\max}$ stars. If left unaddressed, this would induce method-dependent trends in the mass and radius scale as a function of $\nu_{\max}$. We address this by calibrating our absolute results to a fundamental reference system, which by construction places all three methods on a common zero-point and removes the relative trends seen in the left panels of Figures 6 and 7. For the lower RGB and in the main RC, we use the scatter in $f_{\Delta\nu}$ to infer the error arising from the method used to infer $f_{\Delta\nu}$. For these domains, the scatter induced by the choice of weights (×0.001) is less than that induced by the choice of models (0.005). We therefore take 0.005, as a minimum random error source for $f_{\Delta\nu}$. This is comparable to that induced by the uncertainty in the $\Delta\nu$ measurements themselves for high-quality data, which illustrates the importance of theoretical models for interpreting the pulsation frequencies.

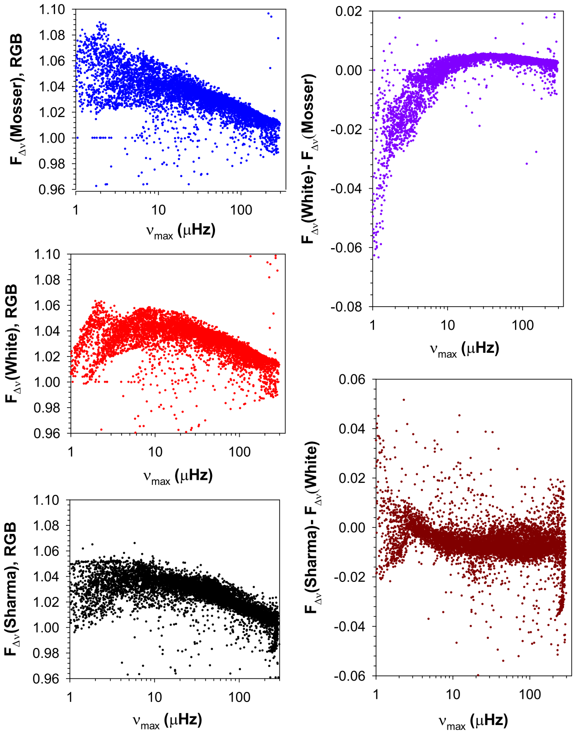

Figure 7. Frequency-spacing corrections for RGB stars using the Garstec+Mosser (top left), Garstec+White (middle left), and Sharma+White (lower left) models and weights. Differences between Garstec+Mosser and Garstec+White (top right) measure the impact of the assigned weighting scheme. Differences between Garstec+White and Sharma+White measure the impact of the models used.

3.2. Asteroseismic and Gaia Radii: Inferring $f_{\nu\max}$

At this point, we are in a position to compute radii and masses. The zero-point of the $\nu_{\max}$ scaling relation is formally the solar value. As discussed in APOKASC-2, however, the solar values differ between pipelines, and there is a poor correspondence between relative measurements in different pipelines and the relative solar values. In APOKASC-2, the zero-point of 3076 μHz was set by calibrating on masses of open cluster stars in NGC 6819 and 6791. This calibration, however, does not address any potential systematics as a function of evolutionary state or surface gravity.

Gaia parallaxes, combined with photometry, bolometric corrections, and an extinction map, can be used to infer luminosities. When combined with $T_{\rm eff}$ from APOGEE, we can then solve for R, hereafter Gaia radii. Asteroseismic radii, which do not depend on parallax, can then be compared with these radii that do. This combination was used as a test of the absolute $T_{\rm eff}$ scale and the Gaia zero-point for DR2 (J. C. Zinn et al. 2019a) and DR3 (J. C. Zinn 2021).

Given the dependence of $f_{\Delta\nu}$ on $\nu_{\max}$, it is plausible that a $\nu_{\max}$ correction, $f_{\nu\max}$, also depends on $\nu_{\max}$. For RGB stars, which span several orders of magnitude in $\nu_{\max}$, we therefore implemented an empirical calibration. Binned means of the asteroseismic-Gaia radius ratio for RGB stars were taken as a function of $\nu_{\max}$, and are shown in Figure 8. A third-degree polynomial was then fit using least-squares as implemented in *numpy*, giving each bin equal weight. The fit was anchored to the ratio of the radii at a $\nu_{\max}$ of 50 μHz. The asteroseismic radii were then corrected according to this polynomial, with separate corrections performed for each $f_{\Delta\nu}$ scale. This calibration can be thought of as a calibration of $\nu_{\max}$, since $R_{\rm seis} \propto \nu_{\max}$. The resulting calibration of $f_{\nu\max}$ is

$$f_{\nu\max} = (1 + p)^{-1}, \tag{4}$$

where

$$p = a(\ln\nu_{\max})^3 + b(\ln\nu_{\max})^2 + c(\ln\nu_{\max}) + d, \tag{5}$$

Table 2
Fit Coefficients and Zero-points for Our Three Methods for Inferring Mean Density

MODEL	WEIGHT	$\mathrm{FNM_{RC}}$	$\mathrm{FNM_{RGB}}$	a	b	c	d
SHARMA	WHITE	0.9941	0.9893	−0.00989448	0.08085812	−0.18509446	0.08986743
GARSTEC	MOSSER	0.9937	0.9959	−0.00556347	0.04268084	−0.07452754	−0.02442568
GARSTEC	WHITE	0.9985	1.0032	−0.00758535	0.06330463	−0.14603078	0.05336784

Note. The underlying stellar models are in column (1), and the weighting scheme is in column (2). Zero-points for the RC (column (3)) and RGB (column (4)) are the total scale factors relative to the APOKASC-2 value of 3076 μHz. Polynomial coefficients a, b, c, and d, as described in the text, are in columns (5)–(8).

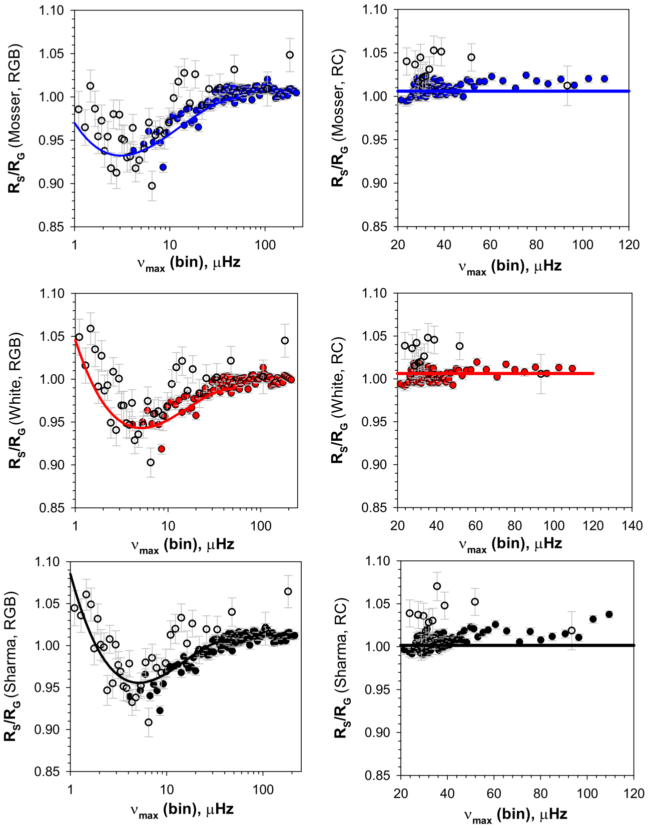

Figure 8. The ratio of asteroseismic to Gaia radii for our sample. Rows denote results using different methods: the Garstec+Mosser (top), Garstec+White (middle), and Sharma+White (bottom) models and weights. RGB stars are shown on the left and RC on the right. Data points are 50 star bins, defined in a rank-ordered list in $\nu_{\rm max}$. Silver sample bins are open points, and Gold sample bins are closed points. The $\nu_{\rm max}$ dependent fits to the RGB data are shown with the lines in the left panel.

with $\nu_{\rm max}$ in μHz, and is defined for $1.1 < \nu_{\rm max} < 50$ μHz. We adopt a fixed zero-point for $\nu_{\rm max} > 50$ μHz on the RGB and a separate one for the RC. The polynomial coefficients and zero-points are provided in Table 2 for each of the $f_{\Delta\nu}$ scales. This calibration brings the asteroseismic radii and the Gaia radii into alignment for stars up to $R \approx 50 R_\odot$. We adopt the GARSTEC +Mosser $f_{\Delta\nu}$ values as our default case, which was the one used in APOKASC-2. The lower RGB and RC zero-points for the Mosser scale are the equivalent of an effective solar $\nu_{\rm max}$ of 3063 and 3057 μHz, respectively.

Figure 8 compares Gaia radii to asteroseismic radii. We rank order stars in $\nu_{\rm max}$ and show averages for 50 star bins. The three left panels show RGB data adopting different $f_{\Delta\nu}$ methods (from top to bottom, Garstec+Mosser, Garstec+White, and Sharma+White); the three panels on the right show RC stars using the same methods. Open symbols are the Silver sample, and closed ones are the Gold sample.

Asteroseismic radii are in excellent agreement with fundamental data in the RC and the lower RGB. However, there are clear, and highly significant, deviations between asteroseismic radii and fundamental data in lower $\nu_{\rm max}$ RGB stars; furthermore, the magnitude of the offsets depends on the method used to infer $f_{\Delta\nu}$. The lines in our left panels represent the fits, using the coefficients in Table 2.

There are also offsets between the Silver and Gold RC samples, but they are of marginal statistical significance. The Silver RC sample is quite small, with large uncertainties, as most Kepler RC stars have high-quality data. Given the lack of a significant trend in $\nu_{\rm max}$ for the RC, a constant $\nu_{\rm max}$ zero-point was used for the RC.

Our fit differs from that used in APOKASC-2, which was based on masses in the open clusters NGC 6791 and NGC 6819. However, our system does produce results in good agreement with open cluster data. In a companion paper focused on luminous giants, A. L. Ash et al. (2025) found mean lower RGB and RC masses in NGC 6791 of 1.15 ± 0.01 and $1.12 \pm 0.01 M_\odot$, respectively, in excellent agreement with the M. H. Pinsonneault et al. (2018) fundamental mass of $1.15 \pm 0.02 M_\odot$. For NGC 6819, average lower RGB and RC masses were 1.65 ± 0.02 and $1.64 \pm 0.02 M_\odot$, respectively, roughly 2σ higher than the $1.55 \pm 0.04 M_\odot$ value adopted by APOKASC-2. However, we note that our values are close to those obtained by R. Handberg et al. (2017; 1.61 ± 0.02 and $1.64 \pm 0.02 M_\odot$ for the RGB and RC, respectively). We discuss our systematic and random error models in Section 3.4.

3.3. Masses and Ages

3.3.1. Masses

For masses, we adopt the $f_{\Delta\nu}$ and $f_{\nu_{\rm max}}$ data from above for all three of our $f_{\Delta\nu}$ methods, which gives us three different mass scales. For consistency with APOKASC-2, we choose to use the Garstec+Mosser corrected mass scale as our base case, and provide the alternative options in Table 5. We discuss population tests of our mass scale and uncertainties in Section 4.2. The J. Yu et al. (2018) data set is the largest homogeneous comparison set for asteroseismic masses, and provides a good check on our results. They focused on stars with $\nu_{\rm max} > 5$ μHz and used the SYD pipeline (Appendix A.2.3), which is one of the ones used in our study. In order to make a comparison with the J. Yu et al. (2018), we focus on the Gold sample, which describes the large majority of stars in that domain. We compare our data with Yu et al. in Figure 9. To quantify the comparison, it is useful to divide the sample into three cohorts: RC, lower RGB ($\log g > 2.5$),

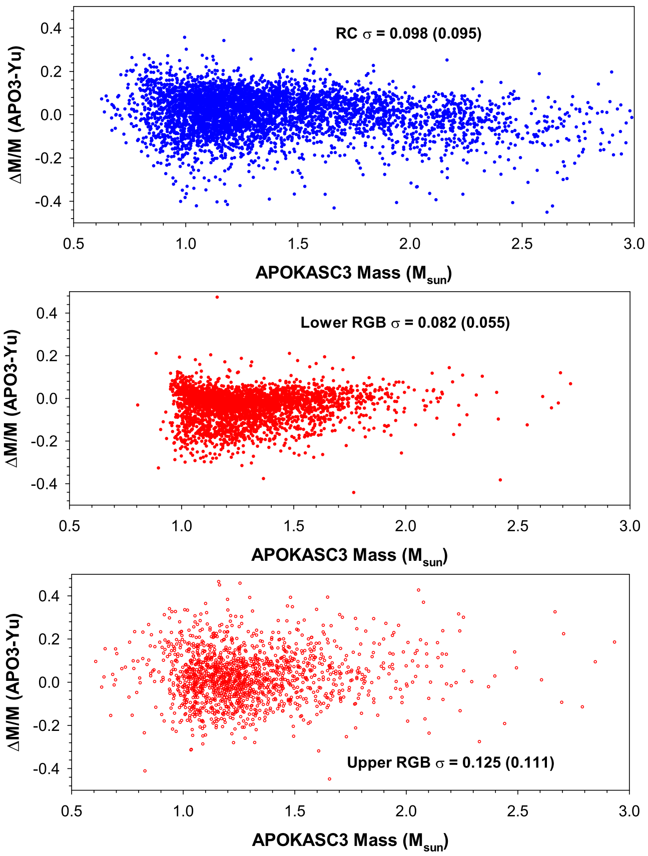

Figure 9. APOKASC-3 and Yu masses compared for Gold sample stars in the RC (top), lower RGB (middle), and upper RGB (bottom). Errors in each panel are the standard deviation and the median absolute deviation (MAD) converted to σ (in brackets).

and upper RGB ($\log g < 2.5$). The median fractional mass differences for these three groups are modest (+0.016, −0.023, and +0.022 for the RC, LRGB, and URGB, respectively); the dispersion is larger (0.098, 0.082, and 0.125, respectively).

The J. Yu et al. (2018) masses are in good average agreement with ours, which is expected because the underlying asteroseismic data is on a similar scale. The derived asteroseismic parameters from SYD are in excellent mean agreement with our system (Table 8 in Appendix B), with zero-points in $\nu_{\max}$ and $\Delta\nu$ within 0.1% of our mean. J. Yu et al. (2018) used the Sharma+White model for inferring $f_{\Delta\nu}$. This method, as shown in Figures 6 and 7, is close to our central value for the Gold sample $\nu_{\max}$ range.

We can trace the mass differences to larger measurement uncertainties in a single method relative to an ensemble average. The scatter of the SYD pipeline around our ensemble mean is ~0.015 in $\nu_{\max}$ and $\Delta\nu$ for the Gold sample, which by itself would produce a predicted scatter in mass around our relationship of 0.075 $M_\odot$. The remainder of the mass scatter can be explained by the nonseismic data. J. Yu et al. (2018) adopted a heterogeneous sample of $T_{\rm eff}$ and [Fe/H] literature measurements, and only had a modest subset of 5678 APOGEE measurements available; the data was also from DR12, and there have been substantive changes to APOGEE since that time. Photometric $T_{\rm eff}$ measurements have large random uncertainties (M. H. Pinsonneault et al. 2012), and are subject to systematics from the adopted extinction map, and $T_{\rm eff}$ is a direct ingredient of the scaling relations. [Fe/H] has an indirect effect on photometric $T_{\rm eff}$ and on $f_{\Delta\nu}$. We therefore believe that the differences shown here can be traced to known effects.

Overall, we believe that our ensemble averaging method produces more precise data, and should be used in preference to single pipeline results when available. We explore the stellar population results more fully in Section 4.2. We also note that the Yu sample did not report masses for 695 of the Gold sample stars; we report results for these stars because our ensemble method allows us to recover signals in targets missed by individual pipelines. Conversely, the Yu sample includes stars without APOGEE spectra, which makes it of comparable size overall (16,094) to APOKASC-3.

3.3.2. Ages

We use stellar evolution models to infer ages from the measured mass, surface gravity, and composition. However, stellar ages are intrinsically model-dependent. We also explore several different methods for doing so. The first option for estimating the ages, and our reported base case, is most similar to the method used for APOKASC-2. In this case, the seismically inferred stellar mass and surface gravity are used, and the metallicity and α-enhancement are combined into the corrected [Fe/H] as described in Section 3.1.

The corrected metallicity, the seismic mass, and $\log g$ are then used as inputs in our Bayesian code BeSPP, discussed in Section 3.2, to determine the stellar age. No prior was used with respect to the initial mass function when inferring ages, it being used before to determine the seismic mass. We use the stellar models described in Section 3.1. A priori, the stellar age and uncertainties could then be determined directly from the posterior distribution function. However, a typical problem that may arise is a lack of consistency between age and mass estimates originating in the nonlinear relation between mass and age. To avoid this, for any given star, we have carried out three runs in BeSPP: one using the seismic mass as input, and two others using the seismic mass increased and decreased by its uncertainty, respectively. In each case, very small mass errors are used in BeSPP to avoid nonlinear effects in the age posterior distribution. The age determined from the posterior distribution function in the first case is taken as the central value of the stellar age, and the standard deviation is adopted as the statistical uncertainty linked to [Fe/H] and $\log g$ errors. The age values determined in the two other runs are defined as the lower and upper 1σ uncertainties after quadratically combining them with the induced [Fe/H] and $\log g$ errors.

We measure only the current mass in our sample; stars that have experienced significant mass loss had a higher birth mass, and therefore a younger age than the one we would infer in the absence of mass loss. The standard Reimers mass-loss rate we have used is defined by assuming that a fraction η of the luminosity is used to provide the lost gravitational potential energy associated with a stellar wind; $\eta L = -\frac{GM}{R}\frac{dM}{dt}$. We adopted $\eta = 0.2$ for our initial calculations. Low-mass stars experience much more mass loss than high-mass stars, as seen in the bottom panel of Figure 10. This effect means that low-mass AGB stars had a higher birth mass, and therefore a younger age, at a given current mass (top panel, Figure 10). Higher-mass stars have little mass loss, but are actually *older* at fixed mass in the AGB phase as opposed to the RGB phase. In this case, there is minimal mass loss, and the AGB star is older because it has lived through both the core-H and core-He-burning phases.

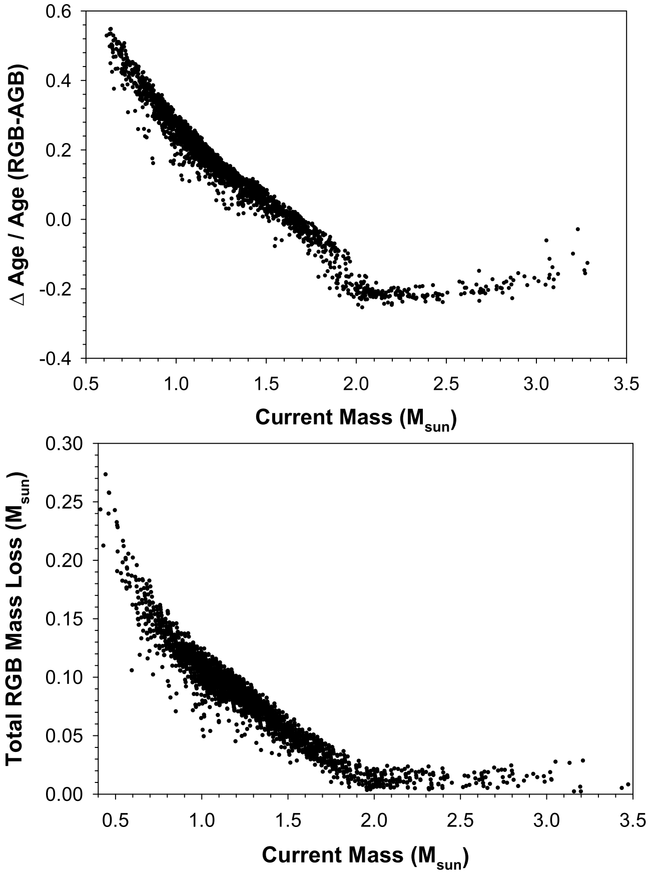

Figure 10. Fractional difference in age between AGB and RGB stars (top) and the total mass loss on the RGB (bottom) as a function of the current mass of the star. Low-mass stars experience much more mass loss.

We use the α-rich population to validate our mass-loss model (see Section 4.2). In brief, the large majority of the stars in that population have similar ages, and therefore the difference in mass between RC and RGB stars is a reasonable diagnostic of mass loss, which is $0.10\,M_\odot$ for our sample. This corresponds to an effective Reimers $\eta = 0.17$, which we adopt as a central value. The RC population has a larger dispersion in mass and age than the RGB precursors, which is consistent with a dispersion in mass loss of $0.03\,M_\odot$. This is equivalent to a dispersion in η of 0.05, which we propagate into an enhanced age uncertainty for the RC population.

We therefore define our ages in three domains. On the lower RGB, noninteracting stars are not expected to experience significant mass loss. On the RC, stars have in general experienced mass loss in the prior RGB phase. Upper RGB stars are a mixture of first-ascent giants and AGB stars; the latter have, to a first approximation, the same degree of mass loss as RC stars. We discuss population tests of our mass-loss model in Section 4.2.

The majority of luminous giants are on the first ascent of the RGB because hydrogen burning is much more efficient than helium burning, but a significant fraction of about one-sixth are AGB stars. In most cases, the RGB age will therefore be applicable, but the two populations have significant overlap in the HR diagram. However, we can use $T_{\rm eff}$ to distinguish between the two in some domains, as shown in Figure 5. We provide two sets of ages for shell-burning stars above the RC that cannot be reliably sorted into AGB or RGB alone.

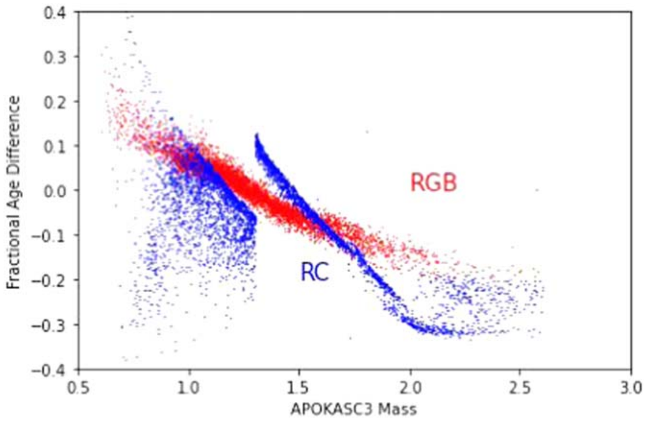

Figure 11. Difference between our main (GARSTEC) and alternative (YREC) ages for both RGB stars (red) and clump stars (blue), in the sense GARSTEC-YREC. Mass loss becomes important in low-mass stars, while differences in convective overshoot treatment are significant for higher masses. Systematics are at the 10 % level for the majority of the RGB stars, and somewhat larger for more-massive RC stars. The sharp edge in the clump offsets comes from the assumptions about mass loss in the alternative (YREC) ages.

Stellar ages are subject to significant systematic uncertainties. In low-mass stars, assumptions about mass loss are important, as shown in Figure 10. In higher-mass stars, the model-dependent treatment of convective cores has a strong impact on the main-sequence lifetime, and therefore on the age on the RGB or RC. To quantify this, we have computed independent models for ages, following the method described in J. Tayar et al. (2017). Here the mass, surface gravity, [M/H], and $[\alpha/{\rm M}]$ are interpolated in a grid of models build using the YREC code (P. Demarque et al. 2008). These models assume no core overshoot, an N. Grevesse & A. J. Sauval (1998) mixture, no gravitational settling, and a gray atmosphere. For these stars, an empirical calibration of the metallicity-dependent mass-loss is assumed for clump stars with masses below $1.3\,M_\odot$ using the same formulation as J. Tayar et al. (2023), namely $\Delta M = (0.12([{\rm M/H}] + 1.0)^2 + 0.95) - (0.3[{\rm M/H}] + 1.0)\,M_\odot$. Mass loss is not included for age inferences in higher-mass RC stars or any RGB stars. For this interpolation, the ages are estimated as if all of the stars are on the first-ascent RGB. Because we included neither mass loss nor core overshooting in these models, the differences are a measure of the systematics from these effects.

Even with these simplifications, as shown in Figure 11, we find surprisingly good agreement. For RGB stars, there are trends at the ±10% level, with YREC ages being higher at low mass and lower at high mass). Typical masses on the lower RGB are $\sim 1.4\,M_\odot$, so the progenitors of these stars had a small or absent main-sequence convective core, and little mass loss is expected for them. These insensitivities explain our modest differences. At higher masses and younger ages, the differences in overshoot are important, but little mass is expected to be lost. At lower masses and older ages, choices about gravitational settling are important, as are the assumptions about mass loss for RC and upper RGB stars.

3.4. Uncertainties

Our error model begins with a formal error based on measurement uncertainties, such as $\nu_{\rm max}$, $\Delta\nu$, $T_{\rm eff}$, and $f_{\Delta\nu}$. We confirm these by population and external checks on mass, radius, and age. Systematic uncertainties are tied to those in the

Table 3
Adopted Uncertainties (Third Column) for Our Key Spectroscopic Observables (First Column)

Category	Units	Adopted σ	DR17 σ	DR17-DR14 Median	DR17-DR14 σ	DR16 σ	DR17-DR16 Median	DR17-DR16 σ
$T_{\rm eff}$	kelvin	0.53 DR16	8.6	−7.7	23.4	85.6	−11.4	21.7
log$g$ (spec)	dex	0.065	0.024	0.031	0.069	0.053	0.023	0.053
[Fe/H]	dex	0.05	0.007	−0.075	0.019	0.007	−0.023	0.020
[α/Fe]	dex	0.02	0.006	0.021	0.028	0.007	0.025	0.022

Note. We also include the median random error in DR17 (fourth column), median difference between DR17 and DR14 (fifth column), and the dispersion between them (sixth column). The seventh, eighth, and ninth columns are the median random error in DR16, median difference between DR16 and DR14, and the dispersion between them. Note that we do not adopt the DR17 $T_{\rm eff}$ errors where available; instead we adopt random errors of 0.53 times the DR16 errors. Stars without DR16 errors are treated as discussed in the text.

calibration system and model-dependent inferences (such as $f_{\Delta\nu}$ and the stellar interiors models used to infer age from mass, composition, and evolutionary state). We discuss these effects and their impact next, and summarize the outcome of external tests at the end.

3.4.1. Uncertainties in Asteroseismic Properties

Our error model is similar to that used in APOKASC-2. We take the scatter of individual pipeline measurements of asteroseismic properties around the mean as a measure of random error. We also assume that the uncertainties are uncorrelated, taking the standard error of the mean as our measurement error for $\Delta\nu$ and $\nu_{\rm max}$. We provide alternative uncertainties in Appendix B for those who wish to use other measures.

The dispersion between calibrated $f_{\Delta\nu}$ values is another measure of random uncertainty. From Figures 6 and 7, it may appear that these could be quite large; however, our calibration ties these to a common value and the dispersion in calibrated mass and radius values induced by the method for inferring $f_{\Delta\nu}$ is much smaller than the pre-calibration scatter. When combined with uncertainties in $T_{\rm eff}$ described below, these error sources are propagated in quadrature to infer an overall uncertainty in mass and radius.

3.4.2. Systematic and Random Spectroscopic Uncertainties

For this catalog, we adopt APOGEE DR17 central values (Abdurro'uf et al. 2022) where available. Asteroseismic measurements are independent of the spectroscopic ones. However, uncertainties in $T_{\rm eff}$ propagate directly into ones for radius and mass. In addition, we need to know the stellar composition to properly map the observed $\Delta\nu$ onto mean density and to infer ages.

Changes between data releases are a good check on systematic and random errors. M. H. Pinsonneault et al. (2018) used results from DR14, while the current effort uses results from DR17. The overlap samples, for DR17 giants, are 12,888 (DR14) and 15,422 (DR16). In order not to be biased by a small number of large changes, we used median statistics, and converted the median absolute deviation (MAD) to an effective σ (for a normal distribution, MAD $= 1.4826\sigma$).

We present our results in Table 3. These properties for our sample are comparable to those derived from the full data releases (T. Spoo et al. 2022).

Systematic scale differences are small for $T_{\rm eff}$ and log$g$ because they are tied to absolute reference systems. Random errors for both are important, and provided by APOGEE for all spectroscopic measurements. The notional DR17 uncertainties are much smaller than those in prior releases. Based on the dispersion in results between data releases alone, we argue that the DR17 uncertainties are underestimated. For more realistic errors, we use external comparisons.

For $T_{\rm eff}$, we take advantage of a robust feature of our sample: the temperature offset between RC and RGB stars (J. A. Holtzman et al. 2018); see also M. Vrard et al. (2024). The RGB locus has well-defined $T_{\rm eff}$ trends with log$g$, mass, and [Fe/H]. When these trends are removed, there is a clear separation between RC and RGB stars that is a weak function of stellar observables. We also have independent asteroseismic techniques for evolutionary classification, which can in turn be used to train spectroscopic state diagnostics. If the errors were as large as the quoted DR16 ones, we would expect a much higher rate of incorrect spectroscopic states than what we see. The observed false-positive rate is consistent with a median $T_{\rm eff}$ error of 45 K, corresponding to 0.53 of the DR16 errors. We adopt this scaled version of DR16 uncertainties for our $T_{\rm eff}$ uncertainty. For stars without DR16 data, we inflate the DR17 errors by a factor of 5, which is the ratio of the mean $T_{\rm eff}$ uncertainties in the two data releases.

Spectroscopic log$g$ errors are important for detecting background sources not associated with the APOGEE target and rejecting outlier measurements. We therefore discuss them more fully in Appendix B. Our adopted error in Table 1 is inferred from the dispersion derived from the MAD between APOKASC-2 asteroseismic data and DR17 spectroscopic values.

For abundance errors, both systematic and random uncertainties are important, as we are comparing observed abundances to absolute abundances in theoretical models. Revisions between data releases induce larger shifts than the quoted random errors in DR17. We adopt 0.05 dex for [Fe/H] and 0.02 dex for [α/Fe] as minimum uncertainties for the purpose of comparing models to data, which are characteristic of the offsets seen between methods. For [C/N], used for the evolutionary state specification, we adopt the DR17 values, as the $T_{\rm eff}$ errors are the largest component of the error budget for state inference.

3.4.3. Systematic Radius and $T_{\rm eff}$ Uncertainties

Our comparisons between Gaia radii and asteroseismic radii are a test of the error model. We focus on RGB stars with $\nu_{\rm max}$ between 50 and 200 μHz. The Gold sample stars have a scatter not much larger than that expected from errors in the Gaia radii alone; this indicates that our predicted uncertainties in the asteroseismic radii are reasonable. The scatter in the Silver sample is larger than that expected from the Gaia radii, consistent with the larger scatter for these that that we expect from the error model. We attempted to use the error budget to infer a scale factor for the radius, and by extension mass, estimates; however, the derived results are not robust to outliers, and are sensitive to the treatment of large astrometric errors. As a consequence, we can claim that our errors are consistent with this check, but we do not attempt to calibrate them on the joint data.

External comparisons are also useful for quantifying the systematic uncertainties in the APOGEE temperature scale. Given that APOGEE is calibrated to the fundamental IRFM scale (P. González Hernández & P. Bonifacio 2009), the absolute accuracy of the temperatures is set by that of the IRFM system. P. González Hernández & P. Bonifacio (2009) found that their giant temperature scale agreed to within 40 K when compared to the independent A. Alonso et al. (1994) temperature scale for stars with $[\mathrm{Fe/H}] > -0.4$, which we take as a 2σ systematic uncertainty on temperature. In practice, we adjust the zero-point of our seismic radius scale to agree with Gaia radii, making our results insensitive to the absolute T_{eff} zero-point.

3.4.4. Systematic Uncertainties Arising from the Gaia Radius Calibration

The asteroseismic radius systematics are best considered in three separate regimes: stars with $R < 30R_{\odot}$, stars with $R > 30R_{\odot}$, and stars with $[\mathrm{Fe/H}] < -1$. The majority of stars in our sample fall into the first category. These stars have systematics set by the Gaia calibration we perform and the temperature systematics discussed above. The Gaia systematics arise from zero-point offsets in the parallax scale, which are documented to be position-, color-, and magnitude-dependent (L. Lindegren et al. 2021; S. Khan et al. 2023). The DR3 parallax scale appears to have a global offset of 15 μas with respect to asteroseismic parallaxes (J. C. Zinn 2021), which would translate to a 2% systematic uncertainty in radius. Temperature systematics are smaller than this, and so the parallax uncertainty dominates the systematic uncertainty in asteroseismic radii via their calibration to Gaia. We therefore estimate that our calibration of $f_{\nu\mathrm{max}}$ is accurate to 2% for the large majority of the sample.

Radius systematics are larger than 2% for the minority of stars with large radii or low metallicities. Stars with $50\,R_{\odot} > R > 30\,R_{\odot}$, corresponding to $1\,\mu\mathrm{Hz} < \nu_{\mathrm{max}} < 4\,\mu\mathrm{Hz}$, have radii that disagree with Gaia radii at up to the 10% level before calibration. Although our fit corrects for these deviations, it is important to understand the physical origin of these differences (J. C. Zinn et al. 2023). Stars with $[\mathrm{Fe/H}] < -1$ are in a domain where the IRFM has limited data, and there is the possibility of systematic offsets in the underlying T_{eff} scale, as discussed in J. Schonhut-Stasik et al. (2024) for the APO-K2 catalog. Although metallicity is accounted for in the $f_{\Delta\nu}$ factor, it is not in the ν_{max} scaling relationship. Theoretical considerations would also predict that the asteroseismic ν_{max} scaling relations could be sensitive to mean molecular weight, and thus metallicity (L. S. Viani et al. 2017); however, in APOKASC-2, the data did not show evidence for a metallicity-dependent systematic offset in the close to solar metallicity domain. We therefore caution that our results may be subject to larger systematic errors in the large-radius and low-metallicity domain than for the bulk of the sample.

3.4.5. Systematic Mass and Age Uncertainties

Our calibration method places asteroseismic and Gaia radii on a common absolute scale. Formally, however, this is only a constraint on the product of $f_{\nu\mathrm{max}} T_{\mathrm{eff}}^{1/2} f_{\Delta\nu}^{-2}$. It is therefore possible that some of the offsets captured in this term could arise from errors in T_{eff} or $f_{\Delta\nu}$, rather than being an offset in the ν_{max} scaling relation. In the limit where the ν_{max} relation is correct, and the error is in the $\Delta\nu$ relationship alone, the mass correction would scale with ${f_{\nu\mathrm{max}}}^{2}$; our approach, assigning the full error to ν_{max}, scales with ${f_{\nu\mathrm{max}}}^{3}$. There is therefore a systematic scale factor error of order $f_{\nu\mathrm{max}}$ in our masses, which is related to the origin of the radius offset. For the vast majority of our sample, this effect is small, but it becomes important in more luminous RGB stars (see below).

Our mass and radius uncertainties are taken from the quadratic sum of the uncertainties in $\Delta\nu$, ν_{max}, T_{eff}, and $f_{\Delta\nu}$. Similarly, the age uncertainties are taken from the uncertainties in mass and composition. However, there are domains where systematic errors can be significant, and where the assumptions used in our error model can break down. We therefore test our results in several different ways (Section 4.2). The mean masses and mass scatter in star clusters are a test of whether our radius-based reference system produces sensible masses, and whether our error model produces sensible uncertainties. The properties of the α-rich population, which can be treated as a pseudo-cluster in some respects, also provide interesting tests. In this case, the small observed age dispersion in the lower RGB, the relative ages of the RC and RGB, and the mass difference between them are all consistent with our overall model (A. L. Ash et al. 2025).

For the more luminous stars, $f_{\nu\mathrm{max}}$ deviates significantly from unity, so there are larger systematic uncertainties. We see evidence of differences in age relative to lower RGB stars of 17%–37% for moderate- and high-luminosity α-rich stars, corresponding roughly to mass offsets of 6%–12%. These stars are a mix of AGB and RGB stars, and population effects could be important, so we do not believe that this is sufficient grounds to revise the underlying system.

3.5. Outliers and Rotation

Any large astrophysical sample will contain outliers, and ours is no exception. Some of these objects are of genuine astrophysical interest, but many are simply the result of automated analysis of large data sets. We therefore individually examined the light curves and analysis for a subset of 201 stars in unusual regimes of phase space or with unusual ensemble asteroseismic properties. Common issues included more than one asteroseismic target in the aperture, typically from chance alignments; eclipsing binaries; artifacts in the light curves; power spectra polluted by background classical pulsators, typically producing high spikes in Fourier space; and rotation. These stars were classified as outliers. Some targets also had very low or high ν_{max} outside of our calibration domain. In all of these cases, we did not provide mass, radius, or age. However, 37 of these stars were confirmed to be valid measurements with interesting properties. A total of 114 Silver sample stars and 12 Gold sample stars were classified as outliers, with the remainder as detections. We summarize the categories below. Table 1, presented earlier, includes these results.

1. *Super-Nyquist Stars.* Forty-nine of our candidates were confirmed in B. Liagre et al. (2025, in preparation) as detections above the Nyquist limit. Of these stars, 39 were in our Silver sample. We treat all as outliers for this paper, classify them as HighN stars, and do not provide asteroseismic properties for them in this paper.
2. *High Scatter.* Sixty of our candidates had unusually high measurement scatter in $\nu_{\max}$. Of these, 14 were valid measurements. Many of the others were double or multiple sources (14) and eclipsing binaries (8). The remainder were classified as nondetections.
3. *Stars below the RC.* RC stars cluster in a narrow range of radii, and smaller stars are unexpected and interesting. The large majority of RC stars had asteroseismic states, but a minority did not. Stars with RC state assignments based only on spectra were more likely to have spurious measurements, and we discuss them separately from seismic states. We had 11 spectroscopically classified RC stars below $6.5\,R_\odot$. Of these, none were true RC stars, and none were confirmed as true asteroseismic detections at all. Of 32 stars with RC spectroscopic states, mass below $1\,M_\odot$, and radius between 6.5 and $10.5\,R_\odot$, five were valid. However, six out of 11 small RC stars with asteroseismic evolutionary states are confirmed as true RC stars.
4. *Unusually Massive Stars.* Very massive stars are rare, but present. We looked at 28 RC stars with masses above $3.5\,M_\odot$ and 34 RGB stars with masses above $3\,M_\odot$. Of these stars, 26 were rejected as false positives; however, we do find truly massive stars in our data. In the catalog, there are 97 stars with masses above $3\,M_\odot$, roughly evenly split between RC and RGB, 28 of which are in our Gold sample. The highest mass cohort (above $3.5\,M_\odot$) has 36 stars. An interesting number of these stars may be post-main-sequence mergers (S. Deheuvels et al. 2022). Our data set has a number of targets in common with the recent C. L. Crawford et al. (2024) study of 48 high-mass stars, although our mass estimates are systematically lower than those in that study for stars in common.
5. *Low-mass RGB Stars.* Below the RC, there is little mass loss expected in RGB stars, and the finite age of the Galaxy imposes a maximum age and minimum mass. We therefore expect a metallicity-dependent, but sharp, lower bound on the mass distribution. We checked 17 stars with mass below $0.9\,M_\odot$ and radius below $10\,R_\odot$; of these, two were valid, including one metal-poor star for which a lower mass is reasonable. Very low stellar masses are also suprising, even on the upper RGB; of 52 stars with formal masses below $0.5\,M_\odot$ at any $\log g$, none were found to be valid asteroseismic measurements.

There is another unique population of stars that makes up 4.0% of the APOKASC-3 sample.[51] These 631 rotationally enhanced giants were originally reported in R. A. Patton et al. (2024) and have $v \sin i$ values between 5 and $75\,\mathrm{km\,s^{-1}}$, 5+ times faster than the typical rotation speed expected for a giant (e.g., J. K. Carlberg et al. 2011). We note that 113 stars have $v \sin i > 10\,\mathrm{km\,s^{-1}}$, the typical literature threshold for defining rapid rotation in giants; this corresponds to 0.7% of our sample. There is significant evidence that the intermediate and rapid rotator cohorts have distinct properties (R. A. Patton et al. 2024).

The spectra used to estimate $v \sin i$ came from APOGEE DR16, and we included estimates for giants whose spectra made it past one or both rounds of spectral fitting in ASPCAP. We cannot estimate $v \sin i$ for giants that were rejected by the pipeline from the outset. Further details on how the giants were selected and how $v \sin i$ was estimated are in R. A. Patton et al. (2024).

It is well established that rapid rotation can suppress seismic signals (P. Gaulme et al. 2020), which we see in our population of rotationally enhanced giants. Figure 12 shows the distribution of $v \sin i$ for giants with and without even a partial seismic detection. Of the 631 rotationally enhanced giants, 316 have complete seismic detections (derived mass and radii) and 184 have partial detections. Unsurprisingly, the vast majority of the rotators with seismic detections rotate more slowly, peaking in the 5–$10\,\mathrm{km\,s^{-1}}$ range and extending up to $20\,\mathrm{km\,s^{-1}}$, except for a few outliers. Of the 91 stars with $v \sin i > 10\,\mathrm{km\,s^{-1}}$ and good spectral fits, only 15 have derived masses, including no RGB stars and no stars with $v \sin i > 15\,\mathrm{km\,s^{-1}}$.

Rapid rotation is not expected in red giants because of spindown caused by mass loss and expansion. Rotationally enhanced giants either did not spin down as much during the main sequence or were spun up. Spin-up can occur in binaries either through merging with a companion or by tidal synchronization. R. A. Patton et al. (2024) found a high binary fraction for rotationally enhanced red giants in the field, but were limited in their assessment of binarity in the APOKASC-3 sample due to many targets having only one visit from APOGEE.

Nevertheless, many of these stars likely have experienced binary interaction. This unique population spans the giant branch and clump, as shown in Figure 12. The majority of the sample is in the RC, consistent with their being upper RGB interaction products. Interestingly, most of these RC stars are low mass, as seen in the lower panel. As another intriguing data point, the majority of the upper RGB detections do not show evidence of a current binary companion, suggesting that they could be in postmerger systems. The rotationally enhanced giants with seismology provide a unique opportunity to probe the internal structure of stars, in various evolutionary states, with unusual histories.

4. The APOKASC-3 Catalog

We now turn to presenting the full set of catalog data. For ease of use, we separate our results into three full tables. Table 4 contains our recommended values for key parameters. Our algorithm for doing so is as follows:

1. *Identifiers*. We include the KIC ID, Gaia DR3 ID, and Two Micron All Sky Survey (2MASS) ID for each target. The latter is used as a unique identifier for the APOGEE survey.
2. *Evolutionary State*. We adopt asteroseismic states when available, and spectroscopic states when they are not. Stars without valid spectra do not have assigned states.

---

[51] Note that the number of stars reported here is less than what originally appeared in R. A. Patton et al. (2024). This is due to differences in selection criteria for giants ($\log g < 3.85$ in R. A. Patton et al. (2024) and $\log g < 3.5$ in this work) and which APOGEE data release the spectra came from. Note also that in R. A. Patton et al. (2024) 15,220 giants were identified, whereas the giant catalog presented here contains 15,808 stars. This is again due to differences in selection criteria. Giants only made the APOKASC-3 main catalog if they had complete spectroscopic solutions in DR17, whereas R. A. Patton et al. (2024) used spectroscopic stellar parameters from DR16.

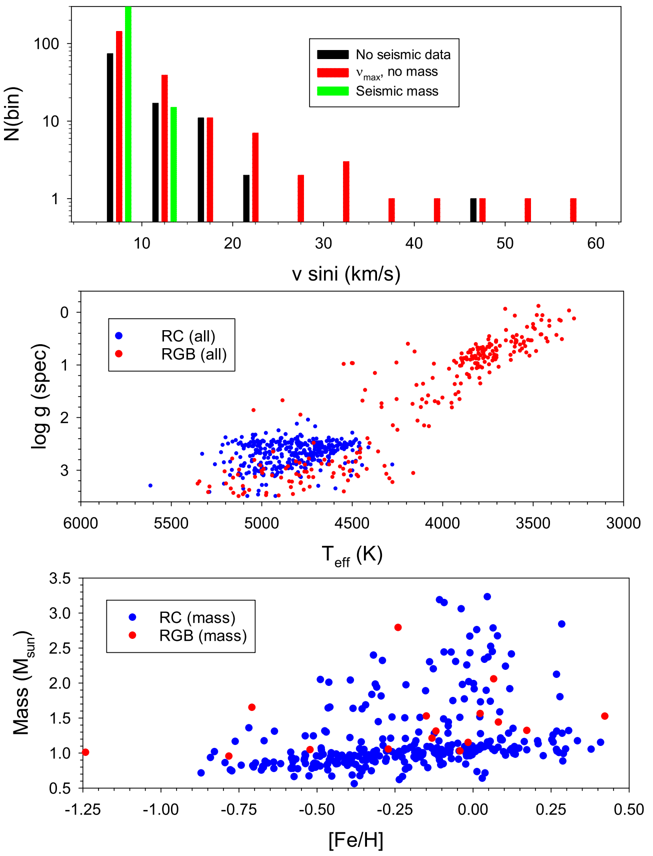

Figure 12. The distribution of $v \sin i$ for giants without a seismic detection (black), with partial data (red), and with full seismic data (green) are shown in bins of 5 km s^{-1} in $v \sin i$ in the top panel. Stars of different type are slightly offset at the same bin location for clarity. In the middle panel, we present spectroscopic log g vs. $T_{\rm eff}$ taken from APOGEE DR17 for the rotationally enhanced giants. The RC stars are plotted as blue circles and first-ascent giants are plotted as red ones. In the bottom panel, we show mass as a function of [Fe/H] for the sample with full asteroseismic data.

Table 4
Catalog of Recommended Stellar Properties

Label	Contents
KIC ID	Number in the Kepler Input Catalog
EvolState, ESSource	Evolutionary state and source
CatTab	Category
SeisSource	Seismic weighting scheme
SpecSource	Spectroscopic data release
NNumax	Number of filtered $\nu_{\rm max}$ values
NDnu	Number of filtered $\Delta\nu$ values
NQuar	Quarters of Kepler data
Numax, SNumax	$\nu_{\rm max}$ (μHz) and σ
Dnu, SDnu	$\Delta\nu$ (μHz) and σ
FDnu, SFDnu	Mosser $f_{\Delta\nu}$ and σ
Fnumax	Mosser $f_{\nu {\rm max}}$
Mass, SMass	Mosser mass ($M_\odot$) and σ
Radius, SRadius	Mosser radius ($R_\odot$) and σ
Loggseis, Sloggseis	Mosser seismic log$g$ (cgs) and σ
Teff, STeff	$T_{\rm eff}$ and σ (K)
Loggspec, Sloggspec	Spectroscopic log$g$ (cgs) and σ
FeH, SFeH	[Fe/H] ([M/H]) and σ
AlpFe, SAlpFe	[α/Fe] and σ
CFe, SCFe	[C/Fe] and σ
NFe, SNFe	[N/Fe] and σ
InvRGaia, SInvRGaia	MIST K $\frac{1}{R_{\rm Gaia}}$ and σ
RecAge	Recommended age class
AgeRGB	Garstec age (Gyr), RGB
SAgeRGB+,SageRGB-	± Garstec age σ (Gyr), RGB
AgeRC	Garstec age (Gyr), RC or AGB
SAgeRC+, SAgeRC-	± Garstec age σ (Gyr), RC or AGB
Vsini	$v \sin i$ (km s^{-1})
α Class	As defined in the Figure 2 caption
Gaia ID	Number in the Gaia Catalog
2MASS ID	Number in the 2MASS Input Catalog

Note. See the text for details.

(This table is available in its entirety in machine-readable form in the online article.)

For a small minority of stars, we had only DR17 data and not DR16 (the latter was used to assign states); in this case, some stars were assigned RC/RGB states if they were in the log$g$ domain where both populations are present. Stars classified as dwarfs or subgiants are not included in the table. We also specify whether the state was derived from spectra or asteroseismology.

3. *Category*. We only present masses, radii, and ages for stars in the Silver and Gold samples. To be included in either sample, $\nu_{\rm max}$ must be between 1 and 220 μHz, the source must not be flagged as a background source or one with poor asteroseismic measurements, and it must have a valid spectroscopic solution. Silver sample stars have between two and four valid measurements of $\nu_{\rm max}$ and $\Delta\nu$. Gold sample stars have five or more measurements of both. A minority of both classes were classified as outliers, with anomalies in the measurements from automated methods; we do not present masses and radii for these targets, and they are labeled SilverOL and GoldOL, respectively. Stars with a $\nu_{\rm max}$ inconsistent with the spectroscopic value are categorized as Background. Stars with $\nu_{\rm max}$ below 1 μHz and two or more valid asteroseismic measurements are classified as LowNMax. Stars with $\nu_{\rm max}$ above 220 μHz and two or more valid measurements are classified as HighNMax (B. Liagre et al. 2025, in preparation). Stars with less than two valid $\Delta\nu$ measurements, but at least two $\nu_{\rm max}$ measurements, were classified as detections (Detect); only $\nu_{\rm max}$ entries are included. Entries with poor data are classified as DetectOL. Nondetections are split into two groups: NoDetSh are ones with less than 3 quarters of data, while NoDetOL are ones with other recognized issues. Outlier categories are described in Table 1.
4. *Spectroscopic Data.* We adopted DR17 spectroscopic parameters when available, and DR16 if not; a table column indicates which data release is the source. A small number of stars lacked valid spectra and were labeled NoSpec. The central values for spectroscopic $T_{\rm eff}$, log$g$, [Fe/H], and [α/Fe] were taken directly from APOGEE. Their errors were inferred as described in the text. Values and errors for [C/Fe] and [N/Fe] were taken directly from APOGEE. Projected rotation velocities ($v \sin i$) were taken from R. A. Patton et al. (2024), and are listed only if they are detections above 5 km s^{-1}. Stars with high [α/Fe] at a fixed [Fe/H] are a distinct stellar population from Sunlike stars with lower [α/Fe]. We classify stars as α-rich or α-poor as described in Section 2.1.

Table 5
Catalog of Alternate Stellar Properties

Label	Contents
KIC	Number in the Kepler Input Catalog
Nquar	Number of quarters of Kepler data
ESA3, ESSe, ESSp	Adopted APOKASC-3, asteroseismic, and spectroscopic evolutionary states
Teff16, STeff16	DR16 $T_{\rm eff}$ and σ (K)
Logg16, Slogg16	DR16 spectroscopic log$g$ (cgs) and σ
FeH16, SFeH16, AlpFe16, SAlpFe16	DR16 [Fe/H] ([M/H]) and σ, [α/Fe] and σ
CFe16, SCFe16, NFe16, SNFe16	DR16 [C/Fe] and σ, [N/Fe] and σ
Teff17, STeff17	DR17 $T_{\rm eff}$ and σ (K)
Logg17, Slogg17	DR17 spectroscopic log$g$ (cgs) and σ
FeH17, SFeH17, AlpFe17, SAlpFe17	DR17 [Fe/H] ([M/H]) and σ, [α/Fe] and σ
CFe17, SCFe17, NFe17, SNFe17	DR17 [C/Fe] and σ, [N/Fe] and σ
PI, SPI	Gaia parallax π (mas) and σ
KS, SKS	2MASS K magnitude and σ
RG16, SRG16, RG17, SRG17	DR16 and DR17 MIST K-band $\frac{1}{R_{\rm Gaia}}$ and σ
RGGH, SRGGH	GHB09 $\frac{1}{R_{\rm Gaia}}$ and σ
FDnuSh, SFDnuSh, FnumaxSh	$f_{\Delta\nu}$ and σ, $f_{\nu{\rm max}}$, Sharma+White weighting
LoggSh, SloggSh	Seismic log$g$ (cgs) and σ, Sharma+White weighting, $f_{\nu{\rm max}}=1$
MSh, SMSh	Mass ($M_\odot$) and σ, Sharma+White weighting, corrected
RSh, SRSh	Radius ($R_\odot$) and σ, Sharma+White weighting, corrected
FDnuMo, SFDnuMo, FnumaxMo	$f_{\Delta\nu}$ and σ, $f_{\nu{\rm max}}$, GARSTEC+Mosser weighting
LoggMo, SloggMo	Seismic log$g$ (cgs) and σ, GARSTEC+Mosser weighting, $f_{\nu{\rm max}}=1$
MMo, SMMo	Mass ($M_\odot$) and σ, GARSTEC+Mosser weighting, corrected
RMo, SRMo	Radius ($R_\odot$) and σ, GARSTEC+Mosser weighting, corrected
FDnuWh, SFDnuWh, FnumaxWh	$f_{\Delta\nu}$ and σ, $f_{\nu{\rm max}}$, GARSTEC+White weighting
LoggWh, SloggWh	Seismic log$g$ (cgs) and σ, GARSTEC+White weighting, $f_{\nu{\rm max}}=1$
MWh, SMWh	Mass ($M_\odot$) and σ, GARSTEC+White weighting, corrected
RWh, SRWh	Radius ($R_\odot$) and σ, GARSTEC+White weighting, corrected
RGBAgeM, SRageMP, SRageMM	Garstec RGB age (Gyr) including mass loss and $\pm\ \sigma$
RCAgeM, SaageMP, SaageMM	Garstec RC/AGB age (Gyr) including mass loss and $\pm\ \sigma$
RGBAgeNoM, SRageNoMP, SRageNoMM	Garstec RGB age (Gyr) not including mass loss and $\pm\ \sigma$
RCAgeNoM, SaageNoMP, SaageNoMM	Garstec RC/AGB age (Gyr) not including mass loss and $\pm\ \sigma$
YRECAge	YREC model age (Gyr; see the text)
Fagecor, Mtrial	Age correction factor between trial and final mass, trial mass ($M_\odot$)
Fagemdrgb, Fagemdrc	Age correction factor for mass loss (η = 0.2) for RGB and RC stars.

Note. We include evolutionary states derived from asteroseismology as well as those derived from spectroscopy alone (0 = no state assigned,1 = RGB ,2 = RC, 3 = DW). For ESSE, −1 are cases where no state could be assigned, and −9999 is for stars not checked for states. Spectroscopic properties are from DR16 and DR17 are given, along with Gaia DR3 parallaxes and 2MASS photometry. We also present here asteroseismic data derived using all three combinations of models and weighting functions, including $f_{\Delta\nu}$, $f_{\nu{\rm max}}$, mass, radius, and asteroseismic surface gravity. Alternate age measurements with different models and assumptions about mass loss and Gaia radii inferred with different assumptions are also included. For details, see the text.

(This table is available in its entirety in machine-readable form in the online article.)

5. *Asteroseismic Parameters.* We used the weighted mean averages for $\Delta\nu$ and $\nu_{\rm max}$ for the Gold and Silver samples. Simple averages were used for detections. We adopted $f_{\Delta\nu}$ (Section 3.1) and $f_{\nu{\rm max}}$ (Section 3.2) values from the Garstec models with Mosser frequency-spacing weights discussed in Section 3.1.
6. *Global Stellar Properties.* Asteroseismic mass, radius, and log$g$[52] were taken from the Mosser $f_{\Delta\nu}$ scaling relation and the spectroscopic $T_{\rm eff}$. Ages were derived using the GARSTEC models. For lower RGB and RC stars, we provide ages inferred from models for the appropriate state only. For luminous giants, we distinguish between AGB, RGB, or AGB/RGB using spectroscopic criteria. Both AGB and RGB ages are provided for stars with ambiguous states. Gaia radii were inferred as described in the text.

We also present two additional tables. Table 5 includes alternative measurements of key properties. This includes DR16 spectroscopic data; $f_{\Delta\nu}$, $f_{\nu{\rm max}}$, mass, radius, and log$g$ values from the Sharma and White weighting schemes; ages from YREC; and Gaia radii derived using the P. González Hernández & P. Bonifacio (2009) version of the IRFM. Alternative weightings for the mean asteroseismic parameters themselves, and the raw measurements used for them, are presented in Appendices A and B.

We also make available on Zenodo (doi:10.5281/zenodo.13308665) an additional table that contains an extensive list of other key properties of interest, collated from other catalogs and sources. This includes a variety of photometric measurements, literature data from other large catalogs, and notes about special stars. Because this table is so

---

[52] Our asteroseismic gravities were derived without including the $f_{\nu{\rm max}}$ term, as discussed in Section 3.2.

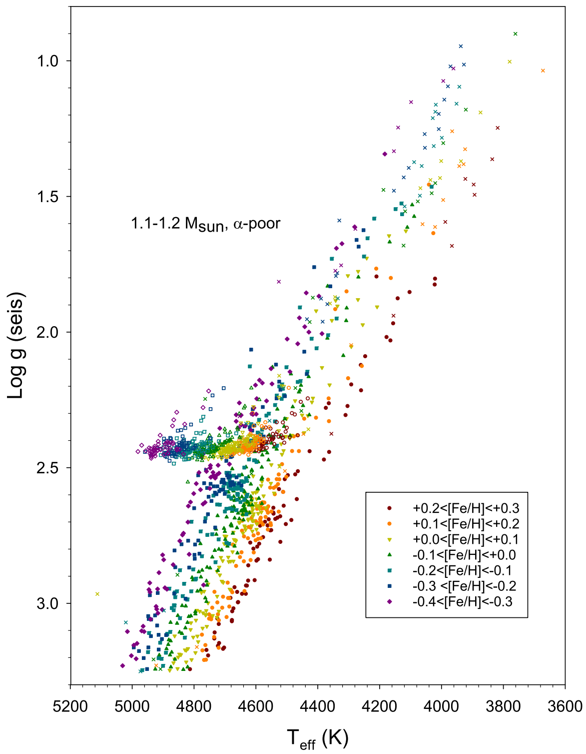

Figure 13. Stellar properties at fixed mass and variable metallicity. APOKASC-3 stars classified as α-poor, with masses between 1.1 and 1.2 $M_\odot$, shown in the asteroseismic log$g$–spectroscopic $T_{\rm eff}$ plane. Filled symbols are Gold sample RGB, open symbols are Gold sample RC, and crosses are Silver sample stars. Symbol types and colors reflect metallicity; stars shown are in the range $-0.5 < {\rm [Fe/H]} < +0.3$.

large, over 500 columns, and contains data from many sources, it is not as carefully vetted as the rest of the results that we present here. However, over the past decade, we have found it advantageous to have a precollated data set including magnitudes, spectroscopic parameters from various surveys, seismic results from our previous work and the literature, annotations about binaries and other stars of interest, and individual spectroscopic state indicators over time. We therefore make this previously internal and exploratory table accessible to everyone with this publication. We also refer to D. Godoy-Rivera et al. (2024) for a complementary characterization of the color–magnitude diagram and binary systems.

We now present key properties of our sample, starting with stellar physics and following up with stellar populations.

4.1. Stellar Physics

Stellar theory makes strong predictions about the properties of evolved red giant stars. Our asteroseismic sample permits stringent tests of stellar theory; in our view, it should be used as a standard calibration set for theoretical stellar interiors models. Here we present some examples of asteroseismology as a test of stellar physics.

4.1.1. Composition Trends

We begin by showing composition trends in a sample of stars with masses between 1.1 and 1.2 $M_\odot$ (Figure 13), restricting our data set to stars classified as α-poor. In this and the following figures, Gold sample shell-burning stars are shown with filled symbols; Gold sample core He-burning stars are shown with open ones, and the Silver sample is shown with crosses. The latter group consists predominantly of more luminous shell-burning stars. The position of the RGB and RC is strongly composition dependent, with a nearly constant $T_{\rm eff}$ offset between the two. The narrow width of the RC in log$g$ is also striking, and consistent with stellar theory. Double shell-burning, or AGB, stars are seen above the RC and are hotter than the main RGB, producing a broader upper RGB relative to the lower RGB. The RGBB is clearly seen below and to the right of the RC; this phenomenon occurs in theoretical models because there is a composition discontinuity associated with the lower boundary of the surface convection zone. When the H-burning shell at the top of the growing core reaches this boundary, the star temporarily becomes fainter and then brighter, producing about a factor of 3 local increase in the density of stars.

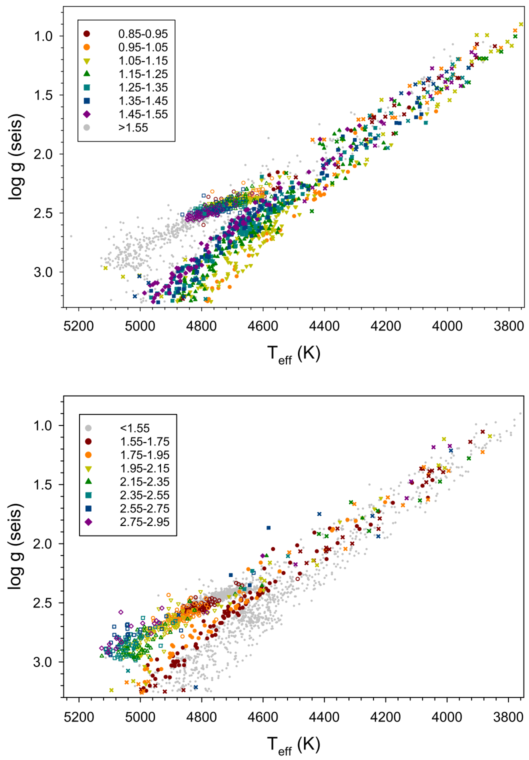

Figure 14. Stellar properties at fixed metallicity and variable mass. APOKASC-3 stars with $-0.05 < {\rm [Fe/H]} < +0.05$, shown in the asteroseismic log$g$–spectroscopic $T_{\rm eff}$ plane. Filled symbols are Gold sample RGB stars, open symbols are Gold sample RC stars, and crosses are Silver sample stars. Symbol types and colors reflect mass. The upper panel shows stars between 0.85 and 1.55 $M_\odot$, while the lower panel shows stars between 1.55 and 2.95 $M_\odot$. Higher-mass stars (upper panel) and lower-mass ones (lower panel) are shown in gray.

4.1.2. Mass Trends

We then isolate stars with close to solar metallicity ($-0.05 < {\rm [Fe/H]} < +0.05$), and show mass trends in Figure 14. Higher mass corresponds to hotter $T_{\rm eff}$, on average, but the effects are much smaller than those due to composition; furthermore, there is a strong relationship between surface gravity and mass in the RC. The latter is expected from theory, because low-mass RC stars have similar radii. The AGB/RGB contrast is more visible in this plane, where the strong dependence of the RGB locus on composition is absent; for example, the orange points in the upper panel are confined to

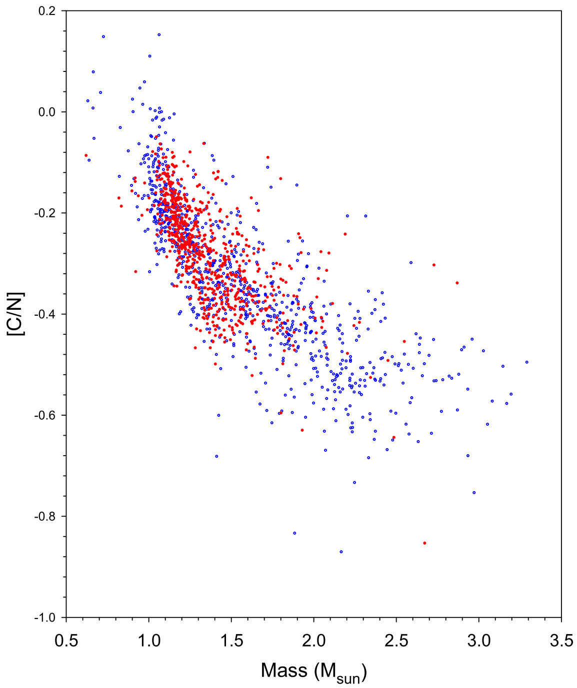

Figure 15. The first dredge-up at solar metallicity. APOKASC-3 stars classified as α-poor, with $-0.05 < [\mathrm{Fe/H}] < +0.05$, are shown in the [C/N]–mass plane. Red symbols are Gold sample RGB stars, and blue symbols are Gold sample RC stars. Higher-mass stars are preferentially seen in the RC due to lifetime effects.

the cool edge below the RC, but are observed at the hot and cool edges on the upper RGB. The mass dependence of the RGBB is also clearly seen here. At higher masses (lower panel), the RC population dominates, and on the lower RGB, massive stars are only seen on the hot edge.

4.1.3. The First Dredge-up

The development of a deep surface convection zone in giants also leads to a dredge-up of CN-processed material (see J. D. Roberts et al. 2024 for an empirical discussion in the APOKASC-3 context). The mass dependence of the first dredge-up at solar metallicity ($-0.05 < [\mathrm{Fe/H}] < +0.05$) is shown in Figure 15. The RC and RGB stars are similar, with some evidence of mass loss in the RC relative to the RGB in the lowest-mass stars.

4.1.4. The Red Clump

Reproducing the properties of the RC in detail is particularly challenging for stellar models. Core He-burning stars have convective cores, leading to significant uncertainties in the lifetime of the RC phase depending on the adopted model, especially the treatment of mixing at the outer boundary (D. Bossini et al. 2015; T. Constantino et al. 2015). G-mode period spacings (not discussed here) are difficult to reproduce with existing models, and they tend to favor longer lifetimes than those typically predicted by isochrones (J. Montalbán et al. 2013). Furthermore, the starting conditions (core mass as a function of initial mass and composition) are contingent on the prior evolution. Our sample provides an extraordinarily precise characterization of the RC. In Figure 16 we show some key properties of the RC. The bottom panel shows the location (in $\log g$ and T_{eff}) of three cohorts of α-poor stars (metallicity close to −0.3, 0 and +0.3, respectively). Metallicity induces significant T_{eff} offsets, while there are strong mass-dependent $\log g$ trends. The main (upper) portion of the RC shifts to lower $\log g$ for the most metal-rich stars. The lower boundary of the RC in mass–radius space is a distinctive feature clearly seen in earlier catalogs (M. H. Pinsonneault et al. 2018; J. Yu et al. 2018). However, in the APOKASC-3 sample (upper panel), we see a strikingly sharp lower boundary for the RC phase, shown here for the solar metallicity cohort. The drop in R close to $2\,M_{\odot}$ can be traced to the transition between degenerate and nondegenerate He ignition; the rise in R at higher masses can be traced to larger core masses in stars with higher birth mass.

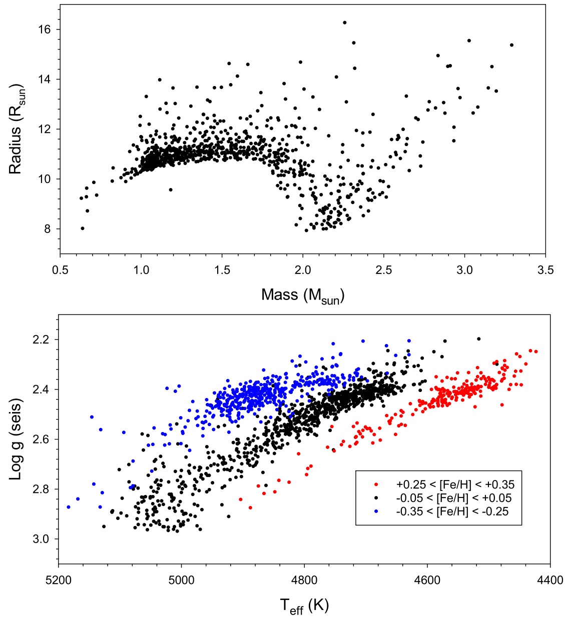

Figure 16. In the upper panels, we show the solar [Fe/H] sample in the mass–radius plane. The RC in the $\log g$–T_{eff} plane for three metallicity domains (−0.3, blue; 0, black; and +0.3, red; with a range of ±0.05 dex for each) is shown in the bottom panel. In all cases, we choose stars from the α-poor sample.

4.2. Stellar Populations

Galactic archeology, or the study of the formation history of the Milky Way, is a flourishing topic. Massive spectroscopic surveys, such as APOGEE and GALAH, have yielded detailed information on stellar abundances. Detailed kinematic, photometric, and distance information from the Gaia mission allows us to map out these trends across the Galaxy. Asteroseismology adds mass and age data for luminous evolved stars. The combination of all three is extremely powerful, and interesting insights have emerged from the Kepler fields (V. Silva Aguirre et al. 2018; A. Miglio et al. 2021; J. Montalbán et al. 2021; D. Huber et al. 2024). Here we highlight how our precise and accurate data allows us to see population features with high fidelity.

Before proceeding, it is important to acknowledge that there are significant selection effects in the Kepler data (M. H. Pinsonneault et al. 2014) that must be accounted for in detailed population studies. We therefore focus on clear global features, including sharp population boundaries and large trends, that are insensitive to details of the selection function.

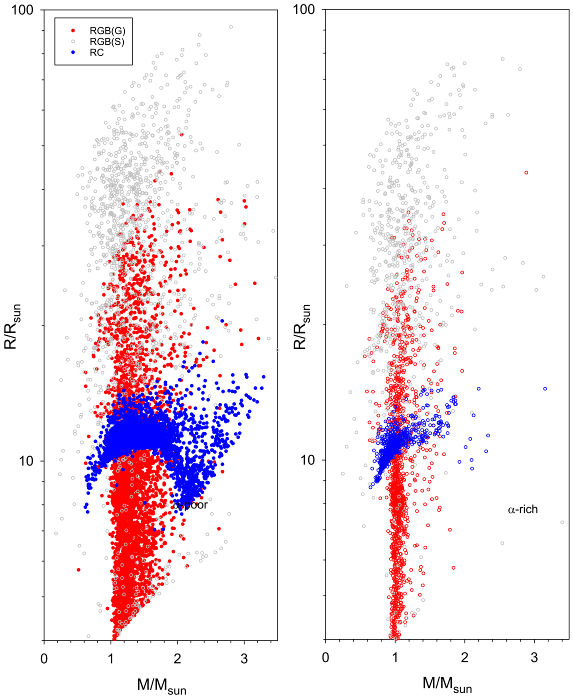

Figure 17. The RGB (red, filled) and RC (blue, open) in the mass–radius plane for α-poor stars (left) and α-rich stars (right). Silver sample stars are shown as gray circles. The field turnoff in the RGB below the clump, mass loss in the RC, and a mixture of AGB and RGB stars above the clump are clearly seen.

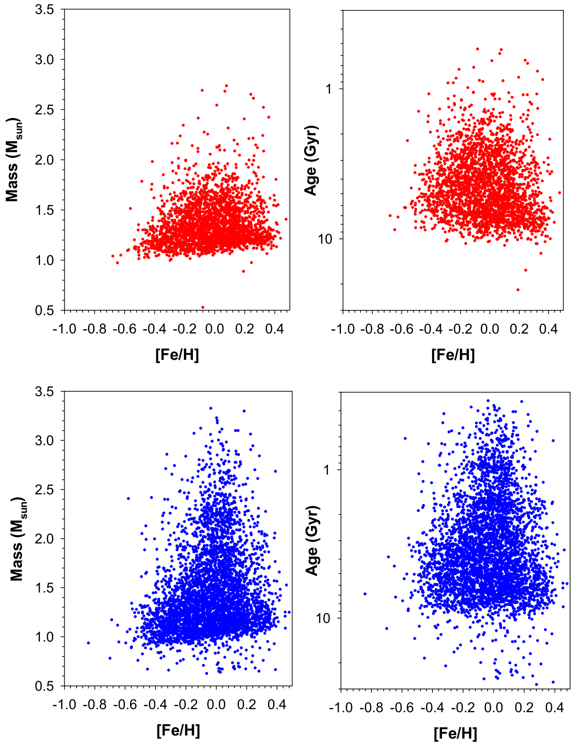

Figure 18. The α-poor RC (top) and lower RGB (bottom) in the mass–[Fe/H] plane (left panels) and the age–[Fe/H] plane (right panels). The RC spans a wider range of masses and ages, while both populations have a sharp lower age boundary corresponding to the finite age of the α-poor population. More-massive and younger stars are concentrated around solar metallicity.

Figure 17 shows mass versus radius for the α-rich (right panel) and α-poor (left panel) populations. The Gold RGB sample is in red, the RC is in blue, and Silver sample stars are in gray. Below the level of the RC, we can see a sharp lower boundary to mass in lower RGB stars. Lower-mass stars are seen in and above the RC, which is clear evidence for mass loss. Above the RC, we see both first-ascent RGB stars and second ascent AGB stars; the latter have experienced significant mass loss, which explains the presence of luminous stars below $1\,M_{\odot}$. The open gray symbols are Silver sample stars, which extend the sample to lower log$g$, albeit with larger mass uncertainties.

The lower RGB, below $10\,R_{\odot}$, therefore allows us to see the RGB population prior to the onset of significant mass loss. In the figures that follow, we therefore compare RC and lower RGB stars in the α-poor and -rich populations.

From Figure 17, the α-poor population has a wide range of masses, and by extension ages. Figure 18 shows the mass and age distributions of the α-poor population. A number of features deserve comment. Higher-mass RGB stars are much less common than higher-mass RC stars because higher-mass stars have much longer RC lifetimes relative to their RGB lifetimes; the RC therefore probes a younger population, on average, than the RGB (see Figure 14). There is a well-defined upper edge in age for both the RC and RGB. The close correspondence in age for the two groups is a confirmation of our mass-loss model for the RC, as we would have obtained a significant age offset between the two populations if our assumptions about mass loss in the RC were very wrong. This is easier to quantify with the α-rich population, which we do below. There is a small but real subpopulation of very-low-mass stars in the RC that are not seen in the RGB. Although we report high formal ages for these stars, their low masses are the products of severe mass loss, likely from interactions with a companion (Y. Li et al. 2022). They appear in the RC because the majority of stellar interactions on the RGB occur on the upper RGB.

There are observational selection effects disfavoring the detection of metal-poor and lower-mass stars in the RC that appear as blue horizontal-branch stars; such objects are too hot to excite solar-like oscillations, explaining their absence in the RC population. See L. Molnár et al. (2024) for a recent discussion. There is no comparable selection against very-low-mass or low-metallicity stars on the lower RGB, so their absence is a true population feature for the Kepler fields. Such stars are seen in APO-K2 (J. Schonhut-Stasik et al. 2024), illustrating the importance of sampling a range of Galactic stellar populations.

Finally, a wide range of masses at fixed [Fe/H] are seen in the α-poor RC, but high-mass (and, typically, young) stars are much more likely to be seen at solar metallicity than for lower or higher metal content. This is not merely a function of there being more solar metallicity stars; there is a much larger fraction of high-mass stars at solar metallicity than at lower or higher values. Our finding that the youngest stars have solar metallicity agrees with other studies in the solar circle (L. Casagrande et al. 2011; D. K. Feuillet et al. 2018), but with higher age precision.

This can be explained if stars born in the solar neighborhood are close to solar in metallicity, while more metal-rich and metal-poor star stars currently being born in the Galaxy are found closer and farther from the Galactic center, respectively. Stars migrate radially in the Galactic disk, blurring the age–metallicity distribution locally. However, there is a time lag for

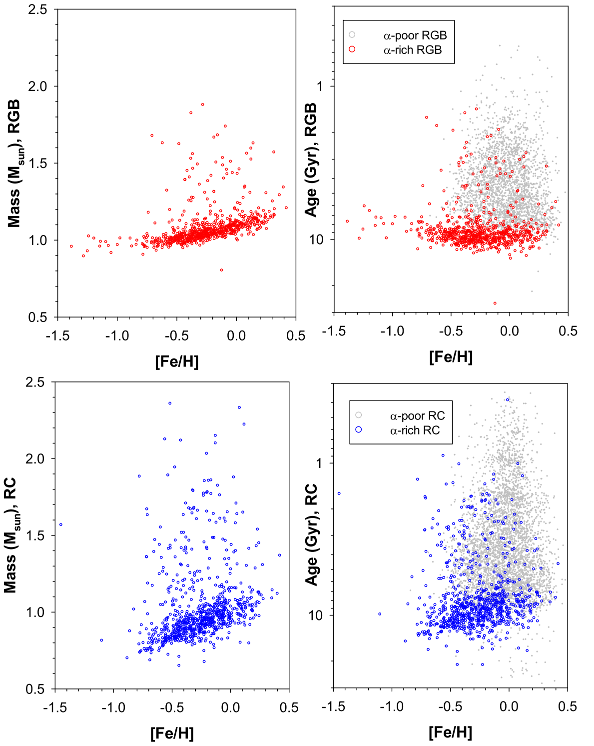

Figure 19. The α-rich populations in the mass–[Fe/H] (left) and age–[Fe/H] (right) planes for the RGB (top) and RC (bottom). The α-poor populations in age space are shown for comparison as faint gray points in the right panels; a clear division, corresponding to the difference between the thick and thin disks, is seen. The RGB masses are also shown in the lower-left panel, and the difference between them and the RC is clear evidence for mass loss.

this process, resulting in a preference for young near-solar metallicity stars (D. K. Feuillet et al. 2018; Y. Lu et al. 2022).

The α-rich population has a distinct mass and age distribution, and it is associated with the thick disk. There is a well-defined peak in the mass and age distributions. In previous studies (A. Miglio et al. 2021), this was found to correspond to a characteristic age of 11 Gyr. Figure 19 shows the masses (left) and ages (right) of lower RGB (top) and RC (bottom) stars. There is a clear distinction between the ages of the α-poor (top right, gray symbols) and the α-rich stars. There is a subpopulation of massive, and potentially young, α-rich stars. As this can impact mean statistics, for the exercises that follow, we use median statistics and the MAD converted to an effective σ. Using this approach, the median ages of the RGB and RC stars are 9.14 ± 0.05 Gyr and 9.28 ± 0.08 Gyr, respectively. The close correspondence between the two is a validation of our mass-loss model for the RC, where we required that the median birth mass in the RC be equal to the median lower RGB mass in the α-rich sample. After rejecting 5σ age outliers, the median RGB and RC masses are, respectively, 1.03 and 0.93 $M_\odot$, for an implied median mass loss of 0.1 $M_\odot$. Reconciling the ages of the two populations would require a slight reduction, of the order of 0.004 $M_\odot$, in the model mass-loss rates or a corresponding change in the relative RC and RGB masses, well within our uncertainties in the relative masses and radii of the two populations.

After performing a 5σ outlier rejection, we can use the width of the main age peak as a diagnostic of the uncertainties (Figure 20). The age dispersion in the bulk population of the lower RGB, 1.1 Gyr, is slightly below the 1.3 Gyr dispersion predicted by our error model—indicating that the random mass uncertainties are below 4% for this sample, and that the underlying age dispersion is <1.1 Gyr. The RC age distribution is clearly broader, with an age $\sigma = 2.12$ Gyr. This is consistent with a dispersion in mass loss at fixed birth mass of 0.03 $M_\odot$, comparable to results seen in modeling of the horizontal branch in globular cluster stars. There is some tendency for stars below [Fe/H] $= -1$ to drift to younger ages, reflecting known problems for halo star ages from asteroseismology (C. R. Epstein et al. 2014; J. Schonhut-Stasik et al. 2024).

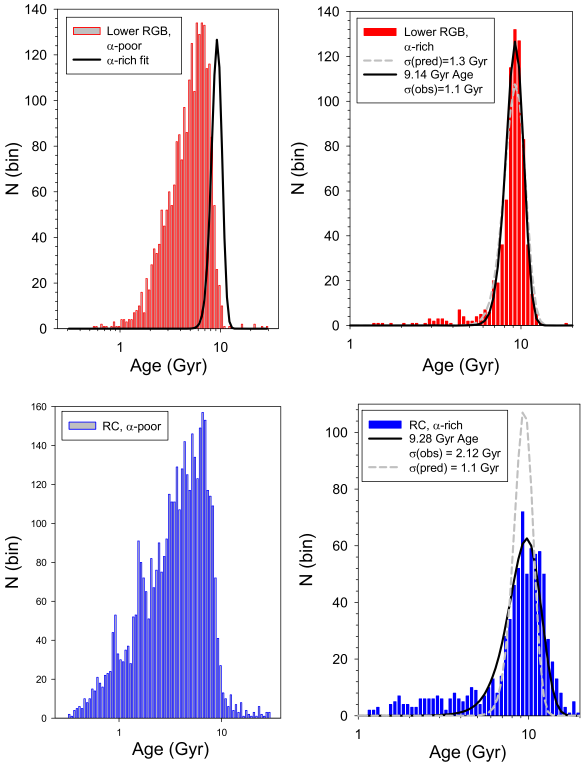

Figure 20. Age distributions for different evolutionary states and chemical populations. The α-rich populations (right) show a strong age peak, while the α-poor ones are broader. The lower RGB (top) and RC (bottom) have similar high age cutoffs, but young stars are much more common in the RC. For the α-rich populations, the peak age and observed dispersion is overlaid for comparison (solid line); the predicted distribution is shown with a short dashed line. For the α-rich populations, the lines indicate the location of an edge in the age distribution (at 7.3 Gyr for the RGB and 6 Gyr for the RC) with the observed dispersions as derived in the right panels.

The upper RGB is complicated by the observed mixture of RGB and AGB stars. The overall data quality is also lower, with a much larger fraction of Silver sample versus Gold sample stars. However, the age distribution of these stars is an interesting astrophysical and modeling test (Figure 21). There is still a clear concentration of the Gold sample stars at an older age of 7.88 ± 0.12 Gyr; Silver sample stars have large age uncertainties and a lower mean age of 6.85 ± 0.08 Gyr. The primary difference between the two is that the Silver sample stars have a lower mean log$g$. If interpreted as a systematic age error, the Gold and Silver samples would be offset by 17% and 35%, respectively.

5. Discussion and Conclusions

Our goal in this paper was twofold: to develop a complete asteroseismic catalog of Kepler giants with spectroscopy, and to critically evaluate the strengths and limitations of asteroseismic scaling relations. Out of the 15,808 stars that we

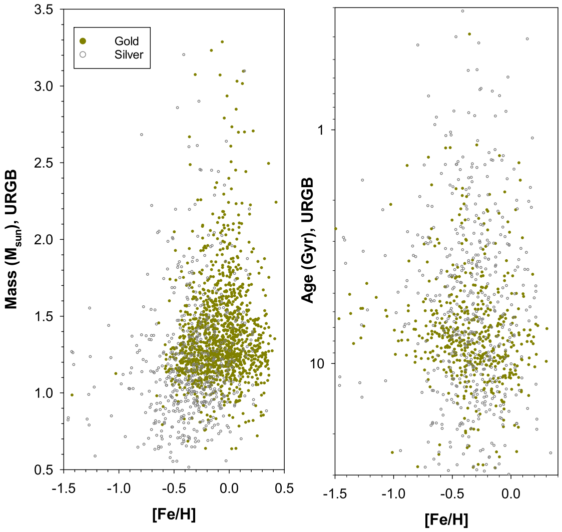

Figure 21. Upper RGB stars in the α-rich population in the mass–[Fe/H] plane (left) and the age–[Fe/H] plane (right). Silver sample stars are dark gray symbols, and Gold sample ones are red symbols. A small number of points below 0.5 and above 3.5 $M_\odot$ are not shown. The Silver sample includes a larger number of stars at lower metallicity, with higher scatter.

studied, we report 12,448 asteroseismic masses, radii, and ages. This yield may seem surprisingly small, given that solar-like oscillations are nearly universal in cool giants. A tour through our filters, however, provides a straightforward explanation. A total of 1356 stars are real detections, but in domains where we cannot provide valid solutions: background sources (129), stars without good spectroscopic solutions (174), oscillation frequencies that are too close to the Nyquist sampling rate (567), or stars too low for scaling relations to be valid (486). This still leaves 2004 stars as marginal detections or nondetections. The failure modes here are varied, but fall into a few general families. Some targets had predicted oscillation frequencies close to the Nyquist sampling rate, and may not have detectable signals with 30 minutes sampling. Many targets had short time series. The Kepler mission did not consistently observe evolved giants, particularly luminous ones, and long time series data is required to detect low oscillation frequencies. Other light curves had artifacts or highly variable background sources that confounded automated algorithms. Finally, there was an interesting minority of targets that had true astrophysical backgrounds, such as stellar activity, eclipses, or double oscillation patterns. These stars are interesting, and we have summarized their key properties in the relevant tables.

Our Gold sample of 10,036 stars is the most precise and accurate asteroseismic data set to date, making it an excellent training set for inferring ages in other surveys. The Silver sample of 2382 stars extends the data to lower surface gravity. Our data is also a powerful test for stellar interiors models, and should be used as a reference in isochrones. Traditionally, stellar models are calibrated on the Sun, but it is now possible to directly compare absolute model properties of evolved stars with asteroseismic data. The core He-burning locus, the location of the RGB, and that of the RGBB as a function of mass and composition are testable fundamental predictions of stellar interiors models, along with the first dredge-up. The field star data here complements globular cluster data, which extends to lower metallicities than those in our sample. Our data covers a much wider range of masses and metallicities than the well-studied open cluster sample, and the field star sample of evolved stars is also much larger. Population inferences are more complex to interpret, but the sharp cutoffs in the mass distributions for thin and thick disk stars are robust, and point to stringent bounds on their formation ages. The narrow age range in the thick disk population is also a robust feature. The strong metallicity dependence of the mass distribution, similarly, will set interesting constraints on radial-mixing models.

Our approach—using multiple analysis techniques—was explicitly designed to stress test the scaling relations. Different methods had excellent internal agreement for low-luminosity giants. Above $\sim 20 R_\odot$, larger *measurement* systematics started to arise. We saw similar effects in the mapping of $\Delta\nu$ to $\langle\rho\rangle$ from theoretical models. The RC was more complex; in that case, there appear to be method-dependent systematics relative to the RGB at the 1% level across the board. We then did an external comparison with Gaia radii. The agreement at low radii was again excellent (at the 1%–2% fractional level in R). For the largest radii, we saw significant trends and large (up to 50%) fractional offsets.

Putting this together, scaling relationships are remarkably precise and accurate on the lower RGB and the RC. There are some potential systematic error sources between the two phases that are important to account for, in particular for inferring mass loss during the RGB phase. Systematics between the RGB and RC could enter in at the 1%, 3%, and 10% levels in radius, mass, and age, respectively. Scaling relations remain useful for more luminous stars but require careful calibration and attention to measurement systematics. For the most luminous stars, with $\nu_{\rm max}$ below 1 μHz, we do not recommend the usage of scaling relations to infer masses and radii. This is partially driven by empirical data showing large offsets, and partially driven by theoretical work mapping out the breakdown in the underlying assumptions. Asteroseismology remains an interesting tool for luminous giants, but we believe that it calls for different analysis tools, such as a move to modeling of individual frequencies, and a more rigorous assessment of measurement techniques (e.g., M. Joyce et al. 2024).

In terms of best practice, we have three key recommendations. First, we recommend using more than one detection method to validate results from automated pipelines. This is valuable for outlier rejection and for a good understanding of recovery rates. Second, theoretical stellar models are essential for interpreting the observed frequency spacings, impacting stellar parameter estimates significantly. Such models can account for nonuniform mode spacing, allowing scaling relation studies to incorporate some individual frequency properties in a compact fashion. Finally, we recommend calibration of the results against fundamental data. Even in the well-studied Kepler fields, with excellent data, we demonstrated that significant systematics can be injected into global stellar parameters that make outcomes dependent on evolutionary state and luminosity.

Our masses and radii are tied to an absolute system, and we believe that they are precise and accurate within the quoted random and systematic uncertainties. We have provided individual measurements in case users prefer to adopt single pipeline measurements; in such cases, we encourage users to check the outcomes against the fundamental calibration set, which we provide.

The global APOGEE $T_{\rm eff}$ scale is tied to the IRFM, and for solar-type stars, there are stringent limits on deviations (J. C. Zinn et al. 2019b). As discussed in the APO-K2 catalog (J. Schonhut-Stasik et al. 2024), however, there may be $T_{\rm eff}$ offsets in the metal-poor domain that could translate into mass systematics. There is some evidence for such trends in our metal-poor data. We encourage a revised look at the IRFM temperature scale in the metal-poor domain.

Age estimates are more complex than mass or radii estimates, with clear model-dependent offsets, particularly for younger stars with convective cores on the main sequence. The RC ages also depend on the assumed mass loss in prior phases, and ages also assume a specific mapping between helium abundance and metal content. However, we see encouraging signs in our data. The maximum ages of the α-rich and α-poor populations are consistent between the RC and RGB, validating our mass-loss model. On the lower RGB, we also see no evidence of mass or age trends with log$g$. Conversely, there is some evidence for differences in mean age for α-rich luminous stars relative to the lower RGB and RC, indicating that our radius calibration did not completely remove age systematics for such stars.

In addition to Kepler, K2 is a valuable asteroseismic resource (J. Schonhut-Stasik et al. 2024). Although the data precision is lower than that of Kepler, the K2 mission sampled a more diverse set of stellar populations, particularly for more metal-poor stars. TESS and the upcoming Roman mission represent exciting opportunities for asteroseismology of stellar populations. TESS will provide a large sample of bright, primarily local, stars (M. Hon et al. 2021), concentrated in the domain where scaling relations work well (the lower RGB and RC). The Roman Galactic Bulge Time Domain Survey will be a deep census of stars in the Galactic bulge, sampling very different stellar populations than Kepler (D. Huber et al. 2023).

Acknowledgments

We thank the anonymous referee for providing constructive comments that improved the paper. This paper includes data collected by the Kepler mission and obtained from the MAST data archive at the Space Telescope Science Institute (STScI). Funding for the Kepler mission is provided by the NASA Science Mission Directorate. STScI is operated by the Association of Universities for Research in Astronomy, Inc., under NASA contract NAS 5-26555. M.H.P. acknowledges support from NASA grants 80NSSC24K0637 and 80NSSC18K1582. M.H.P., J.T., and P.M.F. acknowledge that part of this work was performed at the Aspen Center for Physics, which is supported by National Science Foundation grant PHY-1607611. M.H.P. acknowledges support from the Fundación Occident and the Instituto de Astrofísica de Canarias under the Visiting Researcher Programme 2022-2025 agreed between both institutions. A.S. acknowledges support by the Spanish Ministry of Science, Innovation and Universities through the grant PID2023-149918NB-I00 and the program Unidad de Excelencia Marìa de Maeztu CEX2020-001058-M, and by Generalitat de Catalunya through grant 2021-SGR-1526. S.B. acknowledges NSF grant AST-2205026. P.G.B. acknowledges support by the Spanish Ministry of Science and Innovation with the *Ramón y Cajal* fellowship Nos. RYC-2021-033137-I and MRR4032204. D.S. is supported by the Australian Research Council (DP190100666). P.G.B., D.G.R., and R.A.G. acknowledge support from the Spanish Ministry of Science and Innovation from grant No. PID2023-146453NB-100 (*PLAtoSOnG*). M.V. acknowledges support from NASA grant 80NSSC18K1582 and funding from the European Research Council (ERC) under the European Union's Horizon 2020 research and innovation program (grant agreement No. 101019653). T.C.B. acknowledges partial support for this work from grant PHY 14-30152; Physics Frontier Center/JINA Center for the Evolution of the Elements (JINA-CEE), and OISE-1927130: The International Research Network for Nuclear Astrophysics (IReNA), awarded by the US National Science Foundation. The research leading to the presented results has received funding from the ERC Consolidator Grant DipolarSound (grant agreement No. 101000296). P.F. and T.S. acknowledges support from the National Science Foundation Astronomy and Astrophysics grants AST-1715662 and AST-2206541. S.M. acknowledges support by the Spanish Ministry of Science and Innovation with the Ramon y Cajal fellowship Nos. RYC-2015-17697, PID2019-107061GB-C66, and PID2023-149439NB-C41, and through AEI under the Severo Ochoa Centres of Excellence Programme 2020–2023 (CEX2019-000920-S). S.M. and D.G. R. acknowledge support from the Spanish Ministry of Science and Innovation (MICINN) from grant No. PID2019-107187GB-I00. D.G.R. acknowledges support from the Spanish Ministry of Science and Innovation (MICINN) with the Juan de la Cierva program under contract JDC2022-049054-I. L.B. gratefully acknowledges support from the European Research Council (ERC) under the Horizon Europe program (Calcifer; Starting grant agreement No. 101165631). A.R.G.S. acknowledges the support from the FCT through national funds and FEDER through COMPETE2020 (UIDB/04434/2020, UIDP/04434/2020, and 2022.03993.PTDC) and the support from the FCT through work contract No. 2020.02480.CEECIND/CP1631/CT0001.

Funding for the Sloan Digital Sky Survey IV has been provided by the Alfred P. Sloan Foundation, the U.S. Department of Energy Office of Science, and the Participating Institutions. SDSS acknowledges support and resources from the Center for High-Performance Computing at the University of Utah. The SDSS website is www.sdss4.org.

SDSS is managed by the Astrophysical Research Consortium for the Participating Institutions of the SDSS Collaboration including the Brazilian Participation Group, the Carnegie Institution for Science, Carnegie Mellon University, Center for Astrophysics—Harvard & Smithsonian (CfA), the Chilean Participation Group, the French Participation Group, Instituto de Astrofísica de Canarias, The Johns Hopkins University, Kavli Institute for the Physics and Mathematics of the Universe (IPMU)/University of Tokyo, the Korean Participation Group, Lawrence Berkeley National Laboratory, Leibniz Institut für Astrophysik Potsdam (AIP), Max-Planck-Institut für Astronomie (MPIA Heidelberg), Max-Planck-Institut für Astrophysik (MPA Garching), Max-Planck-Institut für Extraterrestrische Physik (MPE), National Astronomical Observatories of China, New Mexico State University, New York University, University of Notre Dame, Observatório Nacional/MCTI, The Ohio State University, Pennsylvania State University, Shanghai Astronomical Observatory, United Kingdom Participation Group, Universidad Nacional Autónoma de México, University of Arizona, University of Colorado Boulder, University of Oxford, University of Portsmouth, University of Utah, University of Virginia, University of

Washington, University of Wisconsin, Vanderbilt University, and Yale University.

Appendix A
Asteroseismic Pipelines and Light-curve Preparation

We employed a total of 10 distinct codes for inferring asteroseismic properties of the sample. Seven of these, which we designate as core methods, were designed to measure both $\Delta\nu$ and $\nu_{\max}$. Three were used to measure $\nu_{\max}$ only. Not all methods were used on all stars; only a subset of methods were used to study the more luminous cohort of targets. Here, we describe how the light curves were prepared, and provide detailed descriptions of the individual methods used to infer asteroseismic properties. In Appendix B, we describe how the results were combined into single values with uncertainties.

A.1. Light-curve Preparation

In our study, we utilize KEPSEISMIC[54] Kepler data from the Mikulski Archive for Space Telescopes (MAST). These light curves undergo corrections using the Kepler Asteroseismic data analysis and calibration Software (KADACS; R. A. Garcìa et al. 2011). The corrections involve removing outliers, addressing jumps and drifts, and stitching together data from all quarters. Additionally, to mitigate the impact of regular gaps primarily caused by instrumental operations, such as angular momentum dumps and monthly downlink Earth pointings, we employ a multiscale discrete cosine transform to interpolate missing data (J.-L. Starck & F. Murtagh 2006; R. A. Garcìa et al. 2014; S. Pires et al. 2015), following inpainting techniques based on a sparsity prior (M. Elad et al. 2005).

Subsequently, the light curves are filtered using a 20 or 80 day high-pass filter to eliminate long drifts resulting from the Kepler orbit. The combination of two or more high-pass filtered light curves is a common way to study low-frequency stellar signals in the Kepler data. For example, it has been successfully applied to measure stellar rotation (e.g., T. Ceillier et al. 2017; A. R. G. Santos et al. 2019; S. N. Breton et al. 2021; R. A. Garcìa et al. 2023). The 20 day filter makes it difficult to extract asteroseismic signals in luminous giants with low oscillation frequencies. We therefore use the 80 day filter for stars with $\nu_{\max} < 10\ \mu$Hz; this threshold was chosen because signal recovery with the 20 day filter degraded drastically for lower $\nu_{\max}$. However, the 80 day filter is noisier, injecting scatter into measurements at high $\nu_{\max}$, so we adopted the 20 day filter for stars with $\nu_{\max}$ above 10 μHz.

A.2. Core Asteroseismic Pipelines

The core asteroseismic pipelines are designed to infer both $\Delta\nu$ and $\nu_{\max}$. Many methods detect a power excess above a background to infer $\nu_{\max}$ (see Figure 22), typically by smoothing, or fitting bell-shaped functions to, the discrete frequency spectrum. The discrete oscillation frequencies are then used to characterize $\Delta\nu$, which is defined as the mean separation between modes of different radial order n but the same spherical degree l. Even and odd l modes cluster together in a power spectrum; in most cases, $l = 0$, 1, and 2 can be detected, so the even ($l = 0$, 2) and odd ($l = 1$) modes can be distinguished by searching for a pattern that has close doublets alternating with single modes. The $l = 1$ (and, to a lesser degree, $l = 2$) mode frequencies can be mixed in character—strongly influenced by core g-modes—which can induce a large deviation from uniform spacing. These modes can also be split by rotation.

The observed mode spacing also varies with frequency; some methods focus on modes close to $\nu_{\max}$ while others average results across a wider range. In practice, there can be confounding features, such as pollution of the light curves by other stellar variables in the same apertures. Six of the methods that we use here were included in APOKASC-2, although the pipelines themselves have been modified in the intervening time. We now describe the individual pipelines.

A.2.1. COR

The COR seismic parameters are derived from the envelope autocorrelation function (EACF), as described in B. Mosser & T. Appourchaux (2009). The method uses the properties that the square of the autocorrelation of the time series can be calculated as the Fourier spectrum of the filtered Fourier spectrum, as initially shown by I. W. Roxburgh & S. V. Vorontsov (2006). It first measures the large separation $\Delta\nu$ in a fully blind manner. The reliability of the detection is given by the H_0 test. Then, the frequency $\nu_{\max}$ is inferred from the identification of the oscillation excess power, assuming that the local stellar background around $\nu_{\max}$ can be approximated by a power law in frequency. The estimate of $\Delta\nu$ can be refined, using the homologous properties of the red giant oscillation pattern, as depicted by the so-called universal red giant oscillation pattern (B. Mosser et al. 2011b). The COR pipeline was run on the full set of data, including luminous giants.

A.2.2. ELS

The ELS seismic parameters are derived using the methods described in Y. Elsworth et al. (2020). A key feature is the use of a layered approach, which applies many loose constraints to remove false detections. This has the advantage of a high detection rate combined with a low number of false positives. The frequency $\nu_{\max}$ is determined from an Markov Chain Monte Carlo fit to the power spectrum with the background represented by two Harvey-like profiles, a constant white noise component and the mode power by a Gaussian function centered on $\nu_{\max}$. The effect of the integration time on the shape of the power spectrum is included. For $\Delta\nu$, the method looks for the mode regularity by employing the power spectrum of the power spectrum in the region where the modes are most prominent. A small adjustment is applied to correct for the correlation between $\Delta\nu$ and $\nu_{\max}$.

A.2.3. SYD

The SYD results were derived using the SYD pipeline (D. Huber et al. 2009), largely following the approach as in previous APOKASC data releases. Here we summarize the differences. We adopted the SYD results from the catalog of 16,000 red giants by J. Yu et al. (2018) for stars overlapping with our list. For the rest, we ran the SYD pipeline using $\nu_{\max}$ values from M. Hon et al. (2018) and M. Hon et al. (2019) as initial guesses. The results were vetted using the automated deep learning method by C. Reyes et al. (2022).

---

[54] https://archive.stsci.edu/prepds/kepseismic/

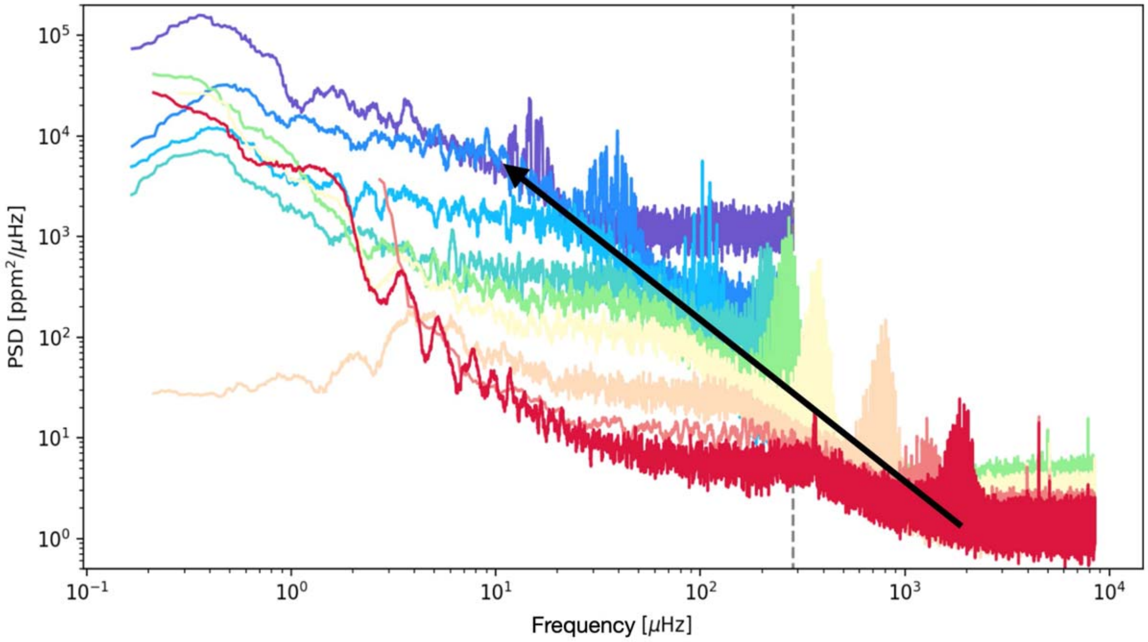

Figure 22. Power spectral density of solar-like oscillators observed by Kepler from the main sequence (red) to evolved red giant branch stars (purple). The vertical dashed gray line indicates the Nyquist frequency for Kepler long-cadence observations. The arrow indicates the decrease in frequency and the increase in power density associated with stellar evolution up until the tip of the RGB.

A.2.4. CAN

The CAN pipeline was one of the five used in the APOKASC-2 paper, and was described there and in T. Kallinger et al. (2010). The majority of the results here are taken from APOKASC-2. New calculations were performed for some luminous giants not present in the original APOKASC-2 effort.

A.2.5. DIA

This method relies on the adoption of the Bayesian inference code DIAMONDS (E. Corsaro & J. De Ridder 2014), which has been developed with the main purpose of analyzing asteroseismic data. The method is directly applied to the stellar power spectral density (PSD), which in this case has been obtained through the KADACS pipeline suite for asteroseismic-optimized data sets (R. A. Garcìa et al. 2011, 2014; S. Pires et al. 2015) starting from the raw Kepler light curves. As presented by E. Corsaro et al. (2017), the PSD is first analyzed by fitting the background model introduced by T. Kallinger et al. (2014). The background model comprises a Gaussian function to reproduce the typical power excess of solar-like oscillations, a flat instrumental noise component, and a series of Harvey-like profiles (J. Harvey 1985) accounting for the effects of stellar granulation, instrumental variations, and potential magnetic activity. The number of Harvey-like components is decided based on an assessment of the Bayesian evidence estimated by DIAMONDS, which is used to evaluate a statistical weight on the fitting model, such that the model providing the best balance between complexity (i.e., number of free parameters) and quality of the fit, is favored. The fitting of the Gaussian envelope of the background model finally provides the estimate of $\nu_{\max}$, along with its Bayesian credible intervals as a measure of uncertainty in the parameter.

For obtaining an estimate of $\Delta\nu$, the method evaluates a squared autocorrelation function (ACF^2) over the region of stellar PSD that contains the oscillation envelope. Before the ACF^2 is applied, the PSD is smoothed with a boxcar having width $\Delta\nu/10$, where the guess for $\Delta\nu$ is taken from a scaling relation (D. Huber et al. 2011). The smoothing has the effect of reducing the stochasticity that is typical of this type of data, resulting in a net improvement of the ACF^2 signal when originating from the presence of a comb-like structure that is characteristic of the solar-like oscillations. The search range of the ACF^2 method is also based on the $\Delta\nu$ guess obtained from the scaling relation, and typically ranges within ±30% of this value. The final estimate of $\Delta\nu$ and its 1σ uncertainty are obtained from the centroid of a Gaussian function fitting the ACF^2 around its maximum. The fitting is performed by means of a nonlinear least-squares fitting method. This pipeline was run on a minority of the stars in the sample, but did include some luminous giants.

A.2.6. GAU

The GAU algorithm was designed to estimate $\nu_{\max}$, $\Delta\nu$, and $A_{\max}$, the amplitude of the Gaussian function employed to model the oscillations' power excess. First, it reads the power spectrum of the time series, and computes the envelope of the filtered autocorrelation of the time series in the way proposed by I. W. Roxburgh (2009) and B. Mosser & T. Appourchaux (2009). In practice, it consists of computing the power spectrum of the power spectrum multiplied by a smooth bandpass filter of 20 μHz width that is centered on a grid of frequencies that run from 1 μHz to the Nyquist frequency (283 μHz) every 5 μHz. If there is a significant maximum in the envelope of the autocorrelation, its location provides both $\Delta\nu$ and an initial proxy of $\nu_{\max}$. Second, the code checks whether it picked a harmonic of $\Delta\nu$ based on the relation between $\Delta\nu$ and $\nu_{\max}$ from D. Stello et al. (2009) $\Delta\nu = \Delta\nu_{\odot}(\nu_{\max}/\nu_{\max,\odot})^{0.75}$. Third, it performs a background fitting of the power spectrum by including two Harvey functions for the stellar activity, a white noise level, and a Gaussian function for the oscillations. The best-fitting algorithm is a maximum likelihood estimator with Bayesian prior as initially described in P. Gaulme et al. (2009). The oscillation $\nu_{\rm max}$ and $A_{\rm max}$ are the central frequency and height of the Gaussian function. The error bars are computed from the Hessian of the likelihood estimator. The GAU pipeline was run only using the 20 days filtered data, so it was not used for stars with $\nu_{\rm max}$ below 10 μHz.

A.2.7. A2Z

The A2Z+ pipeline is a combination of the A2Z (S. Mathur et al. 2010) and an implementation of the EACF method. With the A2Z method, the mean large frequency separation $\Delta\nu$ is inferred by computing the power spectrum of the power spectrum in a region of the power spectrum density where the most prominent repetition of peaks is found, above a given confidence level of 90%. The convective background is then modeled with four different components: two Harvey functions (J. Harvey 1985) to model different scales of granulation with a fixed slope of 4, a Gaussian function to model the p-mode envelope, and a white noise term. The frequency of maximum power is obtained from the fit of the Gaussian that is centered at $\nu_{\rm max}$. In addition, a complementary determination of $\Delta\nu$ and $\nu_{\rm max}$ is included in A2Z+ following the EACF method by B. Mosser & T. Appourchaux (2009). We then compare the results between the two methods. Stars where the values agree within 10% are treated as firm detections, while the others are flagged and visually inspected. Finally, we implemented a refinement of $\Delta\nu$ by cross-correlating the power spectrum with a template with modes $l = 0$ and 2 varying $\Delta\nu$ and the small frequency separation (S. Mathur et al. 2016, 2022) to pick the $\Delta\nu$ with the highest cross-correlation value.

A.3. Other Methods

It is valuable to detect an asteroseismic signal even in cases where the detailed frequency pattern cannot be characterized. The three methods in this section were not used to infer frequency spacings, but are very useful for detecting $\nu_{\rm max}$, particularly in sparse or noisy data sets. Some methods rely on machine learning approaches, while others use other information (such as the granulation spectrum) to improve measurement precision.

A.3.1. HON

This method utilizes deep learning to detect the presence of a power excess corresponding to solar-like oscillations within power spectra. As described in M. Hon et al. (2018), power spectra represented in logarithmic axes are converted into a binary 128 × 128 images as inputs into two convolutional neural networks. The first network classifies power spectra into those containing solar-like oscillations and those without, while the second network measures $\nu_{\rm max}$ by identifying the region of the input image that contains the oscillations. The networks are trained with supervised learning using a labeled training set. For the classification of stars across the full Kepler sample, the networks are trained using the J. Yu et al. (2018) catalog as a training set, as described in M. Hon et al. (2019).

A.3.2. CV

The "coefficient of variation" (CV) method for detecting solar-like oscillations and reporting $\nu_{\rm max}$ values is described in K. J. Bell et al. (2019). The power spectrum is split into frequency bins with widths that scale approximately with the expected $\Delta\nu$ if $\nu_{\rm max}$ were centered in each bin. Within each bin, the CV metric is computed as simply the ratio of the standard deviation of the periodogram power to the mean power in the bin. These bins are narrower than the frequency scale of granulation, such that this background is essentially flat across each bin. If a bin contains no signal besides the granulation background, the CV value is expected to be near 1.0 for random noise distributed about the background as χ^2 with two degrees of freedom. Candidate solar-like oscillations are identified as statistically significant excesses in CV that have widths and heights consistent with known examples of solar-like oscillating red giants. The CV method is able to effectively separate the solar-like oscillation signals from the granulation background without fitting any models to the background. The method flags light curves that show additional CV excesses that are likely caused by other types of variability or that potentially show two power excesses from solar-like oscillations. We found that the light-curve processing from the KADACS pipeline caused the distribution of noise in the power spectra to differ (greater dispersion) from expectations for a χ^2 distribution with 2 degrees of freedom, so we instead analyzed data processed by the KASOC (R. Handberg & M. N. Lund 2014) filter where available (6939 stars), and we used the data from the Kepler pipeline downloaded from MAST with some minimal processing for the rest.

A.3.3. FLI

The FliPer method described in L. Bugnet et al. (2018) is based on the averaged power density contained in the PSD. It allows for measurement of stellar surface parameters (L. Bugnet et al. 2018) or to classify pulsators (L. Bugnet et al. 2019). In the case of solar-like stars, granulation occurs at characteristic frequencies and amplitude correlated with characteristic frequencies and amplitude of the stochastic oscillations it generates (e.g., T. Kallinger et al. 2010; S. Mathur et al. 2010; F. A. Bastien et al. 2013, see Figure 22), the average power density of a solar-like star correlates with its $\nu_{\rm max}$. The FliPer method relies on a random forest (machine learning) algorithm, trained on thousands of Kepler data analyzed with the A2Z+ pipeline (S. Mathur et al. 2011) to automatically estimate $\nu_{\rm max}$ of other Kepler stars from the power contained in the PSD (see L. Bugnet et al. 2018, for more details). It is particularly valuable compared to classic asteroseismology for stars with $\nu_{\rm max}$ at low frequency ($\nu_{\rm max} \lessapprox 10$ μHz), close to and above the Nyquist frequency of the observations, and for stars observed with poor frequency resolution, as there is no need for mode detection to estimate the typical frequency of the oscillations.

Appendix B
Merging Individual Results

Our full sample includes 7555 spectroscopic dwarfs and 15,791 spectroscopic giants. Unlike APOKASC-2, the methods used vary significantly in their precision, and we are not restricted to uniformly high-quality light curves. We therefore had to filter our raw data to reject outlier measurements and to identify background sources. We began by using inferred median results and MADs for our full sample, and then identified and removed robust detections that were clearly from background sources. We followed up by applying a spectroscopic prior to reject individual false-positive measurements, and then rejected measurements strongly inconsistent with the ensemble average. See Appendix B.2. below for the details of the outlier rejection procedure. At the end of this process, we had up to 10 $\nu_{\rm max}$ and up to seven $\Delta\nu$ measurements per target.

With this data in hand, we then adopted a procedure similar to that of APOKASC-2 for combining the raw data from individual pipelines into a single value for each target. We began by dividing the data into data quality categories. The highest-quality cohort, the Gold sample, had a minimum of five independent detections of $\Delta\nu$; the Silver sample had at least two independent $\Delta\nu$ values; and the Detected sample had a minimum of two independent $\nu_{\rm max}$ measurements, but less than two $\Delta\nu$ values. We then placed all stars on a common zero-point by applying small offsets to data from each pipeline, using the Gold RGB sample as a reference data set. We follow by using the agreement between individual pipelines and the ensemble average to give each pipeline a weight; this was done separately for the Gold RGB, Gold RC, and Silver samples. We could then construct weighted averages for our central values; for the "Detected" subsample, we report only $\nu_{\rm max}$. Details of our procedure are described below.

B.1. Identifying Background Sources

We started with data from 13 pipelines. Three of the results corresponded to alternative measurements using the same underlying method as another entry. As these data are strongly correlated, we adopted only one measurement per technique. This left us with 10 independent measurements for $\nu_{\rm max}$, and seven for $\Delta\nu$. This is because the other three methods (Bell, Hon, and FliPer) either did not provide $\Delta\nu$, or did so purely in a statistical manner.

Each light curve is extracted from a number of pixels centered on the target. These Kepler "postage stamps" can be relatively large, and it is possible for asteroseismic signals to be associated with a different target than the associated KIC ID. In some cases the sources are separable spatially, but this need not be true. The most straightforward discriminant is whether the measured $\nu_{\rm max}$ is in the rough domain expected given the spectroscopic data. We therefore used APOGEE DR16 and DR17 spectroscopic surface gravities and effective temperatures to predict a "spectroscopic" $\nu_{\rm max}$. The median uncertainty in the spectroscopic measurements is 0.065 dex (Table 3); to be conservative, we broadened the prior to 3σ in both directions, for a minimum total permitted range of 0.39 dex. As discussed in H. Jönsson et al. (2020), there were corrections applied to the derived spectroscopic values that depended on evolutionary state. To ensure that our results were not biased by the evolutionary states assigned, we further broadened the priors by the difference between the spectroscopic gravities that would have been inferred for RC and RGB states in the domain where both families are observed. Finally, we broadened the prior to account for log$g$ differences between DR16 and DR17 for stars with data in both.

We then computed the $\nu_{\rm max}$ median and MAD for all targets. Stars with measurements inconsistent with the spectroscopic prior at the 5σ level are shown in Figure 23. A total of 129 asteroseismic detections were classified as background sources with this technique. This included 63 targets classified as giants and 66 classified as dwarfs or subgiants. Their properties are discussed in Section 3.5.

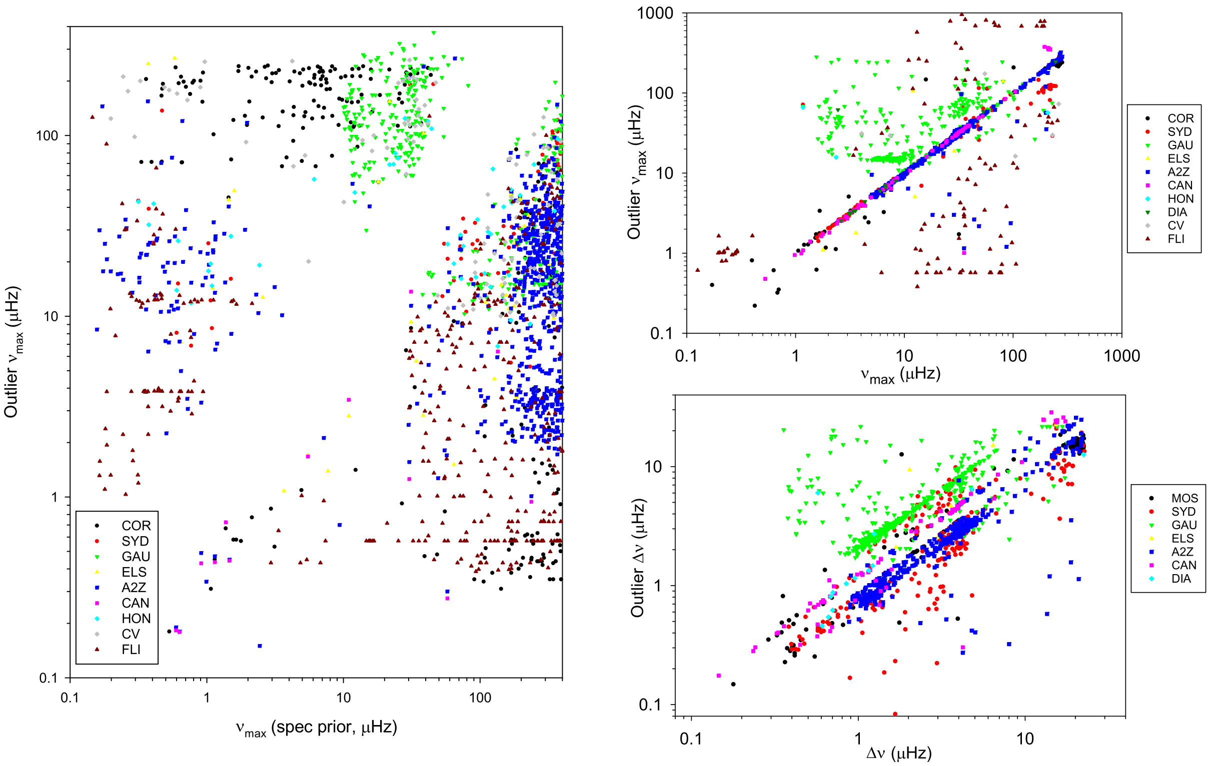

Figure 23. Measurements flagged as outliers in APOKASC-3. The left panel shows data with $\nu_{\rm max}$ inconsistent with the spectroscopic prior. The right panels show measurements inconsistent with other pipelines in $\nu_{\rm max}$ (top right) and $\Delta\nu$ (bottom right). Measurements consistent with the prior are not shown for visual clarity. The population of $\nu_{\rm max}$ measurements close to the unity line were rejected because their corresponding $\Delta\nu$ measurements disagreed. The large majority of rejected measurements are strongly inconsistent with the prior.

B.2. Median Outlier Rejection: Spectroscopic and Ensemble Priors

Having checked for global consistency with spectroscopy, we now turn to the validation of individual measurements. We are using automated techniques to collapse an observed frequency pattern into two global figures of merit. In real data, however, there are confounding factors that can give rise to spurious measurements. For example, a background classical pulsator might inject a single spurious frequency signal into a normal red giant pattern; even faint sources can have a detectable variability amplitude. Other stars have unusual oscillation amplitudes or patterns that can confound detection algorithms. Outlier rejection is an efficient tool for identifying both individual failure modes and targets with light curves that are difficult to interpret. We therefore removed individual $\nu_{\max}$ measurements inconsistent with our spectroscopic prior, as defined above. The results are illustrated in Figure 23. If we excluded a $\nu_{\max}$ detection, we also excluded any corresponding $\Delta\nu$ measurement.

Our final pass involved checking whether the measurements that we included were consistent with the full ensemble of data. Our averaging technique will be biased in the presence of large method-to-method differences, which would manifest as a translation of systematic errors into random ones. To avoid this, in some cases, the trends that we identified caused us to restrict the $\nu_{\max}$ domain for techniques that differed significantly from the mean. The GAU results were not run with the longer 80 day filter, so we did not use them for stars with $\nu_{\max}$ below 10 μHz. The A2Z pipeline had significant systematic differences in $\Delta\nu$ relative to other methods for stars with $\nu_{\max}$ <5 μHz, due to the way it computes $\Delta\nu$ on a broad frequency range instead of computing a local value centered on $\nu_{\max}$. We therefore did not include them in this domain.

With these data removed, there is both a well-behaved core and an excess of outliers. We therefore performed a final outlier rejection test for individual pipeline results relative to the median. We performed this test only for targets with three or more detections, and we removed measurements discrepant from the median at more than 5σ. This test was employed for both $\nu_{\max}$ and $\Delta\nu$, with both measurements excluded if either failed the outlier test. Figure 23 compares individual measurements excluded by this method with the ensemble average. (Some of the data appear close to the median in $\nu_{\max}$ or $\Delta\nu$; such stars were failures in the other value.)

Table 6 summarizes our measurement and detection statistics for all methods. For each pipeline, the total number of raw $\nu_{\max}$ detections per method is in row 1; the number of $\nu_{\max}$ values excluded as spectroscopic outliers is in row 2; the number of $\nu_{\max}$ values excluded as ensemble outliers is in row 3; and the corresponding number of $\Delta\nu$ outliers excluded is in row 4. The total numbers of filtered $\nu_{\max}$ and $\Delta\nu$ measurements per pipeline are in rows 5 and 6.

Table 7 summarizes the net outcome of our filtering process. We includes the raw data, the spectroscopic prior range used,

Table 6
Detection Statistics by Pipeline

Category	COR	ELS	GAU	SYD	A2Z	DIA	CAN	CV	HON	FLI
Detected ($\nu_{\max}$)	12,860	12,204	11,122	13,147	13,676	2069	8294	10,483	12,590	14,113
Reject (log$g$)	988	56	3583	94	3203	0	19	303	58	1289
Reject (ens)	15	6	279	19	14	1	12	6	3	113
Detected ($\Delta\nu$)	11,867	11,222	10,547	12,127	10,995	1899	7164	0	0	0
Reject (ens)	120	19	517	220	540	13	77	N/A	N/A	N/A

Note. Columns correspond to different pipelines. The first row identifies the pipelines. Rows 2, 3, and 4 are the number of $\nu_{\max}$ detections, measurements inconsistent with the spectroscopic prior, and measurements inconsistent with the ensemble median, respectively. Rows 5 and 6 present $\Delta\nu$ detections and measurements rejected as inconsistent with the ensemble median, respectively.

Table 7
Raw Asteroseismic Measurements and Filtering Results

Label	Contents
KIC ID	Number in the Kepler Input Catalog
$\nu_{\max}$ Spec Min, Max	Lower and upper bounds, spectroscopic prior
NDET	Total number of $\nu_{\max}$ detections prior to quality cuts
NNMAX	Number of valid $\nu_{\max}$ measurements after outlier rejection
NDNU	Number of valid $\Delta\nu$ measurements after outlier rejection
NCOR to NFLI	$\nu_{\max}$ data quality flag for pipelines COR, ELS, GAU, SYD, A2Z, DIA, CAN, CV, HON, and FLI, respectively
$\nu_{\max}$ COR to FLI	$\nu_{\max}$ values for pipelines COR, ELS, GAU, SYD, A2Z, DIA, CAN, CV, HON, and FLI, respectively
DCOR to DCAN	$\Delta\nu$ data quality flag for pipelines COR, ELS, GAU, SYD, A2Z, DIA, and CAN, respectively
$\Delta\nu$ COR to CAN	$\Delta\nu$ values for pipelines COR, ELS, GAU, SYD, A2Z, DIA, and CAN, respectively

Note. We include the raw measurements from all 10 input pipelines for $\nu_{\max}$ and all seven for $\Delta\nu$. We also give the permitted range for the spectroscopic filter, the number of measurements with any $\nu_{\max}$ detections, the number of filtered $\nu_{\max}$ detections, and the number of filtered $\Delta\nu$ detections. The codes NCOR to NFLI reflect the category of the data for each star. A 0 entry denotes no data, 1 is a valid filtered measurement, 2 is one that failed the spectroscopic prior, and 6 is one that failed the ensemble prior test. A 9 entry denotes data excluded from usage because it fell outside the range of validity for that pipeline. The DCOR to DCAN codes give data quality for $\Delta\nu$ measurements, using the same notation as that used for $\nu_{\max}$.

(This table is available in its entirety in machine-readable form in the online article.)

Table 8
Relative Zero-point Scales and Sample Sizes by Pipeline

Category	COR	ELS	GAU	SYD	A2Z	DIA	CAN	CV	HON	FLI
Scale ($\nu_{\rm max}$)	0.9961	0.9995	1.0014	1.0003	1.0005	1.0018	1.0031	0.9911	1.0011	0.9729
N ($\nu_{\rm max}$)	5124	5130	4710	5144	5143	975	3643	4565	5125	5136
σ (Gold, RGB)	0.0115	0.0140	0.0282	0.0158	0.0224	0.0245	0.0116	0.0511	0.0568	0.1352
σ (Gold, RC)	0.0110	0.0137	0.0146	0.0167	0.0274	0.0110	0.0111	0.0618	0.0533	0.1429
σ (Silver)	0.0859	0.0525	0.1744	0.0736	0.0816	0.0465	0.0549	0.5360	0.2039	1.3767
Scale ($\Delta\nu$)	1.0045	0.9983	0.9989	0.9985	1.0000	0.9968	1.0000	n/a	n/a	n/a
N ($\Delta\nu$)	5113	5077	4622	5133	4987	973	3611	0	0	0
σ (Gold, RGB)	0.0158	0.0099	0.0239	0.0153	0.0222	0.0329	0.0135	n/a	n/a	n/a
σ (Gold, RC)	0.0148	0.0116	0.0176	0.0144	0.0227	0.0136	0.0185	n/a	n/a	n/a
σ (Silver)	0.0932	0.0567	0.1740	0.1056	0.1221	0.0521	0.0903	n/a	n/a	n/a

star-by-star detection statistics, and quality codes for individual measurements.

B.3. Data Quality: Gold, Silver, Detection, No Detection

There is a strong correlation between the number of consistent measurements from different techniques and the measurement scatter. Two of our seven core methods were not used on the full data set, so we define our Gold sample as stars with five or more $\Delta\nu$ detections. We required at least two measurements to treat a detection as valid. If there were two or more $\Delta\nu$ data, the target was included in the Silver sample; stars with zero or one $\Delta\nu$ values, but at least two $\nu_{\rm max}$ ones, were treated as Detections. Other stars were classified as Nondetections. Our detection statistics are discussed in Section 2.2.2.

B.4. Zero-points and Pipeline Weights

Each asteroseismic pipeline has both a solar zero-point and a measurement uncertainty based on the quality of the power spectrum. However, in the APOKASC-2 paper, we measured the ensemble average for all methods and could infer both the relative measurement zero-points and the scatter of each method around the mean. We found that the formal uncertainties were not correlated with how well an individual pipeline predicted the ensemble average, and the relative stellar zero-points were not the same as the relative solar zero-points. Given these results, we therefore adopted an empirical approach. Table 8 presents the scale factors and weights.

For stars with high-quality measurements, we compare individual pipeline values to the ensemble mean, and define relative scale factors for each method. This ensures that the mix of detection methods does not bias the zero-point of the average. For $\Delta\nu$, the fractional zero-point corrections are at most ±0.004; for $\nu_{\rm max}$, they are at most ±0.008. The solar $\nu_{\rm max}$ reference value in APOKASC-2, 3076 μHz, was inferred by requiring agreement between fundamental masses in open cluster stars and asteroseismic values. In the current paper, we use fundamental radii to anchor the asteroseismic radii, and by extension masses, onto a fundamental system. This new correction factor is inferred relative to the APOKASC-2 solar reference value, and described in Section 3.2. For $\Delta\nu$, we use the APOKASC-2 solar value of 135.1416 μHz for the initial base zero-point.

For pipeline weights, we divided our sample into three groups. Gold sample stars had five or more $\Delta\nu$ and $\nu_{\rm max}$ detections, and we further split the Gold sample into separate RC and RGB cohorts. Silver sample stars had a minimum of two $\Delta\nu$ detections and a maximum of four. Most of these stars are on the upper RGB. Table 8 lists the standard deviation of each method in each group. We note that the scatter here is somewhat inflated by a modest population of large outliers; with 5σ outlier rejection, the formal errors are roughly two-thirds as large, with similar relative performance in different pipelines. However, to be conservative in our error budget, we used the larger uncertainties.

To study systematic uncertainties in measurements, we rank-ordered data in mean $\nu_{\rm max}$ and $\Delta\nu$. Figure 24 shows the ratio of measurements from each technique in 100-star bins to the mean, as functions of $\nu_{\rm max}$ for the RC and RGB stars. The corresponding data for $\Delta\nu$ are shown in Figure 25.

Table 9 presents our individual and averaged measurements. The zero-point adjusted (see Table 8) individual pipeline entries that were accepted as valid (State 1 from Table 7) are given here. We then present several statistical characterizations of the data. We present both straight averages of measurements and ones corrected to the same mean zero-point. The weighted averages used the weights given in Table 8, and the uncertainties are the formal standard error of the mean. We also give median values and the MAD converted to an effective dispersion by multiplying the MAD by 1.4826, appropriate for a normal distribution. For the work that follows, we will use the weighted mean averages in most cases, switching to a median for cases with only two detections, which is equivalent to a simple average. We discuss tests of our error model in Section 3.4.

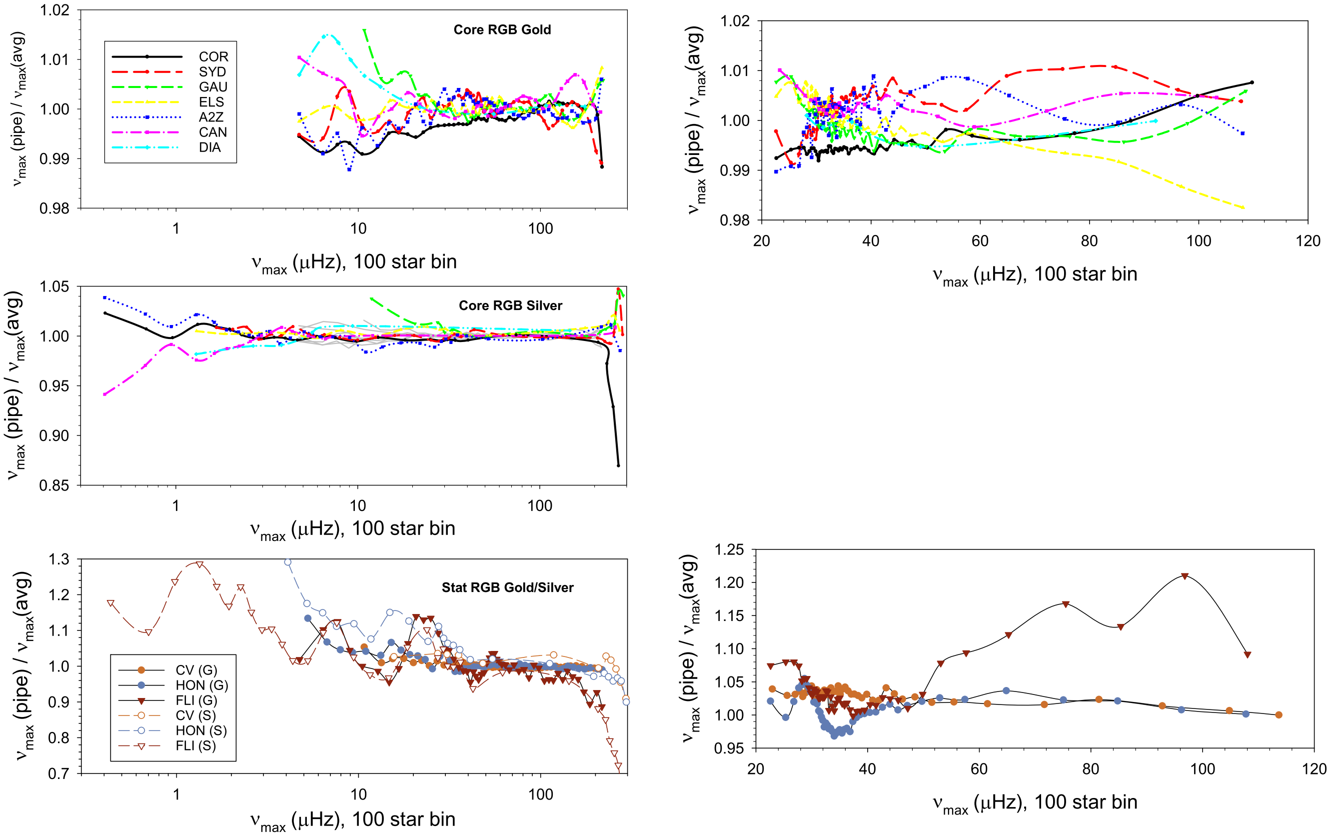

Figure 24. Pipeline systematic offsets in ν_{max} for RGB (left) and RC (right). We distinguish our seven core methods and show results for the Gold sample (top) and Silver sample (middle). Our ν_{max}-only methods are shown in the bottom panels. Different symbols and line styles demote different pipelines (see the legend). For ν_{max} in the RGB Gold sample, fractional differences are at the ±0.004 level, rising to ±0.012 at low and high ν_{max}; a comparable ±0.009 range is seen for the RC. The Silver sample and the ν_{max}-only methods have larger scatter, especially in the low ν_{max} domain.

Table 9
Filtered Asteroseismic Measurements and Different Methods for Combining Them

Label	Contents
KIC	Number in the Kepler Input Catalog
NDet, NFDet	Number of raw and filtered ν_{max} detections
NDNDet	Number of filtered $\Delta\nu$ detections
NmaxCrct, SigNmaxCrct	Zero-point adjusted average ν_{max} and fractional σ
NmaxWtCor, SigNmaxWtCor	Weighted mean ν_{max} and fractional standard error of the mean
NmaxMed, NmaxMAD	Median ν_{max} and median absolute deviation converted to fractional σ
NMAXCOR to NMAXFLI	ν_{max} values for pipelines COR, ELS, GAU, SYD, A2Z, DIA, CAN, CV, HON, and FLI, respectively
DNuCrct, SigDNuCrct	Zero-point adjusted average $\Delta\nu$ and fractional σ
DNuWtCor, SigDNuWtCor	Weighted mean $\Delta\nu$ and fractional standard error of the mean
DNuMed, DNuMAD	Median $\Delta\nu$ and median absolute deviation converted to fractional σ
DNUCOR to DNUCAN	$\Delta\nu$ values for pipelines COR, ELS, GAU, SYD, A2Z, DIA, and CAN, respectively

Note. A straight average (Crct), a weighted average (WtCor), and a median (Med) are given, along with σ (averages) and the median absolute deviation (median). The weighted average is used where available.

(This table is available in its entirety in machine-readable form in the online article.)

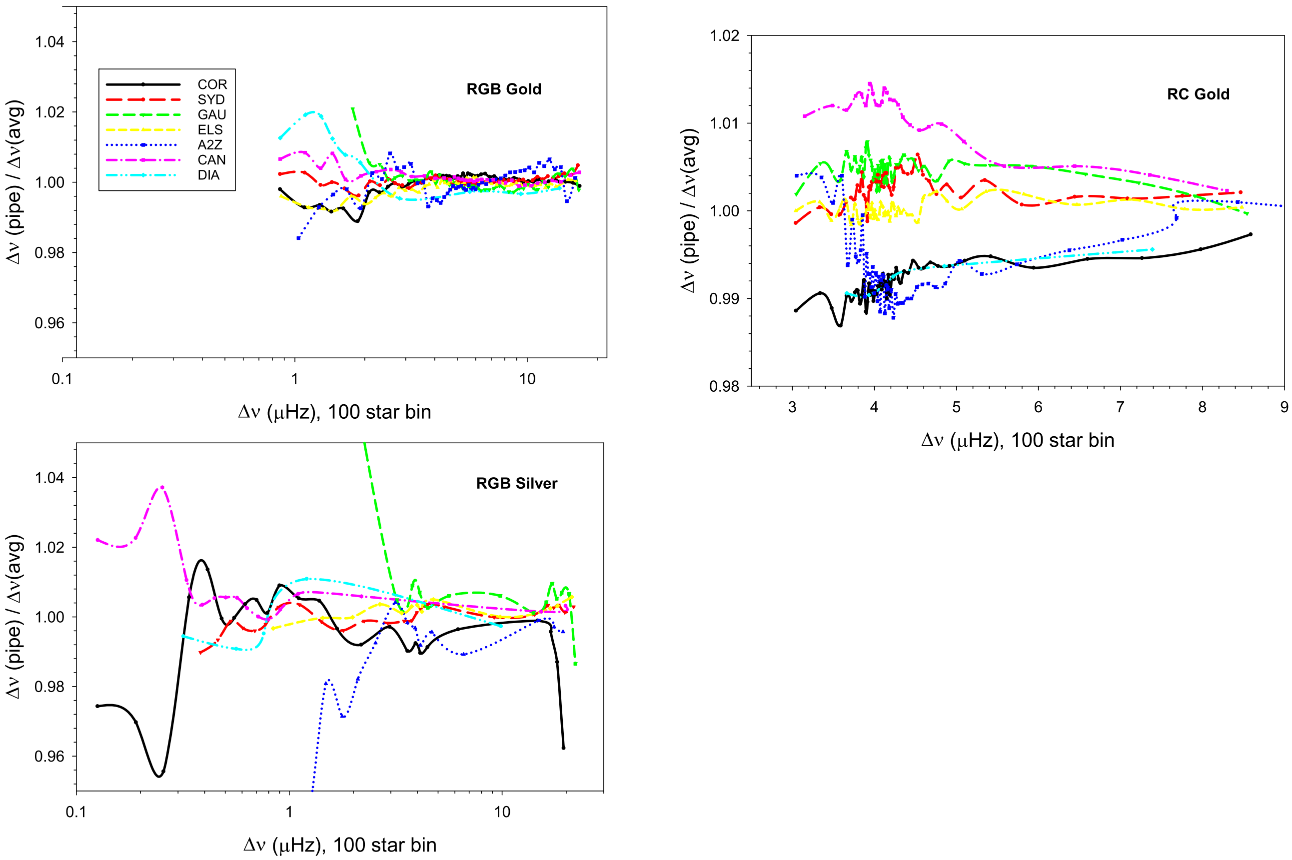

Figure 25. Pipeline systematic offsets in $\Delta\nu$ for RGB (left) and RC (right). We show results for the Gold sample (top) and Silver sample (bottom). Different symbols and line styles demote different pipelines (see the legend). For $\Delta\nu$ in the Gold RGB sample, fractional differences are at the ±0.004 level, rising to ±0.02 at low $\Delta\nu$; a ±0.01 range is seen in the primary RC, with a smaller ±0.005 range in the secondary RC. Note that the Silver RC sample is small, and not shown here.

ORCID iDs

Marc H. Pinsonneault https://orcid.org/0000-0002-7549-7766
Joel C. Zinn https://orcid.org/0000-0002-7550-7151
Jamie Tayar https://orcid.org/0000-0002-4818-7885
Aldo Serenelli https://orcid.org/0000-0001-6359-2769
Rafael A. García https://orcid.org/0000-0002-8854-3776
Savita Mathur https://orcid.org/0000-0002-0129-0316
Benoit Mosser https://orcid.org/0000-0002-7547-1208
Dennis Stello https://orcid.org/0000-0002-4879-3519
Keaton J. Bell https://orcid.org/0000-0002-0656-032X
Lisa Bugnet https://orcid.org/0000-0003-0142-4000
Enrico Corsaro https://orcid.org/0000-0001-8835-2075
Patrick Gaulme https://orcid.org/0000-0001-8330-5464
Saskia Hekker https://orcid.org/0000-0002-1463-726X
Marc Hon https://orcid.org/0000-0003-2400-6960
Daniel Huber https://orcid.org/0000-0001-8832-4488
Thomas Kallinger https://orcid.org/0000-0003-3627-2561
Kaili Cao https://orcid.org/0000-0002-1699-6944
Bastien Liagre https://orcid.org/0009-0008-7869-7430
Ângela R. G. Santos https://orcid.org/0000-0001-7195-6542
Sarbani Basu https://orcid.org/0000-0002-6163-3472
Paul G. Beck https://orcid.org/0000-0003-4745-2242
Timothy C. Beers https://orcid.org/0000-0003-4573-6233
William J. Chaplin https://orcid.org/0000-0002-5714-8618
Katia Cunha https://orcid.org/0000-0001-6476-0576
Peter M. Frinchaboy https://orcid.org/0000-0002-0740-8346
Léo Girardi https://orcid.org/0000-0002-6301-3269
Diego Godoy-Rivera https://orcid.org/0000-0003-4556-1277
Jon A. Holtzman https://orcid.org/0000-0002-9771-9622
Henrik Jönsson https://orcid.org/0000-0002-4912-8609
Szabolcs Mészáros https://orcid.org/0000-0001-8237-5209
Claudia Reyes https://orcid.org/0000-0001-9632-2706
Hans-Walter Rix https://orcid.org/0000-0003-4996-9069
Matthew Shetrone https://orcid.org/0000-0003-0509-2656
Verne V. Smith https://orcid.org/0000-0002-0134-2024
Taylor Spoo https://orcid.org/0000-0003-4019-5167
Keivan G. Stassun https://orcid.org/0000-0002-3481-9052
Ji Wang https://orcid.org/0000-0002-4361-8885

References

Abdurro'uf, Accetta, K., Aerts, C., et al. 2022, ApJS, 259, 35
Abolfathi, B., Aguado, D. S., Aguilar, G., et al. 2018, ApJS, 235, 42
Adelberger, E. G., Garcìa, A., Robertson, R. G. H., et al. 2011, RvMP, 83, 195
Ahn, C. P., Alexandroff, R., Allende Prieto, C., et al. 2014, ApJS, 211, 17
Ahumada, R., Allende Prieto, C., Almeida, A., et al. 2020, ApJS, 249, 3
Alonso, A., Arribas, S., & Martinez-Roger, C. 1994, A&A, 282, 684
Angulo, C., Arnould, M., Rayet, M., et al. 1999, NuPhA, 656, 3
Ash, A. L., Pinsonneault, M. H., Vrard, M., & Zinn, J. 2025, ApJ, 979, 135
Bastien, F. A., Stassun, K. G., Basri, G., & Pepper, J. 2013, Natur, 500, 427
Basu, S. 2016, LRSP, 13, 2
Beaton, R. L., Oelkers, R. J., Hayes, C. R., et al. 2021, AJ, 162, 302
Beck, P. G., Grossmann, D. H., Steinwender, L., et al. 2024, A&A, 682, A7
Bedding, T. R. 2014, in Asteroseismology, ed. P. L. Pallé & C. Esteban (Cambridge: Cambridge Univ. Press), 60
Bedding, T. R., Huber, D., Stello, D., et al. 2010, ApJL, 713, L176
Bedding, T. R., Mosser, B., Huber, D., et al. 2011, Natur, 471, 608

Belkacem, K., Goupil, M. J., Dupret, M. A., et al. 2011, A&A, 530, A142
Bell, K. J., Hekker, S., & Kuszlewicz, J. S. 2019, MNRAS, 482, 616
Blanton, M. R., Bershady, M. A., Abolfathi, B., et al. 2017, AJ, 154, 28
Bossini, D., Miglio, A., Salaris, M., et al. 2015, MNRAS, 453, 2290
Breton, S. N., Santos, A. R. G., Bugnet, L., et al. 2021, A&A, 647, A125
Brown, T. M., Latham, D. W., Everett, M. E., & Esquerdo, G. A. 2011, AJ, 142, 112
Bugnet, L., Garcìa, R. A., Davies, G. R., et al. 2018, A&A, 620, A38
Bugnet, L., Garcìa, R. A., Mathur, S., et al. 2019, A&A, 624, A79
Carlberg, J. K., Majewski, S. R., Patterson, R. J., et al. 2011, ApJ, 732, 39
Casagrande, L., Schönrich, R., Asplund, M., et al. 2011, A&A, 530, A138
Casagrande, L., & VandenBerg, D. A. 2014, MNRAS, 444, 392
Cassisi, S., Potekhin, A. Y., Pietrinferni, A., Catelan, M., & Salaris, M. 2007, ApJ, 661, 1094
Cao, K., & Pinsonneault, M. H. 2025, ApJ, submitted
Ceillier, T., Tayar, J., Mathur, S., et al. 2017, A&A, 605, A111
Chaplin, W. J., Bedding, T. R., Bonanno, A., et al. 2011, ApJL, 732, L5
Christensen-Dalsgaard, J. 2008, Ap&SS, 316, 113
Christensen-Dalsgaard, J., & Thompson, M. J. 1997, MNRAS, 284, 527
Constantino, T., Campbell, S. W., Christensen-Dalsgaard, J., Lattanzio, J. C., & Stello, D. 2015, MNRAS, 452, 123
Corsaro, E., & De Ridder, J. 2014, A&A, 571, A71
Corsaro, E., Mathur, S., Garcìa, R. A., et al. 2017, A&A, 605, A3
Cox, J. P., & Giuli, R. T. 1968, Principles of Stellar Structure (New York: Gordon and Breach)
Crawford, C. L., Bedding, T. R., Li, Y., et al. 2024, MNRAS, 528, 7397
Cui, X.-Q., Zhao, Y.-H., Chu, Y.-Q., et al. 2012, RAA, 12, 1197
De Ridder, J., Barban, C., Baudin, F., et al. 2009, Natur, 459, 398
Deheuvels, S., Ballot, J., Gehan, C., & Mosser, B. 2022, A&A, 659, A106
Demarque, P., Guenther, D. B., Li, L. H., Mazumdar, A., & Straka, C. W. 2008, Ap&SS, 316, 31
Dréau, G., Mosser, B., Lebreton, Y., Gehan, C., & Kallinger, T. 2021, A&A, 650, A115
Dupret, M. A., Belkacem, K., Samadi, R., et al. 2009, A&A, 506, 57
Dziembowski, W. A., Gough, D. O., Houdek, G., & Sienkiewicz, R. 2001, MNRAS, 328, 601
Eisenstein, D. J., Weinberg, D. H., Agol, E., et al. 2011, AJ, 142, 72
Elad, M., Starck, J.-L., Querre, P., & Donoho, D. 2005, Appl. Comput. Harmonic Anal., 19, 340
Elsworth, Y., Hekker, S., Johnson, J. A., et al. 2019, MNRAS, 489, 4641
Elsworth, Y., Themeßl, N., Hekker, S., & Chaplin, W. 2020, RNAAS, 4, 177
Epstein, C. R., Elsworth, Y. P., Johnson, J. A., et al. 2014, ApJL, 785, L28
Evans, J. W., & Michard, R. 1962, ApJ, 135, 812
Ferguson, J. W., Alexander, D. R., Allard, F., et al. 2005, ApJ, 623, 585
Feuillet, D. K., Bovy, J., Holtzman, J., et al. 2018, MNRAS, 477, 2326
Freytag, B., Ludwig, H. G., & Steffen, M. 1996, A&A, 313, 497
Fu, J.-N., Cat, P. D., Zong, W., et al. 2020, RAA, 20, 167
Gaia Collaboration, Vallenari, A., Brown, A. G. A., et al. 2023, A&A, 674, A1
Garcìa, R. A., Gourvès, C., Santos, A. R. G., et al. 2023, A&A, 679, L12
Garcìa, R. A., Hekker, S., Stello, D., et al. 2011, MNRAS, 414, L6
Garcìa, R. A., Mathur, S., Pires, S., et al. 2014, A&A, 568, A10
Garcìa, R. A., Mathur, S., Salabert, D., et al. 2010, Sci, 329, 1032
Garcìa Pérez, A. E., Allende Prieto, C., Holtzman, J. A., et al. 2016, AJ, 151, 144
Gaulme, P., Appourchaux, T., & Boumier, P. 2009, A&A, 506, 7
Gaulme, P., Jackiewicz, J., Spada, F., et al. 2020, A&A, 639, A63
Gehan, C., Mosser, B., Michel, E., Samadi, R., & Kallinger, T. 2018, A&A, 616, A24
Godoy-Rivera, D., Mathur, S., Garca, R., et al. 2024, A&A, submitted
González Hernández, J. I., & Bonifacio, P. 2009, A&A, 497, 497
Grevesse, N., & Noels, A. 1993, in Origin and Evolution of the Elements, ed. N. Prantzos, E. Vangioni-Flam, & M. Casse (Cambridge: Cambridge Univ. Press), 15
Grevesse, N., & Sauval, A. J. 1998, SSRv, 85, 161
Grosjean, M., Dupret, M. A., Belkacem, K., et al. 2014, A&A, 572, A11
Gunn, J. E., Siegmund, W. A., Mannery, E. J., et al. 2006, AJ, 131, 2332
Handberg, R., Brogaard, K., Miglio, A., et al. 2017, MNRAS, 472, 979
Handberg, R., & Lund, M. N. 2014, MNRAS, 445, 2698
Harvey, J. 1985, in ESA Special Publication 235, Future Missions in Solar, Heliospheric & Space Plasma Physics, ed. E. Rolfe & B. Battrick (Noordwijk: ESA), 199
Hekker, S., Kallinger, T., Baudin, F., et al. 2009, A&A, 506, 465
Holtzman, J. A., Hasselquist, S., Shetrone, M., et al. 2018, AJ, 156, 125
Hon, M., Huber, D., Kuszlewicz, J. S., et al. 2021, ApJ, 919, 131
Hon, M., Stello, D., Garcìa, R. A., et al. 2019, MNRAS, 485, 5616
Hon, M., Stello, D., & Yu, J. 2017, MNRAS, 469, 4578
Hon, M., Stello, D., & Zinn, J. C. 2018, ApJ, 859, 64
Huber, D., Bedding, T. R., Stello, D., et al. 2011, ApJ, 743, 143
Huber, D., Pinsonneault, M., Beck, P., et al. 2023, arXiv:2307.03237
Huber, D., Slumstrup, D., Hon, M., et al. 2024, ApJ, 975, 19
Huber, D., Stello, D., Bedding, T. R., et al. 2009, CoAst, 160, 74
Iglesias, C. A., & Rogers, F. J. 1993, ApJ, 412, 752
Iglesias, C. A., & Rogers, F. J. 1996, ApJ, 464, 943
Irwin, A. W., 2012 FreeEOS: Equation of State for Stellar Interiors Calculations, Astrophysics Source Code Library, ascl:1211.002
Jenkins, J. M., Caldwell, D. A., Chandrasekaran, H., et al. 2010, ApJL, 713, L120
Jönsson, H., Holtzman, J. A., Allende Prieto, C., et al. 2020, AJ, 160, 120
Joyce, M., Molnár, L., Cinquegrana, G., et al. 2024, ApJ, 971, 186
Kallinger, T., De Ridder, J., Hekker, S., et al. 2014, A&A, 570, A41
Kallinger, T., Hekker, S., Mosser, B., et al. 2012, A&A, 541, A51
Kallinger, T., Mosser, B., Hekker, S., et al. 2010, A&A, 522, A1
Khan, S., Miglio, A., Willett, E., et al. 2023, A&A, 677, A21
Kjeldsen, H., & Bedding, T. R. 1995, A&A, 293, 87
Kuszlewicz, J. S., Hekker, S., & Bell, K. J. 2020, MNRAS, 497, 4843
Leighton, R. B., Noyes, R. W., & Simon, G. W. 1962, ApJ, 135, 474
Li, G., Deheuvels, S., & Ballot, J. 2024, A&A, 688, A184
Li, Y., Bedding, T. R., Murphy, S. J., et al. 2022, NatAs, 6, 673
Li, Y., Bedding, T. R., Stello, D., et al. 2023, MNRAS, 523, 916
Lindegren, L., Bastian, U., Biermann, M., et al. 2021, A&A, 649, A4
Lu, Y., Buck, T., Minchev, I., & Ness, M. K. 2022, MNRAS, 515, L34
Majewski, S. R., Schiavon, R. P., Frinchaboy, P. M., et al. 2017, AJ, 154, 94
Mathur, S., Garcìa, R. A., Breton, S., et al. 2022, A&A, 657, A31
Mathur, S., Garcìa, R. A., Bugnet, L., et al. 2019, FrASS, 6, 46
Mathur, S., Garcìa, R. A., Huber, D., et al. 2016, ApJ, 827, 50
Mathur, S., Garcìa, R. A., Régulo, C., et al. 2010, A&A, 511, A46
Mathur, S., Hekker, S., Trampedach, R., et al. 2011, ApJ, 741, 119
Mathur, S., Huber, D., Batalha, N. M., et al. 2017, ApJS, 229, 30
Miglio, A., Chiappini, C., Mackereth, J. T., et al. 2021, A&A, 645, A85
Molnár, L., Netzel, H., Howell, M., Kalup, C., & Joyce, M. 2024, arXiv:2409.05391
Montalbán, J., Mackereth, J. T., Miglio, A., et al. 2021, NatAs, 5, 640
Montalbán, J., Miglio, A., Noels, A., et al. 2013, ApJ, 766, 118
Mosser, B., & Appourchaux, T. 2009, A&A, 508, 877
Mosser, B., Barban, C., Montalbán, J., et al. 2011a, A&A, 532, A86
Mosser, B., Benomar, O., Belkacem, K., et al. 2014, A&A, 572, L5
Mosser, B., Belkacem, K., Goupil, M. J., et al. 2011b, A&A, 525, L9
Mosser, B., Dréau, G., Pinçon, C., et al. 2024, A&A, 681, L20
Mosser, B., Dziembowski, W. A., Belkacem, K., et al. 2013, A&A, 559, A137
Mosser, B., Elsworth, Y., Hekker, S., et al. 2012, A&A, 537, A30
Mosser, B., Michel, E., Samadi, R., et al. 2019, A&A, 622, A76
Patton, R. A., Pinsonneault, M. H., Cao, L., et al. 2024, MNRAS, 528, 3232
Paxton, B., Bildsten, L., Dotter, A., et al. 2011, ApJS, 192, 3
Paxton, B., Cantiello, M., Arras, P., et al. 2013, ApJS, 208, 4
Paxton, B., Marchant, P., Schwab, J., et al. 2015, ApJS, 220, 15
Pinsonneault, M. H., An, D., Molenda-Żakowicz, J., et al. 2012, ApJS, 199, 30
Pinsonneault, M. H., Elsworth, Y., Epstein, C., et al. 2014, ApJS, 215, 19
Pinsonneault, M. H., Elsworth, Y. P., Tayar, J., et al. 2018, ApJS, 239, 32
Pires, S., Mathur, S., Garcìa, R. A., et al. 2015, A&A, 574, A18
Reyes, C., Stello, D., Hon, M., & Zinn, J. C. 2022, MNRAS, 511, 5578
Roberts, J. D., Pinsonneault, M. H., Johnson, J. A., et al. 2024, MNRAS, 530, 149
Roxburgh, I. W. 2009, A&A, 506, 435
Roxburgh, I. W., & Vorontsov, S. V. 2006, MNRAS, 369, 1491
Salaris, M., Chieffi, A., & Straniero, O. 1993, ApJ, 414, 580
Santos, A. R. G., Campante, T. L., Chaplin, W. J., et al. 2018, ApJS, 237, 17
Santos, A. R. G., Garcìa, R. A., Mathur, S., et al. 2019, ApJS, 244, 21
Schonhut-Stasik, J., Zinn, J. C., Stassun, K. G., et al. 2024, AJ, 167, 50
Serenelli, A. M., Bergemann, M., Ruchti, G., & Casagrande, L. 2013, MNRAS, 429, 3645
Sharma, S., Stello, D., Bland-Hawthorn, J., Huber, D., & Bedding, T. R. 2016, ApJ, 822, 15
Silva Aguirre, V., Bojsen-Hansen, M., Slumstrup, D., et al. 2018, MNRAS, 475, 5487
Simonian, G. V. A., Pinsonneault, M. H., & Terndrup, D. M. 2019, ApJ, 871, 174
Spoo, T., Tayar, J., Frinchaboy, P. M., et al. 2022, AJ, 163, 229
Starck, J.-L., & Murtagh, F. 2006, Astronomical Image and Data Analysis (Berlin: Springer)
Stello, D., Chaplin, W. J., Basu, S., Elsworth, Y., & Bedding, T. R. 2009, MNRAS, 400, L80
Stello, D., Huber, D., Bedding, T. R., et al. 2013, ApJL, 765, L41

Stello, D., & Sharma, S. 2022, RNAAS, 6, 168
Stello, D., Compton, D. L., Bedding, T. R., et al. 2014, ApJL, 788, L10
Tassoul, M. 1980, ApJS, 43, 469
Tayar, J., Ceillier, T., Garcìa-Hernández, D. A., et al. 2015, ApJ, 807, 82
Tayar, J., Claytor, Z. R., Fox, Q., et al. 2023, RNAAS, 7, 273
Tayar, J., Somers, G., Pinsonneault, M. H., et al. 2017, ApJ, 840, 17
Thoul, A. A., Bahcall, J. N., & Loeb, A. 1994, ApJ, 421, 828
Townsend, R. H. D., & Teitler, S. A. 2013, MNRAS, 435, 3406
VandenBerg, D. A., Bergbusch, P. A., Dotter, A., et al. 2012, ApJ, 755, 15
Vernazza, J. E., Avrett, E. H., & Loeser, R. 1981, ApJS, 45, 635
Viani, L. S., Basu, S., Chaplin, W. J., Davies, G. R., & Elsworth, Y. 2017, ApJ, 843, 11
Vrard, M., Mosser, B., & Samadi, R. 2016, A&A, 588, A87
Vrard, M., Pinsonneault, M. H., Elsworth, Y., et al. 2024, arXiv:2411.03101
Weiss, A., & Schlattl, H. 2008, Ap&SS, 316, 99
White, T. R., Bedding, T. R., Stello, D., et al. 2011, ApJ, 743, 161
Wilson, J. C., Hearty, F. R., Skrutskie, M. F., et al. 2019, PASP, 131, 055001
Xiang, M., Ting, Y.-S., Rix, H.-W., et al. 2019, ApJS, 245, 34
York, D. G., Adelman, J., Anderson, J. E. J., et al. 2000, AJ, 120, 1579
Yu, J., Huber, D., Bedding, T. R., et al. 2018, ApJS, 236, 42
Zasowski, G., Cohen, R. E., Chojnowski, S. D., et al. 2017, AJ, 154, 198
Zasowski, G., Johnson, J. A., Frinchaboy, P. M., et al. 2013, AJ, 146, 81
Zinn, J. C. 2021, AJ, 161, 214
Zinn, J. C., Pinsonneault, M. H., Bildsten, L., & Stello, D. 2023, MNRAS, 525, 5540
Zinn, J. C., Pinsonneault, M. H., Huber, D., & Stello, D. 2019a, ApJ, 878, 136
Zinn, J. C., Pinsonneault, M. H., Huber, D., et al. 2019b, ApJ, 885, 166